AFRL-IF-RS-TR-2004-2
Final Technical Report
January 2004

INJECTABLE CERAMIC MICROCAST SILICON CARBONITRIDE (SiCN) MICROELECTROMECHANICAL SYSTEM (MEMS) FOR EXTREME TEMPERATURE ENVIRONMENTS WITH EXTENSION: MICRO-PACKAGES FOR NANO-DEVICES

University of Colorado at Boulder

APPROVED FOR PUBLIC RELEASE; DISTRIBUTION UNLIMITED.

AIR FORCE RESEARCH LABORATORY
INFORMATION DIRECTORATE
ROME RESEARCH SITE
ROME, NEW YORK

STINFO FINAL REPORT

This report has been reviewed by the Air Force Research Laboratory, Information Directorate, Public Affairs Office (IFOIPA) and is releasable to the National Technical Information Service (NTIS). At NTIS it will be releasable to the general public, including foreign nations.

AFRL-IF-RS-TR-2004-2 has been reviewed and is approved for publication.

APPROVED: /s/

THOMAS E. RENZ
Project Engineer

FOR THE DIRECTOR: /s/

JAMES A. COLLINS, Acting Chief
Information Technology Division
Information Directorate

REPORT DOCUMENTATION PAGE

Form Approved
OMB No. 074-0188

1. AGENCY USE ONLY (Leave blank)	2. REPORT DATE	3. REPORT TYPE AND DATES COVERED
	JANUARY 2004	Final Aug 99 – Aug 03

4. TITLE AND SUBTITLE
INJECTABLE CERAMIC MICROCAST SILICON CARBONITRIDE (SiCN) MICROELECTROMECHANICAL SYSTEM (MEMS) FOR EXTREME TEMPERATURE ENVIRONMENTS WITH EXTENSION: MICRO-PACKAGES FOR NANO-DEVICES

5. FUNDING NUMBERS
C - F30602-99-2-0543
PE - 63739E
PR - E117
TA - 00
WU - 52

6. AUTHOR(S)
Victor M. Bright, Rishi Raj,
Martin L. Dunn, and John W. Daily

7. PERFORMING ORGANIZATION NAME(S) AND ADDRESS(ES)
The Regents of the University of Colorado at Boulder
Office of Contracts and Grants
Campus Box 19
Boulder Colorado 80309-0019

8. PERFORMING ORGANIZATION REPORT NUMBER
N/A

9. SPONSORING / MONITORING AGENCY NAME(S) AND ADDRESS(ES)
Air Force Research Laboratory/IFTC
26 Electronic Parkway
Rome New York 13441-4514

10. SPONSORING / MONITORING AGENCY REPORT NUMBER
AFRL-IF-RS-TR-2004-2

11. SUPPLEMENTARY NOTES

AFRL Project Engineer: Thomas E. Renz/IFTC/(315) 330-3423/ Thomas.Renz@rl.af.mil

12a. DISTRIBUTION / AVAILABILITY STATEMENT
APPROVED FOR PUBLIC RELEASE; DISTRIBUTION UNLIMITED.

12b. DISTRIBUTION CODE

13. ABSTRACT ***(Maximum 200 Words)***
MEMS that can survive ultrahigh-temperatures and corrosive environments are important in a variety of unique applications. This work develops an innovative microfabrication technology for high temperature MEMS: microcasting of injectable polymer-derived SiCN ceramic materials. The techniques allow realization of MEMS with complex, three-dimensional and multilayer geometry useable to 1500 C. Our approach is easy and low cost. Several MEMS were realized and evaluated. The objectives of the extension research project are to investigate a new micro-packaging technology to create a high-vacuum, sealed environment for nano-devices integrated with other electronic or RF circuits. The process fits standard manufacturing infrastructure, and can be scaled to package MEMS or nano devices. Such a micro-package will be critical to the advancement of devices such as nano sized resonators that require high vacuum and clean environment to maintain Q's on the order of 10,000 or higher, or very advanced RF MEMS where packaging can greatly affect performance. Two challenges were identified in the initial proposal: the precision creation of the micro-cap, and the deposition of glass droplets in vacuum. The final deliverable for this project was to demonstrate a MEMS sensor hermetically sealed in vacuum. The sensors performance was measured as a function of time to demonstrate the vacuum and hermetic sealing levels.

14. SUBJECT TERMS
Microelectromechanical Systems, MEMS, Harsh Environments, MEMS Packaging

15. NUMBER OF PAGES
134

16. PRICE CODE

17. SECURITY CLASSIFICATION OF REPORT	18. SECURITY CLASSIFICATION OF THIS PAGE	19. SECURITY CLASSIFICATION OF ABSTRACT	20. LIMITATION OF ABSTRACT
UNCLASSIFIED	UNCLASSIFIED	UNCLASSIFIED	UL

Table of Contents

Table of Figures

Table of Tables

1. Summary of Research Objectives

MEMS that can survive ultrahigh-temperatures (exceeding 1000 ^{o}C) and in chemically corrosive environments are important in a variety of unique applications. For example, potential microdevices that could operate in high temperature and harsh corrosive environments include sensors in gas engines or in space applications. In other cases, the microsystems themselves may contain high temperature environments, such as microscale turbine engines and microscale combustion chambers for MEMS power generation.

Conventional MEMS made by silicon micromachining or LIGA-like techniques are not suitable for long term operation in harsh environments because the structural materials (silicon, most polymers and most metals) cannot survive at temperatures exceeding several hundred degrees Celsius. A material under development for high temperature MEMS is the chemical vapor deposited (CVD) SiC. CVD SiC is patterned using-surface micromachining techniques. The disadvantages of this technology are that both CVD and SiC micromachining are difficult, time-consuming, complex and expensive procedures. Furthermore, it is difficult with CVD SiC to fabricate complex three-dimensional components with high aspect ratios due to the planar nature of the CVD process.

The research objectives of the present work are to develop a novel, innovative microfabrication technology for high temperature MEMS: microcasting of injectable polymer-derived SiCN ceramic materials. The microcasting and associated "polymer-bonding" techniques allow realization of MEMS with complex, three-dimensional and multilayer geometry. Our approach is easy and low cost. The polymer derived SiCN ceramics can be used at temperatures exceeding 1500 ^{o}C. To demonstrate the feasibility of the technology, several MEMS are to be realized and evaluated in a high temperature environment. These include, but are not limited to, cantilever beams, piston actuators, micromotors and microcombustors.

2. Technical Report

2.1 Task Schedule

For reference, the schedule of tasks as set at the start of this contract is included below. The blue shaded time period blocks indicate task completion. The progress of individual tasks is given in Section 2.2.

Task 1: Injectable Ceramics for High-Temperature MEMS	99	00				01				02			
	Q4	Q1	Q2	Q3	Q4	Q1	Q2	Q3	Q4	Q1	Q2	Q3	Q4
a). Develop B-contained injectable ceramics, study material's high temperature stability and electrical conductivity													
b). Study thermal shock behavior of SiCN and Si(B)CN using MEMS scale samples													
c). Develop SiCN: characterize nanostructure, connect to properties													
d). Understand the evolution of nanostructure/composition during heat treatment													
e). Map out range of low-cost starting polymer compositions													
f). Identify atomic oxidation and creep mechanisms													
g). Study thermal stability of SiCN													
h). Identify ranges of property tailoring based on polymer doping													
i). Investigate material parameter effects of liquid polymer on casting quality													
j). Investigate other polymer precursors for injectable ceramics													
k). Fully optimize processing-microstructure-property connections													

Task 2: Microcasting Technology	99	00				01				02			
	Q4	Q1	Q2	Q3	Q4	Q1	Q2	Q3	Q4	Q1	Q2	Q3	Q4
a). Casting procedure for single layer structures													
b). Thermal set and demolding													
c). Cross-linking and pyrolysis procedure													
d). Casting procedure for complex structures													
e). Demolding procedure for complex structures													
f). Improve cross-linking and pyrolysis conditions													
g). Define standard procedures for microcasting ceramic devices													
h). Demonstrate fabrication of microcast parts for combustion chamber													
i). Begin to determine the length-scale range possible by injectable ceramic microcasting													
j). complete identification of the length-scale range of MEMS that can be fabricated with injectable ceramic microcasting													
k). Optimize complete microcasting processing													

Task 3. Multilayer Technology	99	00				01				02			
	Q4	Q1	Q2	Q3	Q4	Q1	Q2	Q3	Q4	Q1	Q2	Q3	Q4
a. Develop deposition of adhesive polymer													
b. Develop techniques for holding ceramic parts during bonding													
c. Develop thermal set, cross-linking, and pyrolysis procedures													
d. Identify metals and develop procedures for metallization													
e. Assess metallization during different fabrication stages													
f. Optimize bonding conditions													
g. Define a standard procedure for polymer-based ceramic bonding													
h. Develop techniques for positional precision for metallization													
i. Optimize metallization process and define a standard procedure													
j. Reduce adhesive polymer footprint size; determine dimensional ranges													
k. Assess bond quality as a function of size scale													

Task 4. Design Knowledge Base	99	00				01				02			
	Q4	Q1	Q2	Q3	Q4	Q1	Q2	Q3	Q4	Q1	Q2	Q3	Q4
a. Characterize material properties using MEMS scale samples													
b. Characterize dimensional stability during microcasting													
c. Extend micromechanical test capability to high temperature													
d. Develop room temperature microindentation test methodology													
e. Determine dimensional tolerances obtainable for microcast SiCN MEMS													
f. Characterize quality of bonded joints; connect to bonding procedures													
g. Develop dimensional change models to be used in MEMS design													
h. Extend instrumented microindentation capability to high temperature													
i. Evaluate cantilever and piston actuator electromechanical performance													
j. Evaluate micromotor electromechanical performance													
k. Determine key performance and life limiting factors of high-T devices													
l. Optimize micromotor fabrication and design													
m. Evaluate material properties following testing													
n. Determine batch fabrication tolerances for microcast MEMS													

Task 5. High-T Structures and Devices	99	00				01				02			
	Q4	Q1	Q2	Q3	Q4	Q1	Q2	Q3	Q4	Q1	Q2	Q3	Q4
a. Design cantilever and piston actuators													
b. Design linear and rotary scratch drive micromotor													
c. Evaluate and refine electromechanical models													
d. Simulate based on measured parameters of SiCN ceramics													
e. Design at least two SiCN combustor configurations													
f. Initial demonstration of cantilever and piston actuator													
g. Fabricate electrostatic cantilever and piston actuator													
h. Fabricate parts for linear and rotary scratch drive micromotors													
i. Assemble parts for linear and rotary scratch drive micromotor													
j. Deposit metal electrodes													
k. Begin to fabricate combustors													
l. Test devices under realistic high-temperature operating conditions													
m. Determine the operating limitations of combustion chamber													
n. Improve actuator performance by refining design and fabrication processing													
o. Explore flame ignition and stabilization strategies in the two combustor designs													

Task 6. Integration Technology	99	00				01				02			
	Q4	Q1	Q2	Q3	Q4	Q1	Q2	Q3	Q4	Q1	Q2	Q3	Q4
a. Develop high-T embedded neighbor strategy													
b. Develop wafer bonding capability													
c. Develop flip-chip integration strategy													
d. Demonstrate flip-chip integration technology													
e. Demonstrate embedded neighbor integration technology													
f. Demonstrate hybrid integration technology													

Research Summary

This research was divided into six components:

Task 1: Injectable Ceramics for High-Temperature MEMS. The focus of this task was to study fundamental properties of polymer-derived silicon carbonitride (SiCN) as it is related to MEMS applications and to synthesize multifunctional materials. We focused on the study of electrical properties.

Task 2: Microcasting/Fabrication Technology. This part of the work centered on development of a comprehensive fabrication technology for SiCN MEMS.

Task 3: Multi-layer Technology. This part of the work is an extension of Task 2, in which techniques for fabrication of multi-layer SiCN MEMS were developed.

Task 4: Design Knowledge Base. The focus of this task was to develop methods for measuring mechanical properties of MEMS-scale SiCN using techniques based on micro indentation. In addition, other processing-related phenomena that affected fabrication capability were investigated.

Task 5: High-Temperature MEMS Devices. This section forms the main accomplishment of this project, which is to realize working MEMS made from SiCN materials. Building on the results from the other Tasks, this part of the project focused on the design, fabrication, characterization, modeling and demonstration of a variety of SiCN MEMS. In addition to commonplace devices such as electrostatic actuators and thermal actuators (which were originally demonstrated in silicon MEMS technology), two new classes of MEMS – ultrahigh-temperature micro heaters and high-temperature polymer MEMS – were realized.

Task 6: Integration Technology. This part of the project focused on the integration of SiCN MEMS with the existing silicon-based MEMS infrastructure. The results of this section are best exemplified in Task 5.

Task 1: Injectable Polymer-Derived Ceramics

This section summarizes the fundamental and applied studies that have been done on polymer-derived SiCN and SiBCN ceramics with the emphasis on use toward MEMS applications. The work centers on synthesis of SiCN using the hot isostatic press, and characterization of electrical properties.

Content:

4. Effect of MEMS Fabrication Processing on SiCN composition
    4.1 Oxidation Rate Constant for MEMS-Processed SiCN at 1400 ^{o}C
    4.2 Composition Change of SiCN from MEMS Process

1. Overview of SiCN and PUMVS Precursor

This section summarizes our work toward the development of injectable polymer-derived ceramics. The materials we have been working on can be classified into two groups: those that contain boron, silicoboron carbonitride (SiBCN), and those that do not, silicon carbonitride (SiCN).

For SiCN, the commercially available Ceraset^{TM} (from Kion Corp.) was used as the starting polymer. The polymer, which is a poly-urea-methyl-vinyl-silazane ("PUMVS"), goes through four states during the conversion of the polymer into ceramics: starting liquid polymer, thermal set solid polymer, cross-linked solid polymer and ceramics.

As-received Ceraset^{TM} is a clear, colorless to pale yellow liquid inorganic thermosetting resin with a viscosity ~ 1000 mPa*s. The material contains repeating units of silicon atoms bonded in alternating sequence to nitrogen atoms, forming a ring structure. Figure T1- 1 shows the chemical structure of Ceraset^{TM}. The material contains vinyl group (CH_2=CH-), bonded to Si outside of the ring structure, which is important for thermosetting. The ratio of CH_2=CHSi, CH_3-Si and H-Si is 1:5:3 [Y. Li and R. Riedel, "Formation of Silicon Based Ceramics From Polyureamethylvinylsilazane", 2000].

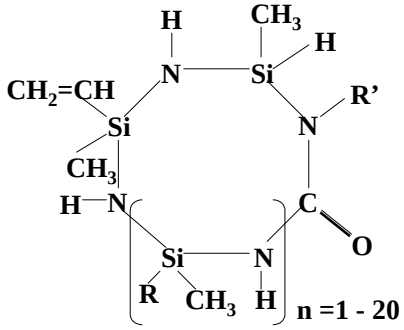

R, R': H, CH_3, or $CH=CH_2$

Figure T1- 1. Chemical structure of Ceraset^{TM} (inorganic polymer).

[D.V. Miller, "Fabrication of SiC Fiber Reinforced SiC Matrix Composites Using Ceraset^{TM} SN Preceramic Polymer," IEA International Workshop on SiC Ceramic Composites for Fusion Structural Applications, 28-29 Oct. 1996, Ispra, Italy]

The as-received Ceraset^{TM} can be thermally set into solid products by heating it at temperature higher than 240 ^{o}C in an inert atmosphere (N_2 or Ar). The viscosity of the polymer increases continuously during the thermal setting forming gel-like, rubber-like and rigid solid accompanied by 1–3 wt% loss. The weight loss is caused by evaporation of the light isomer or rings without vinyl group. The solidification time is a function of temperature. When the temperature is higher than 300 ^{o}C, the solidification is achieved as soon as the temperature is reached. The obtained solids are colorless and transparent, and easy to machine. The thermosetting mechanism is a reaction between vinylsilyl group ($SiCH=CH_2$) and reactive hydrosilyl group (Si-H) [Y. Li and R. Riedel, 1999]:

$$SiCH=CH_2 + H\text{-}Si = SiCH_2\text{-}CH_2Si \qquad \text{(Eq. T1-1)}$$

The thermosetting temperature can be dramatically reduced to ~ 50-150 ^{o}C if a catalyst with free radical initiator such as Dicumyl peroxide is added. Further increasing temperature will result in the continuous reactions within the polymer, which we call cross-linking. After heat-treating in the range 400 – 500 ^{o}C, the hydrogen and nitrogen content significantly decrease (ammonia (NH_3) and H_2 gaseous by-products) while the other elements remain nearly unchanged. The reaction mechanisms during 400 – 500 ^{o}C temperature range are [Y. Li and R. Riedel, 1999]:

$$\text{Si-H} + \text{H-N} = \text{Si-N} + H_2 \qquad \text{(Eq. T1-2)}$$

$$3\ \text{Si-NH-Si} = 2\ NSi_3 + NH_3 \qquad \text{(Eq. T1-3)}$$

The ring structure in Ceraset remains after thermosetting, but is broken in cross-linking reactions, as evidenced by the evaporation of NH_3 since only the ring contains nitrogen. The gaseous by-products produce micropores in the thermoset material. This can be avoided by applying isostatic pressure during cross-linking. The cross-linked polymer is infusible, does not dissolve in any organic solvent and does not melt.

The cross-linked sample starts thermal decomposition when temperature is higher than 500 ^{o}C and becomes ceramic at temperature ~ 1000 ^{o}C. This process is called pyrolysis. With the rise of the pyrolysis temperature the sample's color changes from transparent to yellow between 500 – 600 ^{o}C, to red-brown between 650 –750 ^{o}C, to dark-brown above 800 ^{o}C and finally becomes black at ~ 1000 ^{o}C. The main gases that come out during pyrolysis are H_2, maximum weight loss occurs at 600 and 700 ^{o}C, and methyl (CH_4), maximum weight loss occurs at 600 ^{o}C. The material obtained at 1000 ^{o}C is amorphous. The resultant polymer powder-derived ceramic has composition of $SiN_{0.81}C_{0.85}$. (Note that the formula for a polymer-derived ceramic is obtained by calculation from the weight percentage, which is obtained from chemical analysis. Thus the formula is empirical.)

The material thus obtained has excellent physical properties (see Table T1- 1). It is stable up to ~ 1500 ^{o}C in N_2 or Ar, and up to 1600 ^{o}C in Air. The material also shows excellent creep and oxidation resistance [L. An, et al., J. American Ceramic Society, 81, 3321-3324,1998; R. Raj, et al., J. American Ceramic Society, submitted (2000)]. Figure T1- 2 shows microstructures of samples derived from a powder compact (a) and from isostatically pressed cross-linked bulk sample (b). The cast sample shows great improvement in microstructure with no detectable defect, while the powder sample contains ~ 10 vol% porosity. Figure T1- 2 also shows the improvement in strength and hardness of the cast sample compared to powder sample.

	$SiN_{0.81}C_{0.85}$	**Si**	**SiC**	**Si_3N_4**
Density (g/cm^3) (casting sample)	2.35	2.33	3.17	3.19
E Modulus (GPa) (powder sample)	158	163	405	314
Poisson's Ratio (powder sample)	0.18	0.22	0.14	0.24
CTE (x 10^{-6}/K) (powder sample)	~ 3	2.5	3.8	2.5
Hardness (GPa) (casting sample)	25	11.2	30	28
Strength (MPa) (casting sample)	630	175	418	700
Toughness (MPa.m$^{1/2}$) (casting sample)	3.5	0.9	4-6	5-8
Thermal Shock Resistance*	8000	429	271	892

*strength/(E-modulus CTE); # measured from sample derived from $Si_{1.7}CN_{1.6}$ [R. Riedel, et al., "Synthesis of Dense Silicon-Base Ceramics at Low Temperatures, Nature, 714-16, 1992]

Table T1- 1. Physical Properties of SiCN (obtained from polymer powder), Si, SiC and Si_3N_4

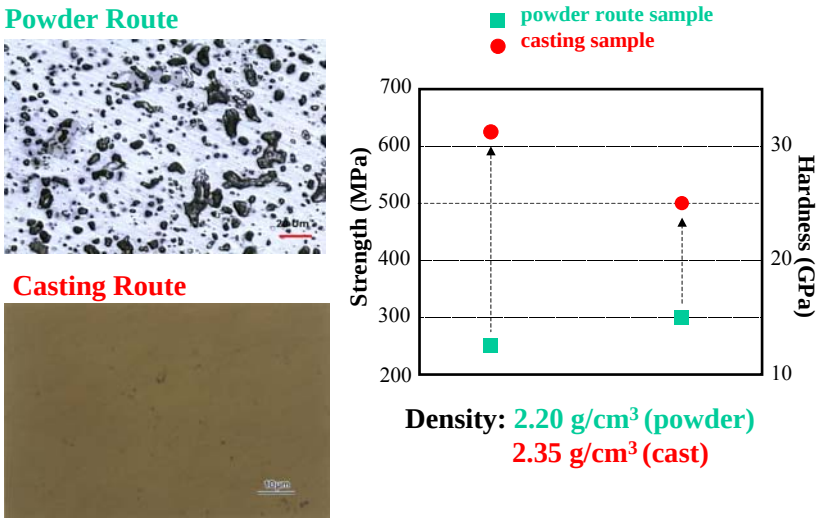

Figure T1- 2. Microstructure of $SiC_{0.81}N_{0.85}$ samples

Obtained by (a) powder route and (b) casting route approach. Comparison of strength and hardness between powder sample and cast sample.

Prior to this project, laboratory made polymer precursors for SiBCN have been used [R. Riedel, et al., Nature, 382 796-98 (1996)]. The precursor is obtained from hydroboration of dimethysulphide boron ($(CH_3)_2S.BH_3$) and dichloromethylvinylsilane ($Cl_2CH_3SiC_2H_3$). The amount of Si and B in the final ceramics is varied by the ratio of $(CH_3)_2S.BH_3$ to $Cl_2CH_3SiC_2H_3$. Powder derived $Si_{1.2}B_1C_{3.9}N_{2.2}$, $Si_2B_1C_{6.3}N_{2.7}$ and $Si_3B_1C_{9.3}N_{2.9}$ have been produced. The SiBCN materials are stable up to 1800 ^oC in N_2 or Ar, much higher than SiCN, implying that MEMS made from SiBCN materials are suitable for even higher temperature applications than SiCN. The SiBCN materials are still under development, many properties of them are still unknown at this time.

We have measured electrical conductivity of these $SiN_{0.81}C_{0.85}$ and $Si_2B_1C_{6.3}N_{2.7}$ materials. The electrical resistivity of the $SiN_{0.81}C_{0.85}$ is ~ 10^7 ohm-cm at room temperature, being an effective insulator, while that of the $Si_2B_1C_{6.3}N_{2.7}$ is ~ 10 ohm-cm.
Figure T1- 3(a) shows the electrical resistivity of SiBCN as a function of temperature.
Figure T1- 3(b) is the plot of conductivity against temperature. The results reveal that the Si_2BCN is a well-behaved amorphous semiconductor, following Mott's 3-D transport model [A. Madan and M.P. Shaw, "The Physics and Applications of Amorphous Semiconductors," Academic Press, P75, 1988].

In this project we have focused on the electrical conductivity of Ceraset^{TM}-derived SiCN and SiBCN, which had not previously been investigated. Results are reported later in this section. The room-temperature d.c. resistivity of these materials are reported, and the Mott parameters for the 3D variable range hopping model were found via data from fabricated MEMS devices.

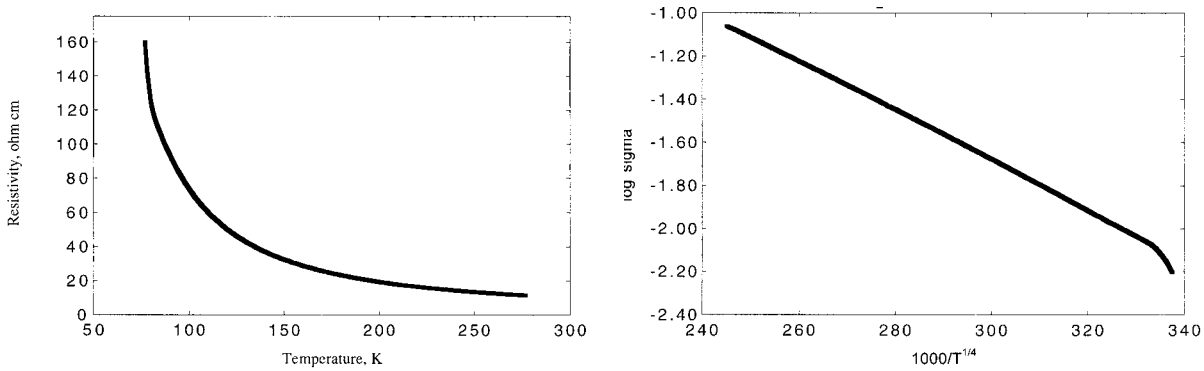

Figure T1- 3. (a) Electrical resistivity of $Si_2B_1C_{6.3}N_{2.7}$ as a function of temperature, and (b) electrical conductivity.

The thermal shock resistance, R, of the polymer-derived SiCN has been estimated [D.P.H. Hasselman, "Thermal Stress Resistance Parameters for Brittle Refractory Ceramics: A Compendium," Amer. Ceram. Soc. Bulletin, 1033-37 (1970)]:

$$R = \sigma/(E\alpha) \qquad \text{(Eq. T1-4)}$$

where σ is the fracture strength, E is theYoung's Modulus and α is the coefficient of thermal expansion. The thermal shock resistance of SiCN and SiC is listed in Table T1-1. SiCN shows much higher thermal shock resistance than SiC.

2. Synthesis and Processing of SiCN and SiBCN

2.1 Hydroboration of PUMVS for Synthesizing SiBCN

Addition of boron to SiCN has been found by others [A.M. Hermann et al, *J. American Ceramic Society*, vol.84, no. 10, pp. 2260-2262, 2001] to increase the electrical conductivity by several orders of magnitude. In addition, SiBCN has also been found to be stable to an even higher temperature than pristine SiCN, the glass transition temperature of SiBCN being ~ 1800 ^oC.

There are currently no commercial precursors available for SiBCN. In this project we have synthesized SiBCN by hydroboration of the Ceraset^{TM} precursor. Boron can be introduced to the precursor by reacting Ceraset^{TM} with B-containing light molecular-weight monomers such as decaborane ($B_{10}H_{14}$) and borane (BH_3). In this project we have used $B_{10}H_{14}$ powder.

Since $B_{10}H_{14}$ is well known to react with a wide variety of Lewis bases (L) to form $L_2\,B_{10}H_{12}$ adducts, the $B_{10}H_{12}$-fragments are easily coordinated to basic nitrogen on the polymer back-bone (Figure T1- 4). The BH_3 can be added to Ceraset through the hydroboration of Ceraset, that is the reaction of BH_3 with vinyl group on Ceraset (Figure T1- 5). In both cases the B content is easily controlled by varying the amounts of monomers. Later in this section we report the measurement of room-temperature d.c. electrical resistivity for SiBCN with different concentrations of B.

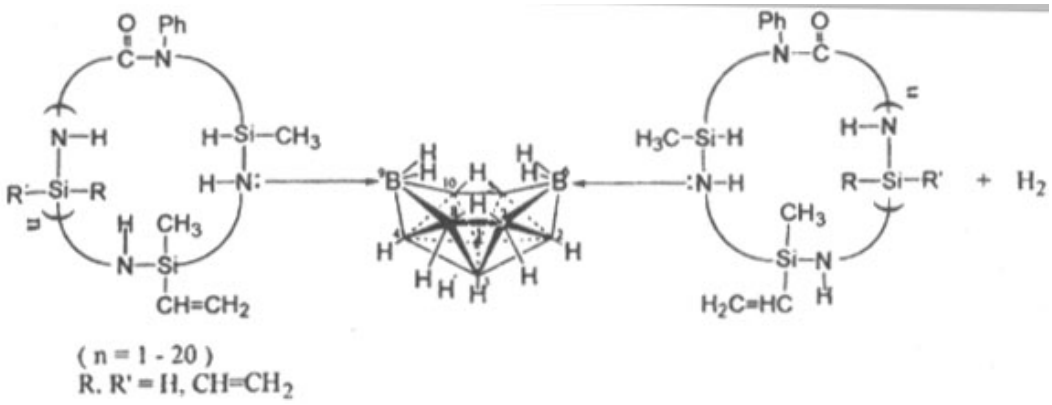

Figure T1- 4. Reaction between $B_{10}H_{14}$ and Ceraset

$$R\text{-}CH{=}CH_2 + BH_3 \;==\; R\text{-}CH_2\text{-}CH_2\text{-}BH_2$$

Figure T1- 5. Reaction between BH_3 and Ceraset.

2.2 Development of the HIP Process for Pyrolysis and Annealing

In December 2000, the hot isostatic press Model AIP 6-30H (from American Isostatic Presses, Inc, Columbus, OH) was installed for pyrolysis. Prior to this, pyrolysis had been done in a tube furnace with flowing nitrogen condition and crosslinking was done separately in a warm isostatic press with silicone oil. The hot isostatic press is a computer-controlled, fully automated high temperature and –pressure furnace commonly used in ceramics processing. With the hot press, we are able to perform crosslinking, pyrolysis, and annealing in one continuous cycle whereas before each step required separate furnaces.

Initial process parameters that were found to be successful in producing SiCN samples that appear comparable to those made using the original process:

Crosslinking: 400 ^{o}C, 4000 Psi (~ 28 MPa) in Argon environment, 1 hour.
Pyrolysis: 1000 ^{o}C, 6000 Psi (~ 41 MPa) in Argon environment, 3 hours.

The resulting samples were crack-free and had a measured hardness of HV = 11-12 GPa. More details can be found in our DARPA technical report from January 2001.

We then systematically refined the processing parameters for the hot isostatic press (HIP). The motivation for the modification of HIP cycles stems from consideration of prior standard pyrolysis processes (without use of the HIP) where a continuous flow of nitrogen is kept. In the present modified HIP processes, a crosslinking step as well as a pseudo-continuous flow of nitrogen were incorporated.

Typical temperature–pressure profiles for pyrolysis-only and pyrolysis-with-annealing HIP cycles are shown in Figure T1- 6 and Figure T1- 7. These are the actual data as recorded in the HIP's data log, as first reported in our DARPA technical report from September 2001.

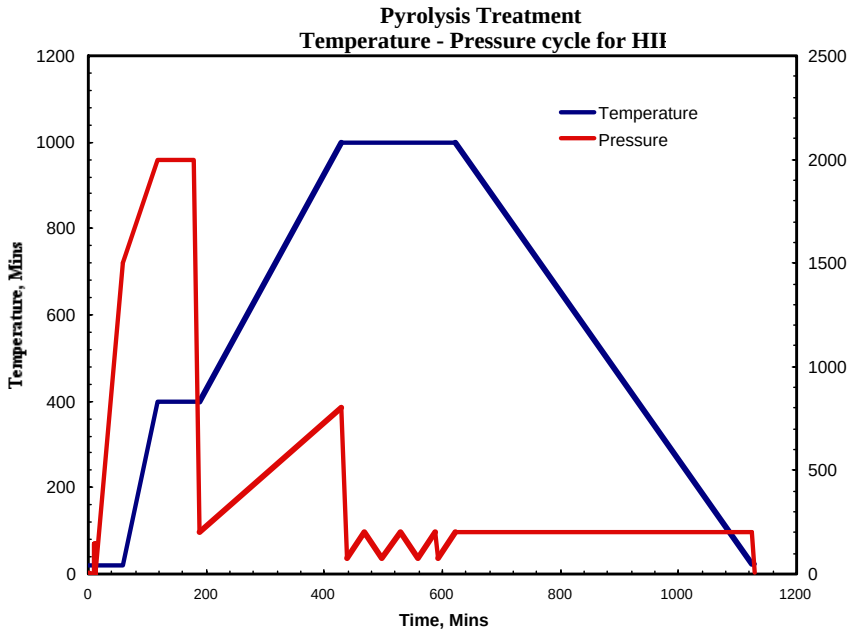

Figure T1- 6. Temperature and pressure profile for pyrolysis cycle in the HIP.

The left vertical axis represents temperature in Celsius. The right vertical axis represents pressure in PSI.

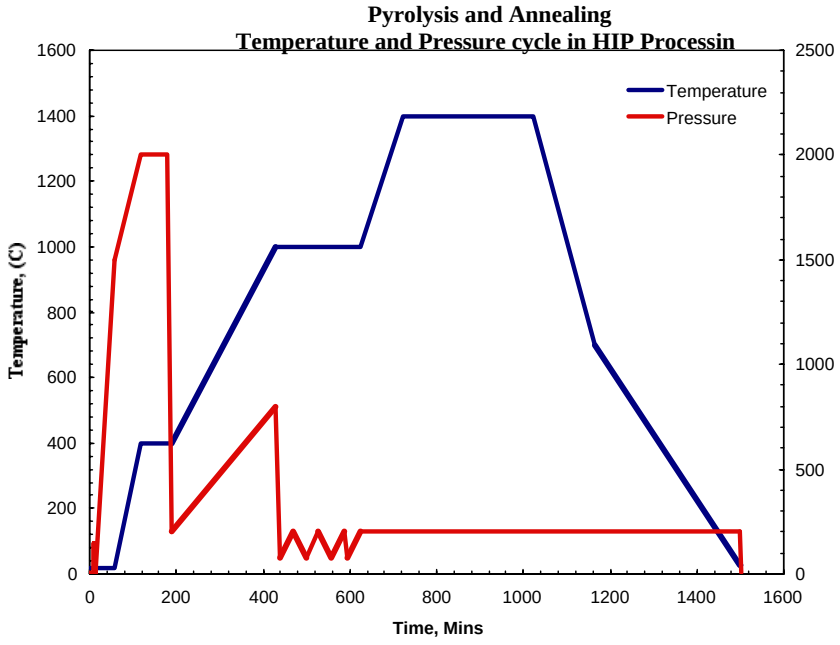

Figure T1- 7. Temperature and pressure profile for combined pyrolysis-and-annealing cycle in the HIP.

The left vertical axis represents temperature in Celsius. The right vertical axis represents pressure in PSI.

With the current HIP processes, near-flat samples with reduced annealing by-products were obtained. This marks a substantial improvement over previous HIP processes in the quality of samples fabricated for MEMS and material-testing purposes.

3. Electrical Properties of SiCN and SiBCN for MEMS applications

SiBCN samples with 0.1%, 1% and 5% boron were sent to Jet Propulsion Laboratory for high temperature property measurement. The preliminary results on electrical conductivity of 5% boron sample as a function of temperature are shown in Figure T1- 8. It can be seen that even at 1000 ^{o}C, the materials still showed semiconductor behavior without breakdown. That means the materials can be used as semiconductor up to 1000 ^{o}C.

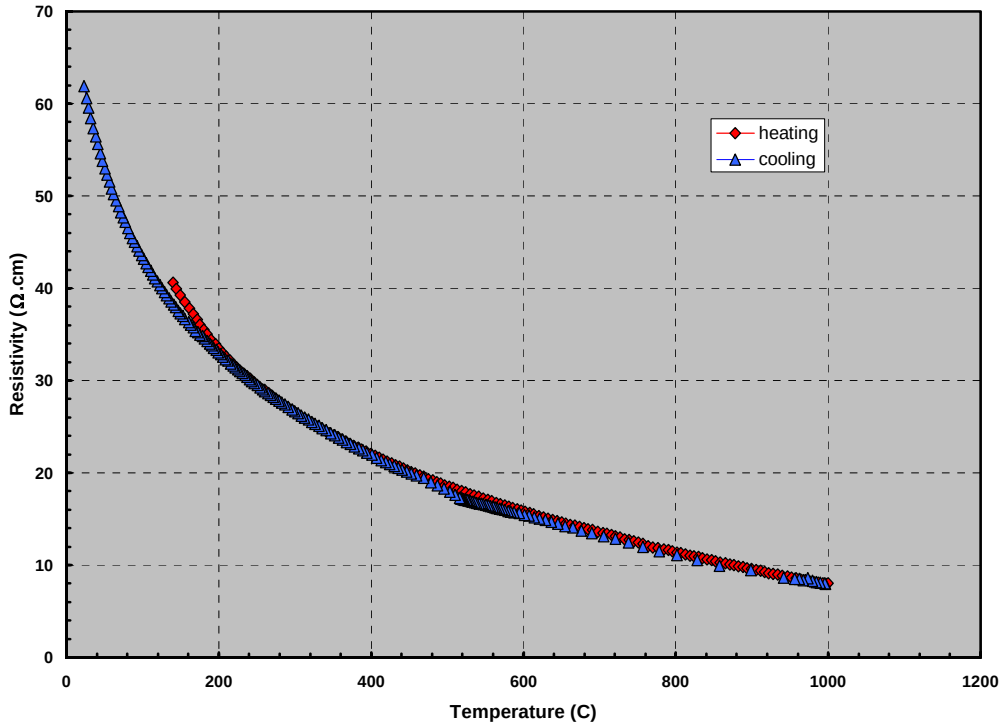

Figure T1- 8. Electrical conductivity of SiBCN derived from the precursor consisting of Ceraset™ + 5 wt% boron.

However, these samples were processed without photopolymerization and with pyrolysis being done in the tube-furnace under flowing nitrogen, rather than in the HIP. Thus, these samples are "pure" material samples that were synthesized independently of any MEMS-related processing. Due to the highly process-dependent nature of polymer-derived ceramics, for the purposes of this project we investigated the electrical properties of PUMVS-derived SiCN and SiBCN that we synthesized via the MEMS-fabrication process described in Task 2 for polymer-micromachining, and using the HIP for pyrolysis and

annealing as described earlier in this section. Investigation of electrical properties of PUMVS-derived, MEMS-fabricated SiCN is unique to this project, and was first reported beginning in our DARPA technical report from January 2001 and continued throughout the remainder of the project.

A typical process for sample fabrication consists of the following: Polymer rectangles are fabricated using microcasting or photopolymerization methods (see our previous DARPA reports for this project). After loading the samples into the hot isostatic press (HIP), the chamber is purged with ultra-high-purity nitrogen several times, then filled to a pressure of 200 PSI. The temperature is then raised to 1000 ^{o}C at a rate of 4 ^{o}C/minute, causing the pressure to increase to about 450 PSI. Pyrolysis consists of maintaining this temperature and pressure for 4 hours, while the nitrogen is periodically purged and then refilled to 200 PSI in 40-minute increments. During pyrolysis the polymer structures thermally decompose into amorphous SiCN. At this point the HIP cycle could be terminated, resulting in as-pyrolyzed SiCN. However, in this case the temperature is then further increased to 1400 ^{o}C at a rate of 6.7 ^{o}C/minute, and held at 1400 ^{o}C and 200 PSI for 5 hours. This high-temperature annealing step is the key to imparting electrical conductivity to the already pyrolyzed SiCN. The mechanism behind this phenomenon is not yet known, but is believed to involve crystallization of SiC as reported in the work for powder-processed SiCN. Following annealing the temperature is lowered first to 700 ^{o}C at a rate of 5 ^{o}C/minute, and then to room temperature at a rate of 2 ^{o}C/minute.

The elements of the above synthesis process that we consider to be the baseline parameters (from which modifications are made in the next section) are:

1. Ceraset^{TM} precursor with 5 wt% DMPA (2,2, dimethoxy-2-phenyl acetophenone) photoinitiator.
2. Pyrolysis at 1000 ^{o}C for 4 hours in N_2 in the hot isostatic press (HIP).
3. Annealing at 1400 ^{o}C for 5 hours in N_2 in the HIP.

Linear four-probe technique is used to obtain a voltage-current curve for the sample, and the resistivity is calculated from the slope of the curve.

Despite the fact that addition of boron has been found in cited works to increase the electrical conductivity [A.M. Hermann et al, *J. American Ceramic Society*, vol.84, no. 10, pp. 2260-2262, 2001] as well the materials' high-temperature stability, in our work we have found boron addition to have the opposite effect on conductivity – i.e., addition of boron leads to *lower* conductivity compared to annealed SiCN, given identical synthesis conditions. Rather than being seen as a disadvantage of boron-addition, however, we instead view this as one way to tailor the material resistivity (see next section).

One disadvantage of SiBCN is the fact that we synthesize the material by adding decaborane powder to the Ceraset^{TM} precursor. This causes the precursor solution to increase in viscosity, making microfabrication difficult. A study was conducted (see next section) to decrease the viscosity by addition of a solvent.

3.1 Effect of Precursor Composition on Si(B)CN Electrical Properties

Table T1- 2 summarizes one set of material samples (rectangular specimens) fabricated by Contact-Photopolymerization and HIP processing. The objective was to investigate the effects of sample composition on electrical resistivity. Note: VL-20^{TM} is a poly-methyl-vinyl-silazane precursor made by Kion Corp as a replacement for Ceraset^{TM}, but which does not contain the urea functional group.

While material resistivity can be altered by varying the annealing conditions (i.e. the HIP process), tailoring the resistivity by altering only its composition is advantageous for fabricating monolithic devices which require individual components to be placed in the HIP together yet exhibit different resistivities, e.g. thermal actuators. As shown in Table T1- 2, all material samples in this first study underwent the same polymer-shaping and HIP processes. Thus, the samples differed only in precursor composition.

Precursor	**Wt% Photo-initiator (DMPA)**	**Si:B Ratio**	**HIP Process**	**Resistivity (Ohm-cm)**
Ceraset™	1%	No Boron	N_2 atmosphere; Pyrolysis @ 1000 °C for 4 hours; Annealing @ 1400 °C for 5 hours;	0.68
Ceraset™	5%	No Boron		0.71
Ceraset™	5%	8:1		4.4
Ceraset™	5%	6:1		7.58
Ceraset™	5%	4:1 diluted in cyclohexane		4.52
Ceraset™	5%	2:1 diluted in cyclohexane		100.9
VL-20™	5%	No boron		0.36

Table T1- 2. Description of SiCN and SiBCN material composition and measured resistivity. Samples underwent identical polymer-shaping and HIP processes, and differed only in composition.

With Boron addition the resistivity was found to increase by an order of magnitude, for all Si:B ratios investigated. However, no conclusion can be drawn at this stage as to the relationship between the resistivity and the Si:B ratio.

This study has shown that we can alter the Si(B)CN material resistivity through changing its composition alone while keeping the annealing times and temperatures constant. This enables the creation of more complex MEMS devices, because now multi-layered devices can be made in which each layer has a different resistivity, e.g. bimorph cantilever actuators. More detail can be found in our DARPA technical report from January 2002.

3.2 Effect of lowering annealing temperature, addition of boron-solvent, and hydrogen atmosphere

Boron addition to Ceraset™ increased the viscosity drastically and removal of entrapped gas could be one of the serious problems for the observed higher resistivity of the B-containing samples. It was thought that the Boron does not go into material structure and may just exist in form of a second phase. However, X-ray diffraction studies failed to show any second-phase peak corresponding to a B phase, and thus B existing in the form of a second phase is ruled out.

A study has been performed to decrease the viscosity of B-containing Ceraset™ by introducing B by a different method. In addition, the annealing temperature in this study was decreased from 1400 to 1350 °C and the time was increased from 5 hours to 10 hours. Decaborane powder (Si:B 4:1) was first

dissolved using Toluene and then added to the Ceraset™ and 5%DMPA mixture. The samples were photo cured and then pyrolyzed and annealed at 1350 °C for 10 hours. Since Decaborane addition to VL-20™ precursor did not drastically affect the viscosity toluene was not used. Further, the result was compared with SiCN (processed using Ceraset – 5%DMPA and pyrolyzed at 1000 °C) heat-treated in hydrogen atmosphere at 1375 – 1400 °C for 2 hours. Table T1- 3 summarizes the samples prepared and results for this study.

Precursor	**Wt% Photo-initiator (DMPA)**	**Si:B Ratio**	**HIP Process**	**Resistivity (Ohm-cm)**
Ceraset™	5%	No Boron	N2 atmosphere; Pyrolysis @ 1000 °C for 4 hours, then annealing @ 1350 °C for 10 hours	98
Ceraset™	5%	4:1, Decaborane first dissolved in Toulene then added to Ceraset™ mixture		434
VL-20™	5%	4:1, no solvent		3338
Ceraset™	5%	No Boron	First pyrolyzed @ 1000 °C in N_2; then annealed @1375-1400 °C for 2 hours in H_2	750

Table T1- 3. Effect on resistivity of lowering annealing temperature with increased time, addition of a solvent for boron, and annealing in a hydrogen atmosphere.

Conclusions from these two studies into SiCN and SiBCN resistivity:

1. *Si(B)CN resistivity can be altered by changing only its composition.*
2. Addition of Boron to SiCN increases the room-temperature resistivity. Hypothesis: addition of decaborane ($B_{10}H_{14}$) into the precursor introduces more dissolved gases, thus during pyrolysis and annealing more gases escape the materials leading to micro cracks or higher porosity, which in turn leads to higher resistivity. Therefore, altering the resistivity by changing the sample composition might lead to a corresponding decrease in mechanical properties.
3. Photoinitiator concentration does not affect resistivity.
4. SiCN (no boron) annealed in H_2 for 2 hours instead of in N_2 for 5 hours, displays an increase in resistivity up to 3 orders of magnitude. (This could be due to either the H_2 or the shorter time or both.)
5. VL-20™ vs. Ceraset™ precursors: VL-20-derived SiCN exhibits the **lowest resistivity** compared to Ceraset-derived SiCN and SiBCN (when all samples are annealed at 1400 °C for 5 hours in N_2). However, VL-20-derived Si**B**CN exhibits the **highest resistivity** compared to Ceraset-derived SiCN and SiBCN (when all samples are annealed at 1350 °C for 10 hours in N_2). This suggests that boron addition adversely affects VL-20 more than Ceraset-derived materials.

3.3 Hall-Effect Measurement of SiCN and SiBCN

Samples of SiCN and SiBCN processed through the MEMS-fabrication route (using photopolymerization and pyrolysis/annealing in the hot isostatic press) were sent to the National Renewal Energy Lab (Golden, Colorado) for Hall Effect measurements.

It has been determined that SiCN is an n-type semiconductor with Hall mobility of 1 cm^2/V-s, while SiBCN is a p-type semiconductor with mobility 2 cm^2/V-s. This result is significant because it points to the future possibility of fabricating high-temperature transistors and other semiconductor devices from SiCN. This result was first reported in our DARPA technical report from June 2002.

Figure T1- 9 shows x-ray spectra for MEMS-processed, annealed samples that are electrically-conductive at room temperature. The lack of sharp peaks indicates that the samples retain a predominantly amorphous structure after annealing.

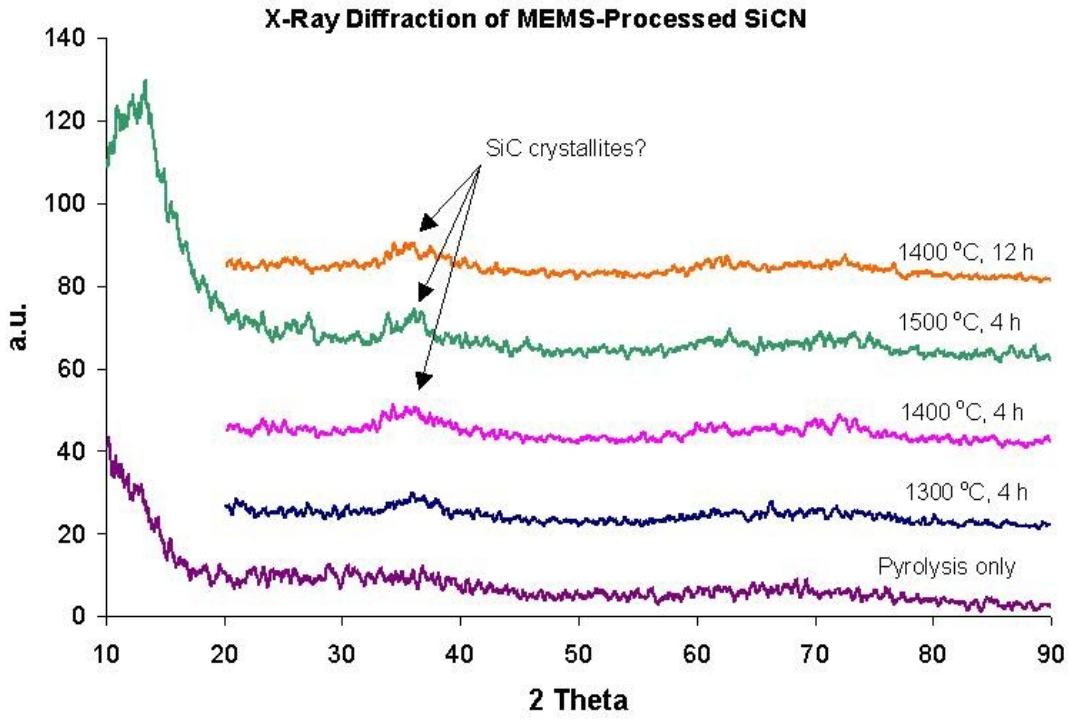

Figure T1- 9. X-ray diffractograms for SiCN processed via the MEMS-route.

4. Effect of MEMS Fabrication Processing on SiCN composition

Polymer-derived ceramics (PDCs) are a relatively new class of materials, developed within the last twenty years and as such data on the properties of these materials is not extensive. This compounds the problem of designing SiCN MEMS. Whereas extensive data bases of material properties exist for designers of silicon-based MEMS, no such precedent exists for PDC MEMS. Furthermore, because of the strong interrelation between processing and properties of PDCs, a valid concern that arises when one considers SiCN MEMS for real-world applications is whether the material properties of micromachined SiCN differ from the published values for SiCN processed independently of the MEMS work.

Therefore, in this project we have considered SiCN material samples processed via the MEMS-route as compared to "pure" SiCN samples synthesized without relation to micromachining. In reality many variations of the latter exist in the literature, since various researchers have each explored unique approaches to synthesizing SiCN from polymer precursors. These non-MEMS related works will collectively be labeled as "the conventional route" since they all share the common characteristic that fabrication of MEMS was not considered a primary objective.

The distinguishing features of the "MEMS-route" compared to the "conventional route" for synthesizing SiCN are: (1) Use of Ceraset^{TM} as the precursor, (2) addition of the DMPA photoinitiator (or dicumyl peroxide) to the precursor, (3) acetone spin rinsing of the precursor, and (4) pyrolysis and annealing in the hot isostatic press (HIP) in nitrogen environment.

4.1 Oxidation Rate Constant for MEMS-Processed SiCN at 1400 ^{o}C

We have been studying the oxidation characteristics of SiCN processed through the MEMS-route - i.e. curing by photopolymerization, followed by heat treatment in a hot isostatic press ("HIP"). Several rectangular samples of dimensions on the order of millimeters were fabricated and pyrolyzed in the HIP, then heat treated in air at 1400 ^{o}C for 4 hours, polished, and then heat treated in air at 1400 ^{o}C for various lengths of time ranging from 1 hour to 150 hours. The oxide thickness was determined by scanning electron microscopy (SEM). Results are shown in Figure T1- 10. The slope of the best-fit line gives the oxidation rate constant. The rate constant for MEMS-processed SiCN at 1400 ^{o}C in air is 5.4 x 10^{-16} m^2/sec.

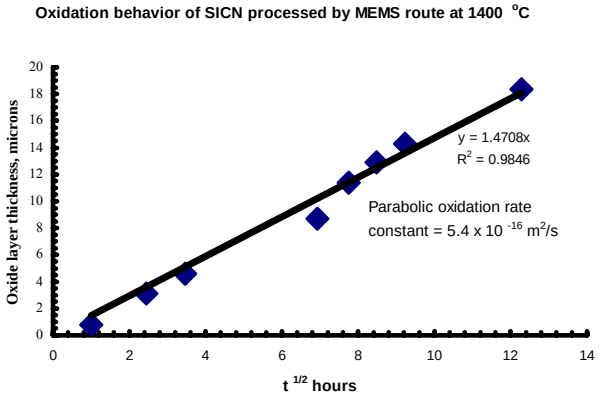

Figure T1- 10. Oxidation data for MEMS-processed bar samples heat-treated at 1400 ^{o}C.

4.2 Composition Change of SiCN from MEMS Process

Figure T1- 11 shows a qualitative IR spectra for MEMS-processed SiCN, for samples that were annealed at different temperatures for 5 hours in nitrogen. This figure shows that the relative size of the C-H peak

and the Si-C peak changes as annealing temperature is increased. Thus, qualitatively we know that the composition of the material changes as annealing temperature is increased.

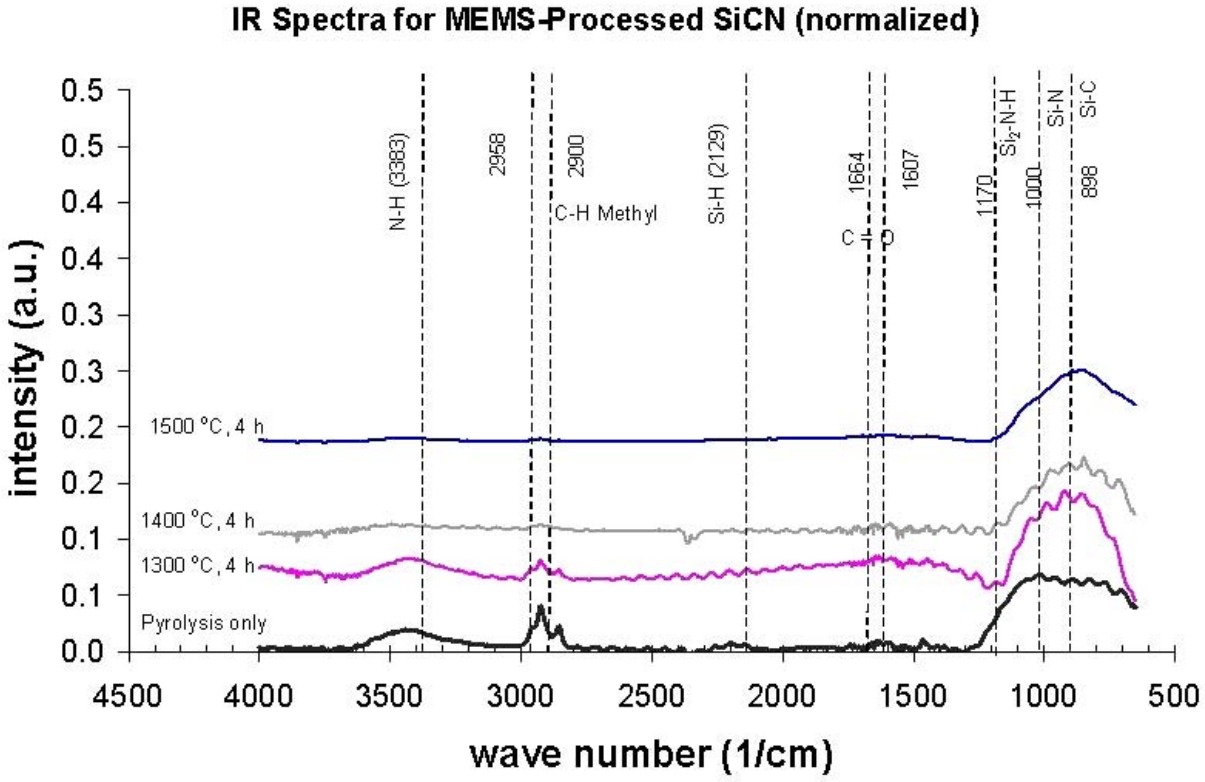

Figure T1- 11. IR spectra of MEMS-processed SiCN.

One surprising aspect Figure T1- 11 is the presence of the C-H bonding to begin with, especially following annealing. The presence of this Methyl group within the SiCN structure indicates incomplete pyrolysis, which is highly unusual given the high temperature pyrolysis of 1000 ^{o}C and above. One possible explanation for the presence of the Methyl group could be the fact that the samples used in this work were pyrolyzed and annealed in the HIP where the nitrogen gas is static, whereas most of the previous work in the literature on non-MEMS processed SiCN utilized pyrolysis conditions under flowing gas, usually Argon.

The IR spectra of as-pyrolyzed samples that were processed by the MEMS-route and the conventional route were then compared, as shown in Figure T1- 12. The "MEMS-processed" samples were those derived from precursor containing the DMPA photoinitiator and spin-rinsed in acetone, while "non-MEMS processed" samples were those obtained from the same precursor that was devoid of catalysts. Furthermore, the samples are distinguished by the pyrolysis conditions, "HIP" being self-explanatory, while "non-HIP" referring to pyrolysis being done in a tube furnace under flowing nitrogen conditions. In all cases the pyrolysis temperature was 1000 ^{o}C.

These results suggest that the HIP is not responsible for the presence of the Methyl group in the final ceramic since the "MEMS-processed, non-HIP" sample (i.e. derived from photopolymerized precursor but pyrolyzed in flowing gas) also displays the C-H peak. Only the sample "Non-MEMS, non-HIP" contains no Methyl group as expected of pure SiCN. Thus, this result suggests that the addition of the photoinitiator and/or rinsing in acetone at the polymer stage gives rise to the presence of the Methyl group in the final SiCN. Thus this is one piece of evidence that SiCN processed via the MEMS-route exhibits different structure and thus properties than pure SiCN processed by the conventional route. However, when comparing the IR of the as-pyrolyzed MEMS-processed samples to the annealed MEMS-processed samples, it is seen that the as-pyrolyzed samples contain a noticeable peak corresponding to C=O bond, whereas neither the annealed samples nor the conventionally processed samples do not. This suggests that another consequence of the photoinitiator and/or acetone is to increase oxygen content within the SiCN, and that through annealing the C=O bonds are broken as carbon is re-directed towards formation of SiC or free carbon. Alternatively, the oxygen could be re-directed toward the formation of the whiskers and crystal clusters as seen sometime under SEM.

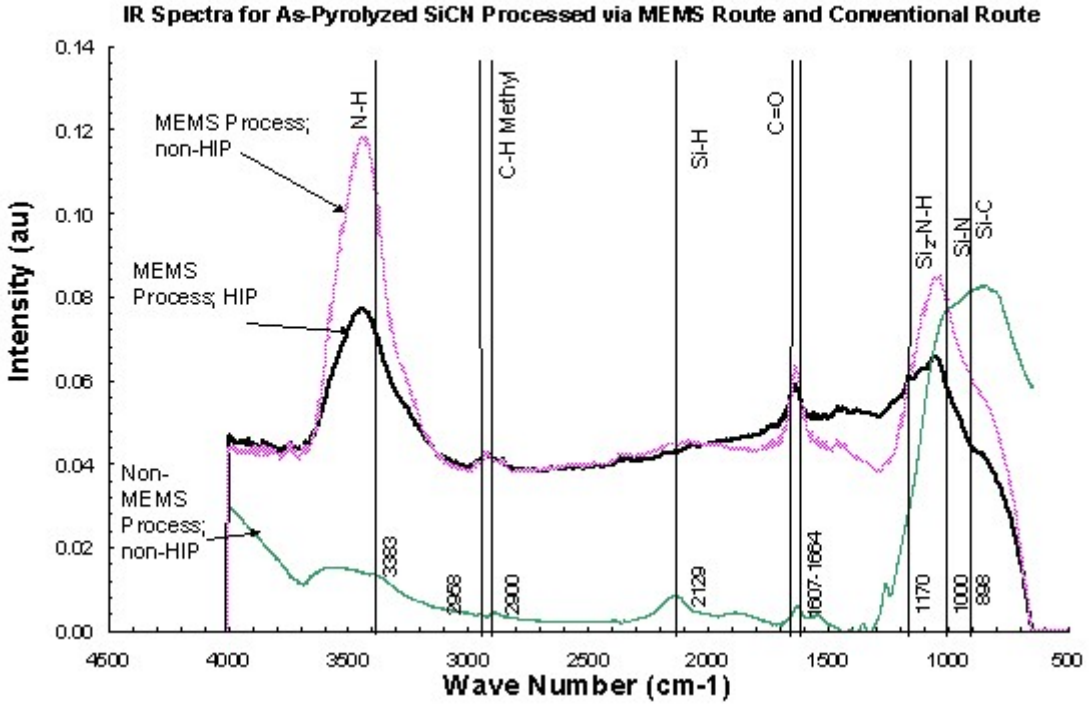

Figure T1- 12. IR spectra for SiCN samples processed via the conventional route and the MEMS-route.

Task 2. Microcasting/Fabrication Technology

This section summarizes the technology and development strategy for fabricating MEMS out of polymer-derived SiCN and its polymer precursor.

Content:

1. Overall Fabrication Technology
2. Development of the Polymer-Micromachining Process
    2.1 Development of the Microcasting Process
    2.2 Development of the Direct-Photopolymerization Process

3. Polymer-to-Ceramic Process

4. Additional Fabrication Techniques
    4.1 XeF_2
    4.2 Macro-scale casting
    4.3 PECVD

1. Overall Fabrication Technology

The overall fabrication process is shown in Figure T2- 1. Although SiCN may be obtained from more than one type of precursor, the precursor used throughout this work is poly-urea-methyl-vinyl-silazane (or PUMVS), available commercially as Ceraset^{TM} from Kion Corp.

It is important to note the distinction between the SiCN material that is synthesized via the procedure developed in this project, and the SiCN that is synthesized outside of this work. While the latter forms the basis for this project's work, the material itself may vary in properties compared to values published independently of this project because of the highly process-dependent properties of the polymer-derived ceramics. For the most part, the material that is characterized in Task 1 is synthesized using a non-MEMS related process unless otherwise stated. This process consists of the following: casting of the liquid precursor in a Teflon mold followed by crosslinking in a warm press under isostatic pressure via silicone oil (60 MPa), followed by pyrolysis in a tube-shaped furnace under flowing nitrogen environment, at 1000 ^{o}C.

Unlike the SiCN materials synthesized independently of the MEMS process, the MEMS-fabrication route begins with a modification of the liquid organic precursor. Catalysts are added to the liquid precursor to enable solidification or polymerization either by low-temperature heating or by exposure to ultraviolet radiation (Step A). Solidification by heating to 140 ^{o}C is referred to as thermosetting, and is made possible by addition of 2 wt% dicumyl peroxide. On the other hand, solidification by exposure to UV (known as photopolymerization) is made possible by addition of 5 wt% 2,2 Dimethoxy-2-phenyl acetophenone ("DMPA", also known commercially as Irgacure 651 from Alrich Chemical, Milwaukee, WI). Photopolymerization of PUMVS is a scientifically new phenomenon, unique to the research at University of Colorado at Boulder, and was driven by the need for SiCN MEMS.

The next step in the fabrication process is polymer-micromachining (Step B), whereby the liquid precursor is shaped into solid MEMS-scale polymer structures. Two separate techniques were developed for accomplishing this: microcasting and direct-photopolymerization.

Once solid polymer shapes are obtained, they may either be used as polymer devices, or they may be subjected to a polymer-to-ceramic process known as pyrolysis (Step C). Pyrolysis consists of firing the material at 1000 ^{o}C to thermally decompose the polymer into SiCN ceramic. During the course of this project, pyrolysis has been done mainly in a hot isostatic press, but also in the tube-furnace.

Upon completion of pyrolysis, the MEMS components are now SiCN ceramic. The SiCN materials are amorphous semiconductors, and the as-pyrolyzed material is electrically insulating at room-temperature. The components may be used in this state; however, for MEMS applications it is usually desirable that the material be electrically conductive at room-temperature so as to enable actuation. Therefore, we typically follow the pyrolysis step with a higher heat-treatment (Step D) at 1350 ^{o}C – 1500 ^{o}C. Upon cooling to room-temperature, the SiCN material displays a room-temperature d.c. resistivity ranging anywhere from 0.1 to 10 Ohm-cm, depending on the annealing temperature, time and environment. This tailoring of the semiconductive properties is one example of how one might exploit the multifunctional properties of polymer-derived ceramics.

One may also functionalize the SiCN material by making composites. For example, we have made SiCN-SiC and SiCN-Fe_3O_4 composites by adding SiC and Fe_3O_4 nano particles to the precursor prior to pyrolysis. The final ceramic composite material exhibits high strength and magnetic properties, respectively, compared to the pristine SiCN.

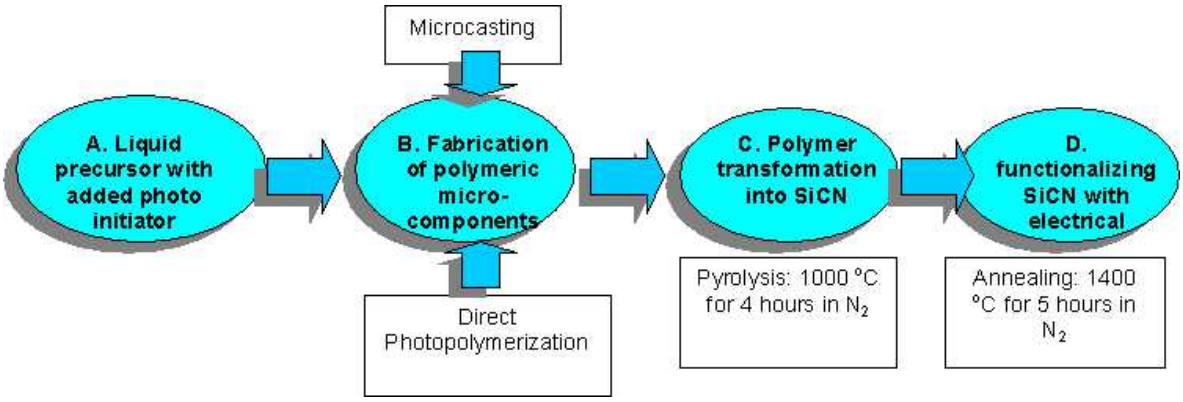

Figure T2- 1. Overall fabrication process for SiCN MEMS

2. Development of the Polymer-Micromachining Process

At the heart of the SiCN MEMS fabrication technology is polymer-micromachining. Since the pyrolysis process does not involve any shape change (except for uniform shrinkage and possible warping unless constrained), micromachining is essentially a polymer process centered around the polysilazane precursor.

Here the SiCN liquid organic precursor, Ceraset^{TM}, is solidified into the microcomponents of desired shape. These solid polymeric components may be either pyrolyzed to produce the ceramic (SiCN) parts, or they may be retained in the polymeric state and used as high-temperature polymer/glass MEMS devices. Two separate micromachining routes were developed in this work: microcasting, and direct photopolymerization.

2.1 Development of the Microcasting Process

Many intermediate approaches to microcasting were considered during the course of this project. These were influenced primarily by two factors: (1) mold-material compatibility with SiCN synthesis/processing, and (2) availability of fabrication facilities at the University of Colorado at Boulder during the time of this research.

The following approaches were considered but ultimately modified or deemed unsuitable:

a. SU8 lost mold (see DARPA technical report Jan 2000)
b. Soft-forged metal foil molds (see DARPA technical report September 2000)
c. Embossed SU8 mold (see DARPA technical report June 2000)
d. Other photoresist molds (see DARPA technical report Jan 2000)
e. NaCl sacrificial mold (see DARPA technical report June 2000)
f. Electroplated metal molds (see DARPA technical report June 2000)
g. Pre-fabricated PMMA and polycarbonate molds (see DARPA technical report June 2000)
h. Wax molds
i. Silicon elastomer molds
j. Bulk-etched silicon molds

The initial effort centered on use of the commercial SU8^{TM} (from Micro Chem Corp.) thick-film photoresist as the mold material. The advantages were excellent definition and high aspect ratios that could be obtained from UV photolithography. The liquid precursor was cast into the SU8^{TM} molds, solidified by thermosetting and polished to remove the top overlying polymer layer that forms from casting. However, a significant disadvantage was the difficulty in removing the mold. Demolding was initially accomplished via the "lost-mold" method whereby the mold was allowed to decompose from the high pyrolysis temperatures that would also convert the cast precursor into ceramic. However, SiCN undergoes about 30% linear shrinkage during pyrolysis, a fact that significantly complicated the fabrication strategy. The presence of the SU8^{TM} mold and the underlying silicon wafer often constrained the shrinkage to the point where the pyrolyzed SiCN components cracked. Another difficult aspect of the fabrication is the high chemical reactivity of the polysilazane precursor. Stripping the mold in the manufacturer-provided solvent resulted in corrosion of the polysilazane. Fabrication yield from this method was thus very low. Attempts at introducing sacrificial material were not successful because the polymer precursor also adheres to most polymers and metals. Details of this process were reported in the DARPA technical report from January 2000.

Thus, we came to the conclusion that demolding of the polymeric components was absolutely necessary so that during pyrolysis the structures could be allowed to shrink freely. This requirement drove the search for appropriate mold materials and processes.

The most successful of these attempts was the soft-forged metal foil method. In this process, positive structures ("masters") were first fabricated from the SU8^{TM} photoresist on silicon, which were then pressed into aluminum foil to create the negative patterns from the foil, which could then be used as molds. After casting and thermosetting of the precursor, the polymeric components are demolded by simply peeling away the metal foil. Although fabrication yield was high, the resultant structures suffered from poor definition and limited aspect ratios. Details of this process were reported in the DARPA technical report from September 2000.

The difficulties with the other processes listed lay in demolding without damage to the polymer structures. Due to the high chemical reactivity of the polysilazane precursor, use of many common solvents and even water led to corrosion of the cast polymer. Figure T2- 2 shows scanning electron micrographs of SiCN MEMS components fabricated using the lost-mold and soft-forged foil mold methods.

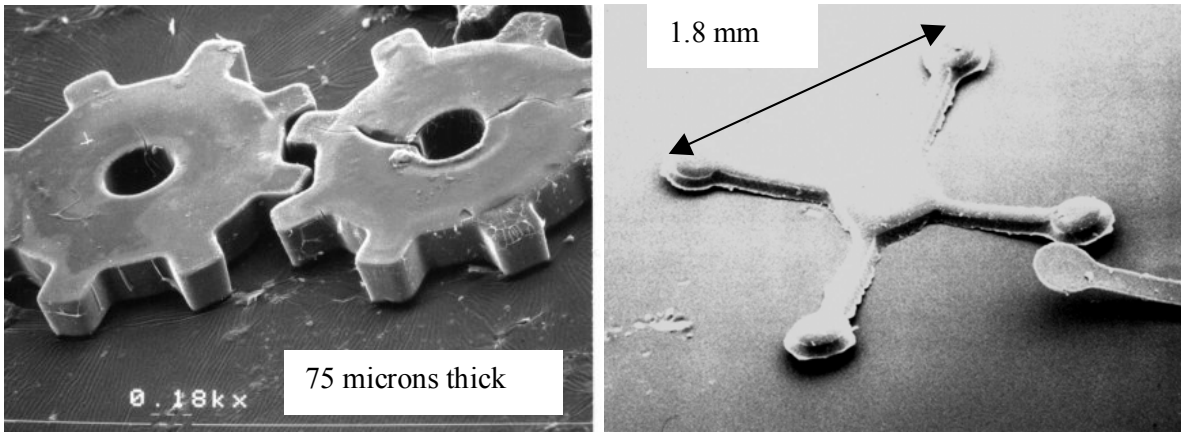

(a) (b)

Figure T2- 2. (a) SiCN micro gears fabricated by casting in SU8 molds using lost mold technique. The main weakness of this method is cracking. (b) SiCN electrostatic actuator structure fabricated by casting in soft-forged aluminum foil mold. The weakness in this method is poor structure definition.

The key to the microcasting process lay in the acquisition of a liquid Teflon solution that was made available under a limited license, approximately halfway through the project.

Figure T2- 3 shows the newly developed fabrication process, first reported in the DARPA technical report from June 2001. First, micro-molds are fabricated out of SU8 photoresist (from Micro Chem Corp) on silicon wafers. A thin, uniform layer of liquid Teflon (from Dupont) is applied to the molds by spin coating and a series of low-temperature (<250 ^{o}C) heat treatments. The liquid Ceraset^{TM}, containing DMPA photo initiator, is then cast onto the wafer. Because the Teflon layer covers the entire surface of the wafer, including the surface of the SU8, the precursor draws away from the SU8 surface due to surface-tension effects and accumulates only in the mold cavities. This eliminates the wafer-polishing step that is common to many micro-molding fabrication techniques such as LIGA (and which also plagued our earlier micro-casting methods because of technical difficulties in the absence of an automated polishing machine). The Ceraset^{TM} is solidified by UV exposure, and demolding is then accomplished by heating the wafer to about 250 ^{o}C. The heat causes the SU8 layer to separate from the silicon wafer, and the cast structures are left on but unattached to the silicon wafer since the Teflon coating weakens the adhesion to both the mold and wafer. The pre-ceramic structures are then crosslinked, pyrolyzed and annealed individually as usual. This low-stress physical demolding made possible by the liquid Teflon is thus the key to fabricating geometrically precise, fully-dense yet crack-free SiCN MEMS structures with fine features.

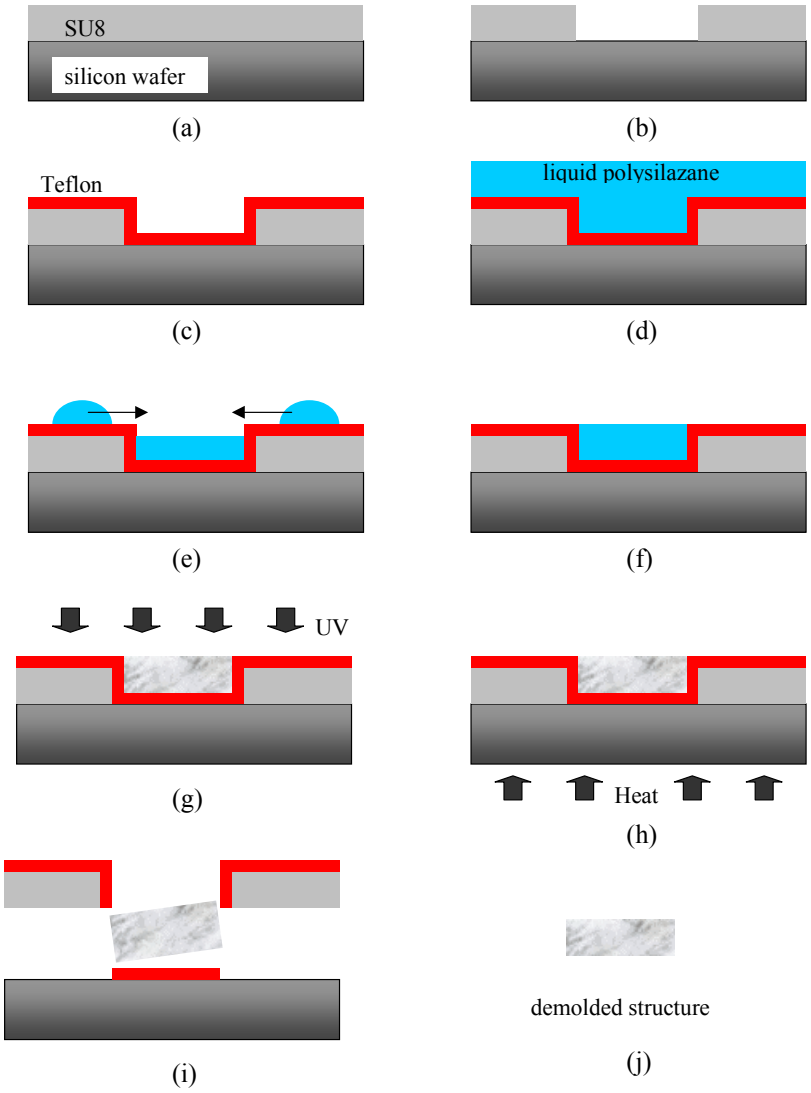

Figure T2- 3. Final Microcasting process.

(a) Apply SU8 photoresist on silicon wafer. (b) Pattern and develop SU8 to produce micro molds. (c) Apply Teflon layer by spin coating and curing. (d) Place liquid Ceraset™ on wafer. (e) Spin off excess liquid; liquid either accumulates in mold cavities or gets flung cleanly off the SU8 surface. (f) A filled mold with no excess liquid on the SU8 top surface results. (g) Solidify Ceraset™ by UV exposure. (h) Heat the wafer to about 250 °C in an oven. (i) The SU8 layer becomes unattached from the wafer, adhesion between the polysilazane structure and the SU8/wafer is weak due to the Teflon coating. (j) A free standing polymer structure results. The structure is then crosslinked and pyrolyzed to convert the polymer to SiCN.

Figure T2- 4 shows some representative structures, including electro-thermal actuator structures (see Task 5), which were fabricated in this manner. As shown in this figure, the structures fabricated with this process exhibit the high geometrical definition associated with SU8™- and LIGA-fabricated components, and, because these structures have been demolded, the yield from pyrolysis was usually 100%. This is thus a significant achievement of this project.

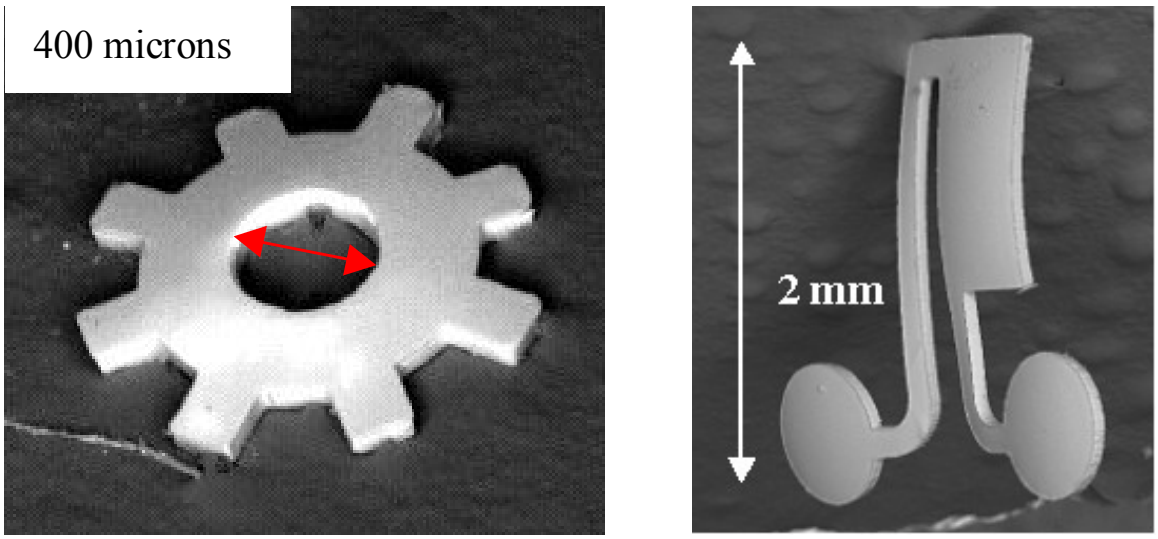

(a) (b)

Figure T2- 4. SEMs of SiCN structures fabricated using the Teflon-coated SU8™ mold process.

(a) Gear, 70 microns thick (b) lateral electro-thermal actuator, 100 microns thick.

Compared to soft-lithography method which has been used elsewhere to fabricate SiBCN micro components [H. Yang et al, *Advanced Engineering Materials, communications*, vol. 13, no. 1, pp. 54-58, 2001], our approach requires fewer processing steps and, because our method requires only one micro-patterning step, results in a more direct translation of mask dimensions to the fabricated structure, leading to potentially higher dimensional tolerances.

2.2 Development of the Direct-Photopolymerization Method

A separate polymer-micromachining process that evolved in parallel with the microcasting route is known as the direct-photopolymerization method. In this approach, a photoinitiator is added to the liquid precursor instead of a thermal catalyst to enable solidification from UV exposure via free-radical polymerization. There is thus no need for a mold at all since the polysilazane precursor can be directly patterned photolithographically as if it were a photoresist. Photopolymerization of PUMVS is a scientifically new phenomenon and recent efforts related to this project have involved study of the kinetics of this process, which involves fundamental research into polymer chemistry.

For the purposes of this project, 5 wt% of the photoinitiator 2,2 Dimethoxy-2-phenyl acetophenone ("DMPA") was added to the Ceraset™ precursor. This initiator was chosen because of its prevalent use in industry, its sensitivity to 365 nm wavelength used in UV photolithography, and its high polymerization efficiency, although other initiators have also been explored in this project. With the addition of the photoinitiator, the liquid precursor can then be directly patterned photolithographically through a mask. The precursor is thus akin to a negative photoresist in which the exposed areas polymerize. The remaining, unexposed precursor remains liquid and is washed away in acetone, leaving behind the polymerized structures on the silicon wafer. In order to allow for the high linear shrinkage during pyrolysis, the polymer components are removed from the wafer and placed, substrate-less, in the furnace. The method releasing the polymeric components from the underlying silicon wafer has been to scrape

them off the wafer using a surgical razor blade and inert silicone oil (from Dow Corning) as a lubricant. Alternatively, dry-etching of the underlying silicon wafer using xenon difluoride gas has also been successful due to the gas' high selectivity to silicon, whereas wet silicon etchants, like many of the solvents attempted for demolding, have been shown to adversely affect the polymerized structures.

Compared to the microcasting route, the direct-photopolymerization route has undergone only two major process iterations. The first consisted of non-contact photolithography (see DARPA technical report from June 2000), in which the glass photomask was placed some distance away from the liquid precursor (typically 1 mm) during exposure. The reason for this was to prevent contact between the liquid polysilazane and the glass, which would result in the polymerized polysilazane adhering very strongly to the glass, thereby destroying both the mask and the fabricated structure. Due to the separation between mask and polymer, the resultant structures exhibited sloped sidewalls, a problem which was more exaggerated in higher-aspect ratio structures (Figure T2- 5).

It was found that the sidewall slope could be reduced by use of a different initiator (see DARPA report from June 2001) such as a 2-part mixture of isopropyl thioxanthone (known commercially as Quantacure ITX, from Biddle Sawyer Corp.) with a concentration of 1.21 wt%, and 2-methyl-1-[4-(methylthio)phenyl]-2-morpholinopropanone-1 (known commercially as Irgacure 907) with a concentration of 0.6 wt%. The weight percentages used for this second initiator were suggested by the manufacturer as being the optimum percentages, beyond which initiator efficiency would decrease. However, despite the promising results from using this new initiator, it was found that the mask-to-wafer gap still dominated the slope of the sidewalls, as measured by the angle between the substrate and the sidewall using a profilometer. Table T2- 1 compares the sidewall angle for different conditions.

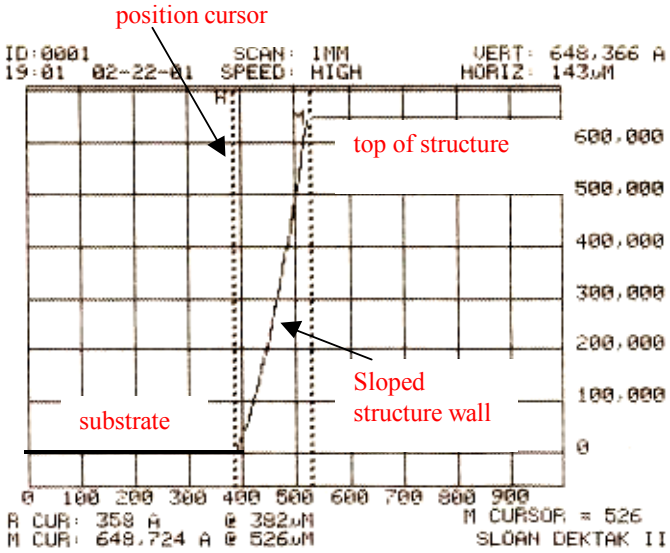

Figure T2- 5. Typical measured profile of a photopolymerized structure (polymerized using I-651 initiator).

Sample	Initiator	Mask to wafer gap	Theta (degrees)
1	B	2 mm	49
2	B	5 mm	29
3	A	5 mm	25
4	A	2 mm	45

Table T2- 1. Effect of varying photo initiator and mask-to-wafer gap on the sidewall angle, in the non-contact direct-photopolymerization fabrication process. Initiator A is DMPA, initiator B is ITX+I907.

As in the microcasting route, the key to the direct-photopolymerization route was the liquid Teflon solution that was now used to coat the glass photomask to enable contact photolithography to be preformed. The Teflon coating prevents the polymerized precursor from sticking to the glass mask, thus following photolithographical patterning the mask can be easily separated from the polymerized structures.

The improved process is shown in Figure T2- 6 (first reported in DARPA technical report from September 2001). First, a photomask is transferred to glass, which is then coated with a thin layer of Teflon (a). For this, the Teflon is spun onto the glass mask at 1500 rpm for 30 seconds, then the glass is placed in an oven and heated to 150-200 ^{o}C for 10 to 20 minutes. The liquid precursor (Ceraset^{TM}) is prepared by adding 5 wt% of the photoinitiator DMPA (Irgacure 651 from Aldrich Chemical), as described in our previous DARPA reports. The Ceraset^{TM} is then dispensed at an arbitrary volume onto a silicon wafer and left alone for several minutes to allow air bubbles to diffuse out of the liquid (a). Then, the glass mask, Teflon-coated side down, is placed *in contact* with the liquid precursor (b). Spacers may be placed on the wafer to keep the glass mask at a predetermined distance from the wafer, thereby setting the thickness of the fabricated structures. Alternatively, the mask may be placed on the liquid without the use of spacers, in which case the thickness of the fabricated structures is determined by the volume of liquid Ceraset^{TM} and its viscosity. The liquid is then exposed to UV for 30-45 minutes at an intensity of about 10 mW/cm^2. Following exposure, the glass mask is separated from the silicon wafer and cleaned in acetone (c). The Teflon-coating on the glass mask prevents adhesion with the precursor, and is thus the key to this improved process. Without the Teflon coating, the polymerized precursor would stick to the glass, being very difficult to remove. The silicon wafer is then spun at a high speed – about 5000 rpm for several seconds – to remove the unpolymerized liquid. Spin-rinsing in acetone or cyclohexane (d) removes the last remnants of unpolymerized liquid, leaving behind polymeric components on the wafer (e). The wafer is then re-exposed to UV for several minutes to harden the structures further, before they are scraped off the silicon with a razor blade using inert silicon oil as a lubricant (f) (see DARPA report June 2000). The structures are then sandwiched between sheets of paper, and a weight is placed on top overnight. The paper absorbs the silicone oil (which can be a contaminant during pyrolysis although it is inert to the precursor at the polymer stage) and the added weight ensures that the structures stay flat while they polymerize during the diffusion-limited "dark" reaction. The polymeric components may then be crosslinked and pyrolyzed as before to obtain SiCN.

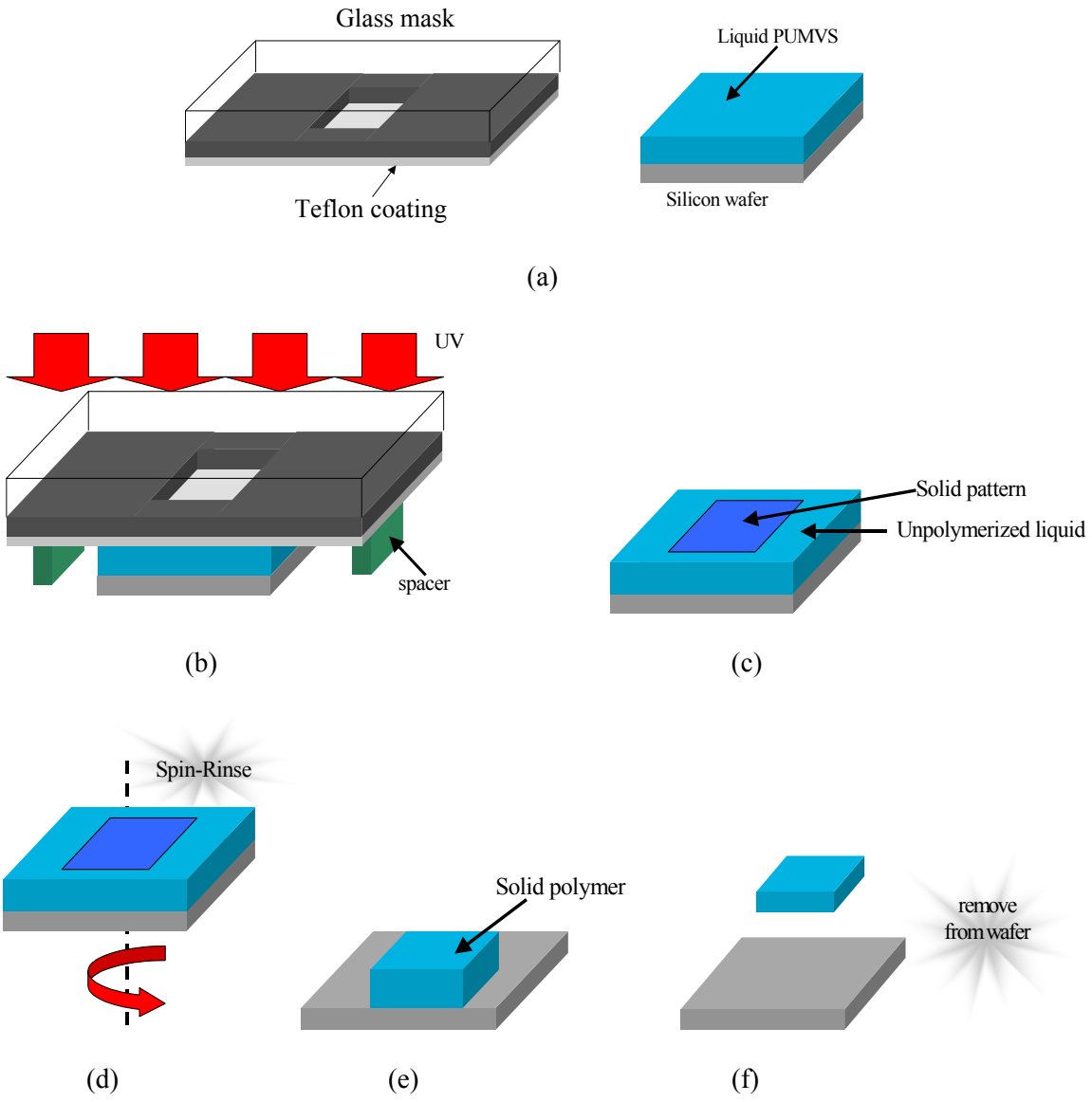

Figure T2- 6. Contact-photopolymerization fabrication process.

Figure T2- 7 shows some structures fabricated using the contact-photopolymerization process. As seen, the structures exhibit extremely vertical sidewalls and have excellent definition. Prior to this process, structures such as these would have been possible only by casting in SU8 molds which would have taken much longer due to the long bake times for SU8. Prior to Spring 2001, such structures would not have been possible at all. The Teflon-coating is thus the key to improving the photopolymerization process because it enables direct contact between the mask and the liquid during photolithography, thus eliminating effects such as light scattering and refraction associated with introducing an air gap in between the mask and the medium to be polymerized. Aspect ratios of up to 20:1 have been obtained using contact-photopolymerization; in addition, resolution seems comparable to that of SU8, that is,

features can be spaced closely without being joined at the base because the walls are so vertical. Furthermore, because the liquid polymer is bounded on either side by silicon or glass during UV exposure, the resultant structures have very planar surfaces, a feature that was lacking in the microcasting process unless polishing was performed. The resolution of contact-photopolymerization is limited by the optical equipment used such as the uniformity and degree of collimation of the UV source. Figure T2- 8 shows that this method can be used to fabricate non-high aspect ratios as well.

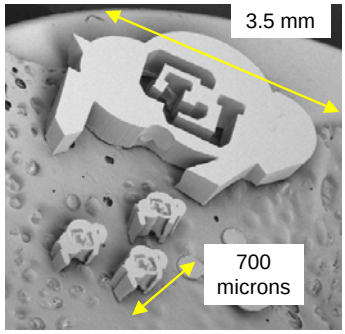

Figure T2- 7. Preceramic buffaloes, 500 microns thick, made using contact-photopolymerization.

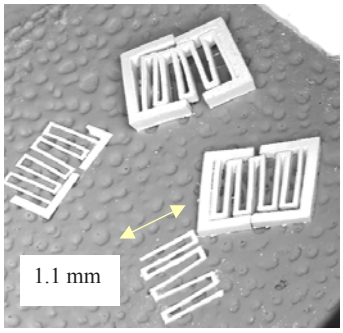

(a)

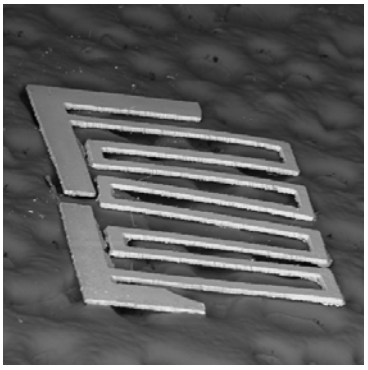

(b)

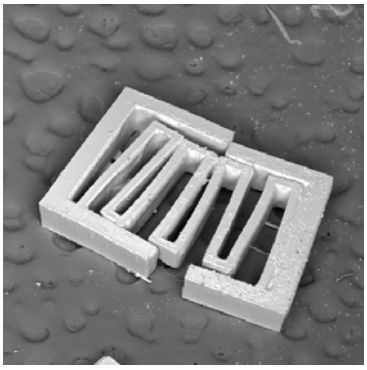

(c)

Figure T2- 8. (a) Low- and high-aspect ratio SiCN structures made using contact-photopolymerization.

(b) Closeup of a low aspect ratio structure, thickness ~ 30 microns. (c) Closeup of a high aspect ratio structure made using the same mask, thickness ~ 150 microns.

This drastic improvement in fabrication capability has several ramifications. First, this means that photopolymerization is the fabrication technique of choice for SiCN MEMS because it is much faster and simpler compared to microcasting. This is especially true for high aspect ratios which, if fabricated using microcasting, would require lengthy processing times for thick SU8™ layers. Also, because very flat and planar surfaces are easily obtained, this could lead to significant improvements in micro-optical components made from Ceraset™ as opposed to those made from microcasting (see Task 5). However, despite this big leap in photopolymerization capability, there are several considerations:

(1) The photopolymerization process still requires that the polymeric structures come into contact with liquid chemicals such as acetone because of the need for spin-rinsing. Spinning at high speeds alone for extended periods of time do not remove the last trace of unpolymerized liquid. It is very likely that this contact with acetone or other rinsing chemicals do affect the final SiCN properties by "contaminating" the polymer. Further efforts are necessary to identify the least damaging rinsing chemicals, that is, chemicals which would not contaminate polymerized Ceraset™, but in which liquid Ceraset™ is soluble.
(2) Use of a razor blade is still needed to remove structures from the wafer, thereby leading to the potential for mechanical damage (see DARPA report June 2001). However, it has been found that in general, during pyrolysis the material bonds to itself, thereby eliminating most "cracks" incurred at the polymerization stage. Experiments were done to eliminate the use of a razor blade by Teflon-coating the silicon wafer as well – however, that made spin-rinsing difficult as the polymerized structures would get flung off the wafer during spinning and be damaged. Rinsing would thus have to be done by immersing the wafer in a bath of rinsing solution, which further aggravates problem (1).
(3) Even though closely-spaced high aspect ratio structures are possible, the rinsing chemicals and the use of silicone oil create liquid capillary forces that pull closely-spaced features together. Long and thin structures, such as closely-spaced beams, are thus likely to be joined together following removal from the wafer. If pyrolyzed as such, the SiCN structure will also exhibit joined features. One way to minimize this problem is to re-expose the rinsed structures for an extended period of time or to allow them to set overnight before removal from the wafer. In this way the structures are more rigid when they are removed from the wafer, and are thus less likely to deform from liquid capillary forces. However, the more rigid the structures are during removal from the wafer, the more likely they are to crack.

Therefore, microcasting in Teflon-coated SU8™ molds offers the following advantages over the improved photopolymerization process:

(1) In microcasting, the precursor does not contact any chemicals, thus the resultant SiCN is purer.
(2) In microcasting, the lack of liquid chemicals (other than the precursor itself) ensures that closely spaced features do not stick together from liquid capillary forces.
(3) In microcasting, there is no razor-induced mechanical damage.

Overall, the direct-photopolymerization fabrication process is a fast, simple and versatile means of fabricating polysilazane and SiCN structures, but if chemical purity of the polysilazane is desired, then microcasting would be more appropriate.

3. Polymer-to-Ceramic Process

SiCN MEMS were initially pyrolyzed using the process established by Shah [S.R. Shah, PhD Thesis, University of Colorado at Boulder, Dept. Mechanical Engineering, 2000] for synthesizing bulk samples of PUMVS-derived SiCN for material characterization; however, due to heavy furnace usage eventually a

hot isostatic press ("HIP", model AIP 6-30H from American Isostatic Presses, Inc., Columbus, OH) was acquired specifically to process the MEMS samples. The HIP is a computer-controlled, fully automated high-temperature and -pressure furnace used extensively in ceramics processing.
The pyrolysis process used for the MEMS-related work therefore evolved separately from the process established previously for pure SiCN material samples. In the conventional processing route, the polymer precursor is first crosslinked in a warm isostatic press (WIP) under pressure. The application of pressure prevents formation of pores within the polymer, thus the final ceramic following pyrolysis is fully dense and defect free. Pyrolysis in the conventional process takes place in a tube-shaped furnace with flowing nitrogen. With the HIP, one has the advantage of being able to perform crosslinking and pyrolysis in the same furnace and within the same automated program. However, unlike the conventional process, pressure during crosslinking is applied not through silicone oil but through nitrogen gas, and during pyrolysis the gas does not continually flow over the samples (thus removing the gaseous byproducts from the chemical reactions within the material) but instead is static. This has the consequences that the gaseous byproducts may remain trapped within the material, leading to non-optimum composition and properties.
It is worthwhile to note that, like the polymer-micromachining process, this research went through many intermediate HIP processes before this final one was established. Time and pressure conditions were varied, and the elimination of the crosslinking step was also experimented with. The resultant materials for these early HIP processes were not characterized for composition, but qualitatively appeared similar to the SiCN processed via the conventional route.
Given that the temperature for pyrolysis was constant at 1000 ^{o}C throughout all process iterations, it is believed that the differences in composition probably lie in the amount of byproducts remaining within the HIP-processed samples. In the early HIP cycles the gas was not vented during pyrolysis but instead was retained throughout the entire process. The venting steps were eventually added to approximate flowing nitrogen, which serves to remove the evolving gases from the material. Samples processed in the HIP qualitatively appeared harder, more lustrous, and less brittle than those from earlier HIP processes. However, extensive characterization of properties for these materials as compared to those processed by the conventional route remains to be performed.

Despite the reduced times used for both crosslinking and pyrolysis, the resultant SiCN from the MEMS-route exhibits similar mechanical properties such as Youngs Modulus and Vickers Hardness, compared to the conventional route. Details on the HIP process are given in Task 1.

4. Additional Fabrication Techniques

4.1 XeF_2 Silicon Etching for Non-Mechanical Release of Polysilazane Structures Following Photopolymerization

Following polymer-micromachining by the direct-photopolymerization method, removal of the structures from the underlying silicon wafer is necessary to allow for shrinkage during pyrolysis. The simplest method for accomplishing this has been through a mechanical release process whereby the structures are "scraped" off the wafer using a surgical razor blade and silicon oil lubricant. While this method is effective for thick layers of simple and compact geometry, it is unsuitable for thin layers, and/or long and narrow features. These delicate Ceraset^{TM} structures commonly break during the mechanical release method. Furthermore, if the structures survived removal from the substrate, another technical barrier to overcome is that of preventing the capillary forces from the silicone oil (used as a lubricant during razor-blade application) from distorting the delicate structures. If the oil is omitted, then friction from the blade

would likely destroy the structures. Microcasting presents a "dry" fabrication alternative but the physical demolding process again poses a high risk of mechanical damage to fragile and/or thin structures.

Therefore, one logical solution would be to polymerize structures on a silicon wafer and then bulk-etch the wafer away from underneath the structures. However, the turbulent liquid forces during wet chemical etching would still likely break the structures. In addition, it has been found that silicon wet etchants such as EDP and KOH also corrode Ceraset^{TM}. One successful alternative is to use XeF_2 dry etching instead.

Xenon difluoride (XeF_2) is a recently-developed technique for etching silicon for MEMS applications [F.I. Change et al, *Proc. SPIE Conf. Microelectronic Structures and Microelectromechanical Devices for Optical Processing and Multimedia Applications*, Austin, TX, October, 1995, pp. 117-128]. Developed in the early 1990s, XeF_2 etching has been shown to possess the following advantages over wet etching:

1. Being a gas-phase etch, the problems of device stiction and damage from capillary forces are eliminated.
2. Due to XeF_2's nearly infinite selectivity to silicon, many materials that cannot withstand wet etchants can be used as masking layers for XeF_2 etching. These include photoresist, silicon dioxide, and metals such as aluminum, to name a few.
3. Being an isotropic etchant, mask orientation is not an issue, and in addition large areas can be undercut very rapidly which is especially useful if the purpose of the etch is to free structures from the underlying substrate.
4. Since it is a gas-phase etchant it is a much "cleaner" process than using wet etchants.

Since the mid 1990s, several MEMS research groups around the world have used XeF_2 etching of silicon, each custom-building their own system. In 2000, the first commercial XeF_2 etcher was made by Xactix, Inc.(Pittsburgh, PA). This machine was based very closely on the system implemented by the Berkeley MEMS group. The cost of one of these fully-automated and computer-controlled commercial machines is presently about $100,000.

In contrast, a less sophisticated though fully functional system was designed and built here at University of Colorado (by one of the graduate student researchers on this DARPA project) for about $8000. The design of this system closely resembles that built by Dr. David T. Read at the Materials Reliability Division of the National Institute of Standards and Technology (NIST) in Boulder, Colorado.

Figure T2- 9 shows the design of the XeF_2 etcher built at C.U for this project. Like the NIST system, our etcher is based on pulsed etching (a concept first developed by the Berkeley group) but with the metering of gas based on time rather than on pressure as used in the Berkeley group. Therefore, there is no feedback loop to control the cycle as is found in the commercial etcher, instead the etching cycle is timed. This means that uniformity, repeatability and controllability of the etching process will understandably not be as high as that in the commercial system, but through process characterization this etcher has been found to work well with reasonable repeatability based on the mass of XeF_2 crystals used.

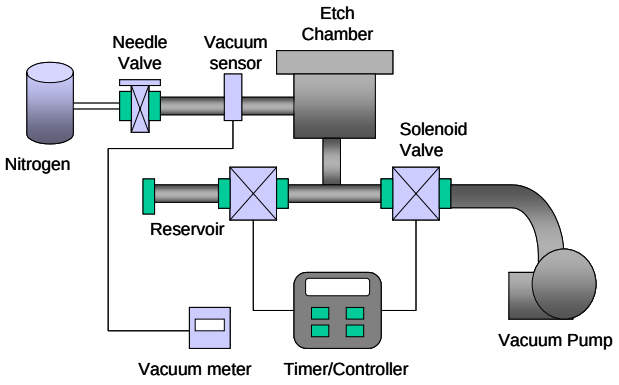

Figure T2- 9. Schematic of the XeF_2 etching system designed and built at University of Colorado.

Figure T2- 10 is a photograph of the XeF_2 etcher, which is located under a fume hood in a cleanroom for safety. Several improvements to the NIST design were implemented in this system: a manual Teflon needle valve is used for connection to nitrogen so that the flow-rate of nitrogen during post-etch nitrogen purging can be controlled to protect thin suspended structures. All the components in the system are standard off-the-shelf components found mostly from the Cole-Palmer catalogue or from the on-campus chemical supply store. The only exception is the vacuum chamber that was custom-designed for size and placement of parts. The vacuum chamber is designed to be much larger than it needs to be for versatility to accommodate large wafers. But for the purposes of most of this research, large aluminum blocks were placed in the chamber to increase the pressure of the gas. The standard load-lock door with glass viewport is fitted to the chamber for easy loading of samples and viewing of the etch progress. The load-lock door and the custom-made vacuum chamber were obtained from Kurt J. Lesker Co. All the vacuum ports are designed for standard NW-25 fittings. All vacuum connections are stainless steel, and all valves as well as the vacuum pump are specially rated for corrosive chemicals. The timer/controller turns the solenoid valves on and off in a timed sequence, but purging and flushing the chamber is done manually.

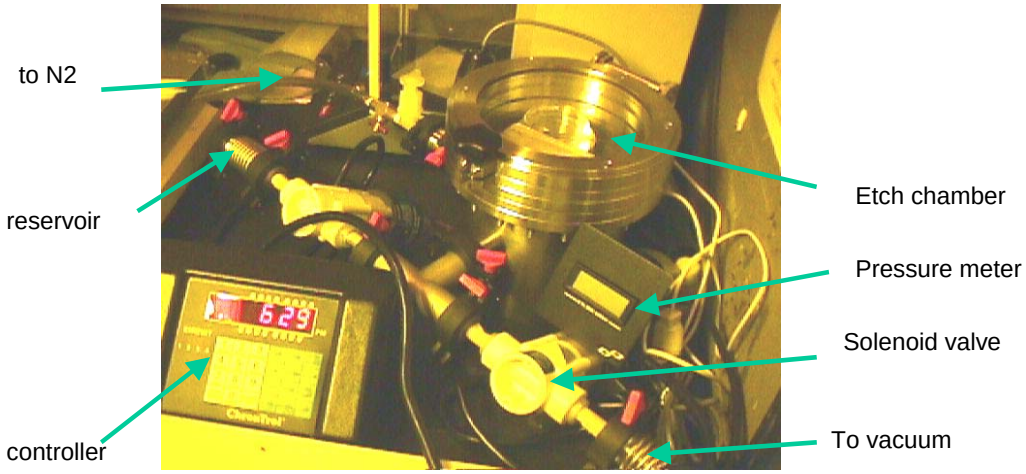

Figure T2- 10. Photograph of XeF_2 etcher.

The programmed pulsed etching cycle, developed for this system, consists of the following steps:

1. The vacuum valve opens for 1 minute so that the chamber is pumped down to a pressure of about 20-50 mT.
2. The vacuum valve closes, then the reservoir valve opens for 3 seconds to allow fresh sublimated XeF_2 vapor to enter the etch chamber. (After the first 3 cycles, this time lengthens to 5 seconds so that the etch pressure may be kept more consistent throughout the duration of the program)
3. All valves are closed for 1 minute, during this time the etching occurs.
4. The program then returns to step 1 to remove the etch byproducts (xenon and silicon tetrafluoride gases). The cycle repeats until the program is turned off by the operator.

In addition, the reservoir and etch chamber have to be manually purged with nitrogen several times before and after the etching. XeF_2 crystals are placed in the reservoir prior to etching. Typically, each etch requires 0.05 – 0.2 grams of crystals. The machine also allows the operator to manually override the programmed etch cycle, and/or to manually control the etching via opening and closing of the valves.

XeF_2 etching was successfully used in the fabrication of free-standing polysilazane beams with layer thickness as thin as 8 microns. Ceraset™ comb-drive structures were photopolymerized on silicon as usual. To create the thin layers, the liquid was spun at 1500 rpm for 15 seconds and the glass photomask was placed directly on the liquid without any vertical spacers. Following photopolymerization and spin-rinsing, the structures were re-exposed to UV for several hours, then left on silicon for a period of several days in order to fully polymerize. The wafer was then cut into smaller pieces, which were placed in the XeF_2 etcher and etched with 0.2 grams of XeF_2 crystals (corresponding etching time ~ 1.5 hours). Immediately prior to etching, the samples were dehydrated on a hotplate at 110 ^{o}C for 10 minutes, a routine process to ensure that XeF_2 does not react with moisture on the sample. Thicker structures were also fabricated and released from the silicon wafer in this manner. Results are shown in Figure T2- 11. Furthermore, the structure shown in this Figure is designed to enable pyrolysis to be done while the structure is still attached to the handling silicon wafer, thereby increasing the fabrication yield. The comb-drive structure is attached to the non-underetched Ceraset™ layer by four short tethers. Thus, after XeF_2 etching the entire device, while being completely suspended, is still attached to the wafer. During pyrolysis the non-underetched Ceraset™ will crack due to the 30% linear shrinkage (see DARPA report Jan 2000), but the suspended device will not, being allowed to shrink. The effect of the shrinkage will be to break the four tethers, thus freeing the device from the substrate.

Note the upward warping of the comb-drive beam. This indicates that film-stress is present in the material as early as immediately following photopolymerization. The origin of this stress could be due to uneven polymerization, the density of cross-links being higher toward the top of the film where the UV light originates.

Also shown in Figure T2- 11 (c) and (d) are SEMs of thicker structures that have been photopolymerized on silicon and underetched. As seen in this Figure, the beams are completely suspended, but due to the thicker layer do not warp.

Therefore, the use of a custom-built XeF_2 silicon-etching system has enabled the fabrication of thin-film polysilazane – and possibly SiCN – devices that have not been realizable using previously-developed fabrication techniques. In addition, the XeF_2 etcher designed and built by the personnel of this project is now central to at least two other funded MEMS projects at C.U. Boulder. More details can be found in the DARPA technical report from June 2002.

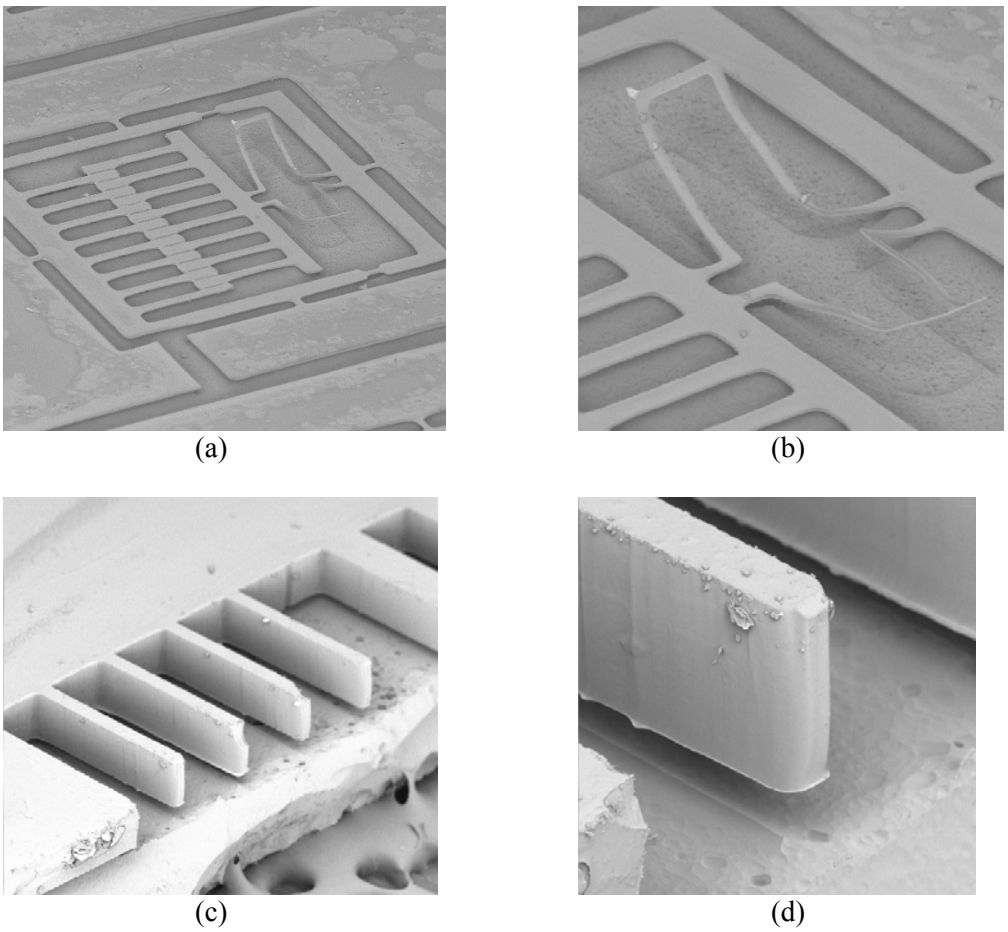

Figure T2- 11. SEMs of Ceraset™ structures on silicon following release by XeF_2 etching.

(a) Comb-drive structure, the width of each finger is 20 microns, and the Ceraset™ layer thickness is 8 microns. (b) Closeup of the released flexure, warping from film stress. (c) Cantilever beams of width 30 microns. (d) Closeup of a beam, showing that it is completely suspended.

4.2 Macro-Scale Casting

Finally, it is worthwhile to realize that molds for casting of polysilazane do not have to be obtained from batch photolithography techniques. Raj et al [S.R. Shah and R. Raj, J. American Ceramic Society, vol. 80, no. 10, pp. 2208-2212, 2001] used the processing route developed by Shah [S.R. Shah, PhD Thesis, University of Colorado at Boulder, Dept. Mechanical Engineering, 2000] for casting liquid PUMVS precursor into millimeter-sized Teflon molds to produce bulk specimens of SiCN. Many applications could benefit from millimeter- scale polysilazane and SiCN components that might be more easily cast into larger molds. Examples are components for MEMS packaging - SiCN and polysilazane are excellent material candidates for MEMS packaging due to the high-temperature stability and flexible casting/photopolymerization based manufacturing. An example is the polysilazane tube shown in Figure T2- 12. This millimeter-sized tube would be valuable in microfluidics packaging, especially if the

microfluidic channels were to be made from SiCN, for instance as high-temperature microfluidic and microchemical reactors for micro power generation applications.

The tube shown was fabricated by casting. The inside of a small glass tube (of inner diameter 1.5 mm) and a syringe needle were coated with the liquid Teflon. The tube and needle were simply dipped in the liquid Teflon and then heat-treated. Ceraset^{TM} containing DMPA photoinitiator was drawn into the tube, the syringe needle (held by a fixture) was inserted into the middle of the tube, and the assembly was exposed to UV, which penetrated the glass tube to polymerize the precursor, as illustrated in Figure T2-12. Following polymerization, the assembly was heated in an oven at 140 ^{o}C for several hours to make the polysilazane more rigid. Then, the syringe was removed and the polymer tube was pushed out of the glass tube.

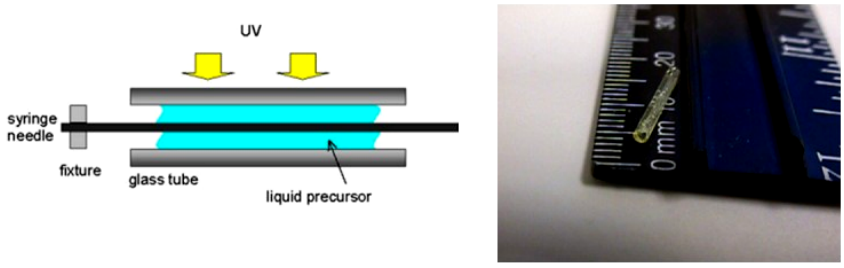

Figure T2- 12. Photograph of a polysilazane tube, and schematic of the fabrication. Length: 1.5 cm, outer diameter: 1.47 mm, inner diameter: 0.82 mm.

4.3 PECVD of PUMVS

Another fabrication technique that was briefly explored is deposition of SiCN films using plasma-enhanced chemical vapor deposition (PECVD) using PUMVS precursor (first reported in the DARPA technical report from June 2002). Amorphous Si-C-N has been produced elsewhere by chemical vapor deposition [D. Mocaer el al, *J. Material Science*, vol 28, pp. 2639-2653, 1993] using tetranethylsilazane system, and microwave plasma-assisted PVD [A. Badzian et al, *Thin Solid Films*, vol 354, pp. 148-153, 1999]. The technique of interest here is PECVD using the Ceraset^{TM} precursor, which has not been demonstrated before, but which is desirable because of its availability for this research.

In attempting PECVD as an alternative, the idea is to obtain SiCN directly from the liquid precursor, the energy for this reaction being supplied by the plasma rather than by high-temperature.

Why would we want to deposit SiCN thin-films? These thin-films can already be obtained via spin-coating of the liquid polymer precursor followed release from the wafer via XeF_2 etching of the underlying substrate. However, after pyrolysis the resulting SiCN devices are separated from the wafer, which is undesirable when reduced feature sizes are desired (smaller than 30 microns for example). Thus, being able to fabricate SiCN directly on a substrate is highly desirable so that pick-and-place of individual devices can be eliminated. SiCN could then be more readily integrated into the rest of the MEMS fabrication/packaging infrastructure, which would be important commercially and technologically. The motivation for exploring PECVD is thus to achieve a deposition process for SiCN thin-films directly, without the need to undergo a polymer-to-ceramic pyrolysis step.

This route was only very briefly explored in this project, and as such the results are far from complete but are presented here to suggest one possible direction for future research.

Figure T2- 13 shows a photograph of the system used. A silicon wafer was mounted on a chuck (using double-stick tape) that was then positioned in the middle of the reaction chamber. A syringe containing pure Ceraset^{TM} precursor - i.e. without photoinitiator or thermal catalyst as is usually used for MEMS fabrication - was attached to the nozzle at the top of the chamber. The chamber was then evacuated to a pressure of about 500 mT and Argon gas was flowed into the chamber while the pressure was maintained. Cooling water was turned on and the RF power source was adjusted for resonance, i.e. maximizing the output power while minimizing the reflected power. This generated a plasma in the middle of the reaction chamber. Drops of CerasetTM were then allowed to enter the chamber due to the low chamber pressure which sucked in the liquid. Upon entering the plasma, the precursor broke down and deposited as a film on the silicon wafer.

The results obtained appeared promising but inconclusive due to the limited time spent on this technique. Films were successfully deposited on silicon wafers, but were highly non-uniform and their chemical composition was not determined. The size of the wafers were one-quarter of an inch or smaller (due to the diameter of the reaction chamber), and for a deposition time of several minutes the film thickness across each wafer ranged from several nanometers to about 2 microns, as estimated visually under a microscope since the films were too rough for measurement by laser interferometry. Furthermore, the film ranged in color from a lustrous black (similar to bulk SiCN) to dull brown or gray.

Many aspects of the experimental procedure remain to be determined and refined. For example, there was a high probability of air leaking into the chamber due to the manner in which the precursor-containing syringe was mounted to the nozzle on the reactor. Vacuum pressure, Argon flow rate, deposition time, RF power, substrate preparation etc. are other parameters that should be controlled and studied. Another important issue is thermal management of the substrate. The silicon wafer typically heated up to at least 200 ^{o}C. If this process is to be compatible with other MEMS fabrication/packaging processes in the future, it would be necessary to reduce the wafer temperature so that techniques such as photoresist processing can be integrated.

Despite the preliminary nature of these results, this technique appears promising and would be a good candidate for future research.

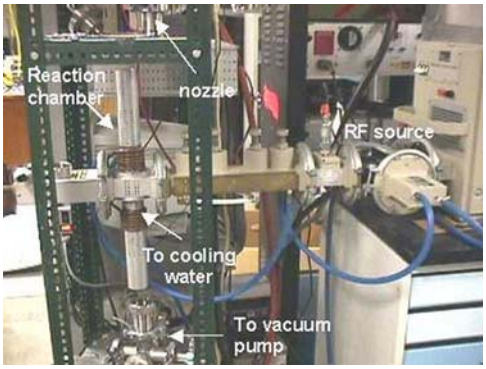

Figure T2- 13. Photograph of PECVD system.

Task 3: Multi-Layer Technology

Content:

1. Casting in Multi-Layer Net-Shape Molds
2. Multi-Layer Photopolymerization
3. Polymer-Based Bonding

We have developed three distinct methods for fabricating multi-layered MEMS-scale structures from SiCN and its polysilazane precursor.

1. Casting in Multi-Layer Net-Shape Molds

In this approach, a first layer of SU8™ photoresist is patterned on a silicon wafer but is not developed so as to prevent unwanted topography in the layer above; a second layer of photoresist is then applied and patterned under a mask aligner, and finally the double-layered photoresist structure is developed. Bake times for the second layer are doubled compared to the manufacturer's specifications to account for the lower heat conduction through the underlying first layer of photoresist. The SU8™ photoresist mold is then coated with Teflon and microcasting and demolding proceed as in the case for single-layer microcasting (see Task 2). This technique was first reported in the DARPA technical report from June 2001.

Figure T3- 1 shows the CAD layout of a MEMS fuel atomizer, and Figure T3- 2 shows the fabricated devices. The atomizer is based on the design that of silicon and SiC atomizers fabricated at Case Western Reserve University. Although erosion tests indicated that the SiC atomizers exhibited higher erosion resistance than the silicon devices, the SiC atomizers were fabricated using CVD, thus the process was expensive and technically challenging especially given the high aspect ratios needed. Therefore we claim that the SiCN atomizer combines both the high-temperature functionality of SiC with low cost fabrication.

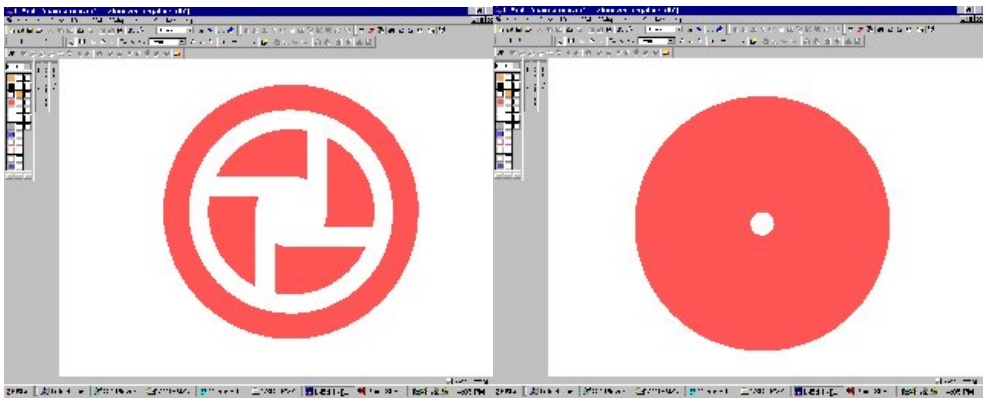

Figure T3- 1. (a): mask for 1st layer SU8 mold, outer diameter = 2 mm. Channel width = 150 microns. (b): 2nd layer SU8 mask.

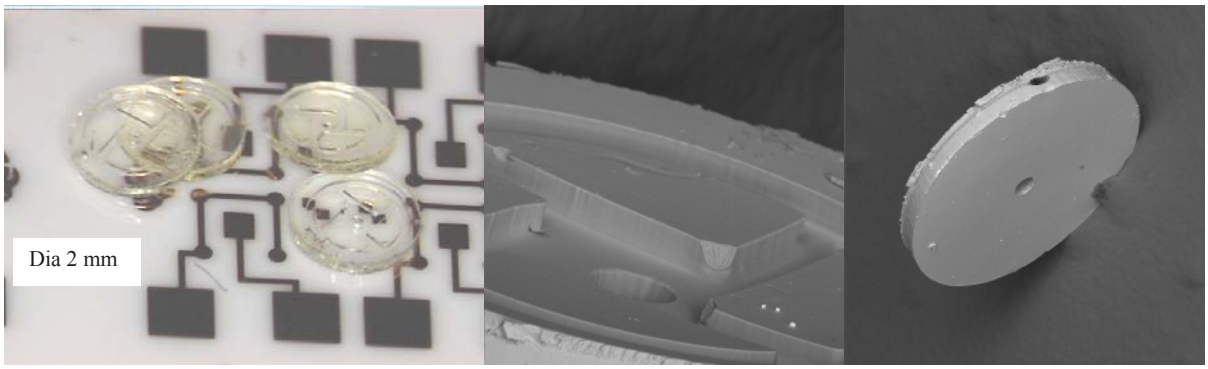

(a) (b) (c)

Figure T3- 2. (a) Pre-ceramic atomizers, outer diameter 2 mm.

This picture illustrates an optically transparent fluidic structure, which has the potential for flow visualization applications. (b) SEM of a pyrolyzed SiCN atomizer. The gouges are due to tweezer handling while the structure was still in the softer polymer state. (c) Underside of atomizer, showing the through-hole.

When designing double-layered molds, the cavities in the top layer should be larger than, and overlap, those on the bottom layer so that the net mold-structure can be developed and the cast structure can be demolded. This process can be extended to triple- or multi-layered molds; however, the bake times necessary for processing multiple SU8™ layers, which can increase to more than six hours for a double-layered mold depending on the layer thicknesses, can make this technique extremely time-consuming.

2. Multi-Layer Photopolymerization

A much faster and simpler way to fabricate multi-layer structures is by successively applying and polymerizing layers of precursor on top of each other, using the direct-photopolymerization method. Thus, polymerized structures are built upwards in a manner similar to stereolithography. This may be peformed under a mask aligner in order to align the features of the various layers; however, the mask aligner available for this research had a very limited depth-of-focus and, along with other operational setbacks, was unsuited to this fabrication method. Specifically, the barrier to success lay in these three key problems:

1. Ceraset™ is transparent, thus aligning a second layer on top of a first, already patterned layer was very difficult because features could not be seen under the mask-aligner.
2. Equipment was severely limited – the mask aligner available for use in this project was limited in its depth of focus. Ceraset™ and SiCN layers have to be fabricated at a thickness of at least several tens of microns if the final parts are to be manageable during packaging; however, this distance was too great to achieve focus in the mask aligner. In other words, aligning a second layer to a first was not possible because of the limited capabilities of the mask aligner's microscope.
3. Unlike commercial photoresists which are hard baked before exposure, Ceraset™ is a liquid before and during the exposure process. Thus the material thickness has to be set by the presence of vertical spacers to determine the height of the mask. During mask-aligning, contact between mask and liquid is problematic – it is messy because moving the mask results in the liquid overflowing off the edge of the wafer and possibly adhering to parts of the machine, or due to viscous forces the substrate might also move, or air bubbles might be introduced into the liquid.
4. Ceraset™ can be likened to a negative photoresist, i.e. areas to be solidified are exposed while everything else is masked. This means that typically most of the wafer will be masked, leaving

only small openings in the glass photomask through which to see the underlying features on the first layer. While this technical problem is encountered in SU8™ fabrication as well, when compounded with problems (1) to (3), the hurdles that needed to be overcome for successful multi-layered photopolymerization of Ceraset™ were daunting.

Of course, use of a stereolithography machine would be a viable technique for creating multi-layered structures, but access to this equipment was not possible at the time of this project.

A partial solution has now been found (first reported in the DARPA technical report from June 2002), which does away with the mask aligner altogether. So now, aligned multi-layers are possible, but only if the features are large (at least 100 microns across), and if alignment tolerances are coarse (several tens of microns or larger), and if design is a negative structure, i.e. the main features to be aligned are masked (or UN-photopolyermized) areas. Basically, the mask aligner was replaced by the same UV-exposure system that has already been in use for much of this project's duration, with the only difference that a stereomicroscope was incorporated into the system and mask alignment was done essentially by hand. Figure T3- 3 shows this set-up. The use of a stereoscope as opposed to the mask aligner's optical microscope virtually eliminated problem (2) while minimizing problem (3) because the user has direct control over the substrate at all times during the aligning process. Problem (1), while not completely eliminated, was less of an issue since the view through the transparent liquid is clearer under a stereomicroscope.

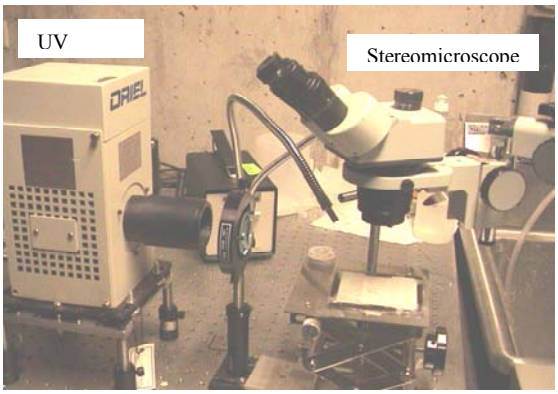

Figure T3- 3. Modified UV-exposure system for multi-layered photopolymerization.

This set-up was used to fabricate double-layered polysilazane microfluidic channels as part of a thermopneumatic actuator array – see Task 5. The fabrication process was as follows: (1) the alumina substrate on which the microfluidic channels were to be built was patterned with the necessary gold traces as well as alignment marks for the Ceraset™ fabrication. The substrate was placed on a glass plate (covered with wax paper to prevent adhesion between substrate and plate should the liquid overflow during poymerization). Liquid Cersaet™ was dispensed on the substrate, glass slides were placed on the plate on either side of the substrate as vertical spacers, and the Teflon-coated glass mask was placed on the spacers, directly in contact with the liquid. The plate was then moved to the exposure stage and the stereomicroscope (with positionable fiber-optic light sources) was placed over the assembly. The stereoscope had to be mounted on a separate bench from the exposure system since it was not to be a permanent part of the set-up. Spatulas were then used to move the substrate from under the mask in order to align the mask to the gold alignment marks on the substrate. One problem encountered is that the mask could

move after alignment due to the liquid capillary forces. But unlike the mask aligner, once aligned there are no moving parts contacting the mask to possibly misalign it during exposure. Following exposure, this process was repeated for a second layer of Ceraset™ and then the substrate was spin-rinsed in acetone to wash away the unpolymerized liquid. Following this, the entire assembly was again exposed to UV to fully-polymerize the material. Crosslinking could be then included if desired, but it was found unnecessary for the purposes of building a working prototype. See Task 5 for a more detailed description and photographs of the thermopneumatic actuator.

This technique worked well for fabricating microfluidic channels because the structure is a negative design – i.e. the features to be patterned are the channels or masked regions, while the majority of the mask is clear. This makes it relatively easy to see through the mask to the underlying alignment marks. A positive-designed structure would be much more difficult to fabricate because then most of the mask would be covered, with only small openings with which to see through to the alignment marks.

Therefore, ideally the use of a better mask aligner or a stereolithography system would still be preferable for fabricating multi-layered structures, but was not possible during this project.

This multi-layer photopolymerization technique was used to fabricate several SiCN MEMS-scale devices such as the combustion chamber, caps for MEMS packaging, and double-layered polysilazane microfluidic channels – see Task 5 for photographs and descriptions of these devices.

3. Polymer-Based Bonding

While the above two methods enable multi-layered structures to be fabricated, these structures are still inherently two-dimensional due to the layered approach. Polymer-bonding is a way to fabricate not only multi-layered but also truly three-dimensional polysilazane and SiCN structures. Two or more free standing polysilazane components are first fabricated by either microcasting or direct photopolymerization routes. Following demolding or removal from the substrate, these polymer structures can then be bonded together using the same liquid Ceraset™ as an adhesive. When this "green" structure is pyrolyzed, the resultant SiCN is a single monolith. In this way, through either manual or robotic assembly, micro- and meso-scale three-dimensional structures may be built. Figure T3- 4 shows a structure fabricated using this method. This is, to our knowledge, the most geometrically complex ceramic MEMS-scale structure to have been fabricated to date.

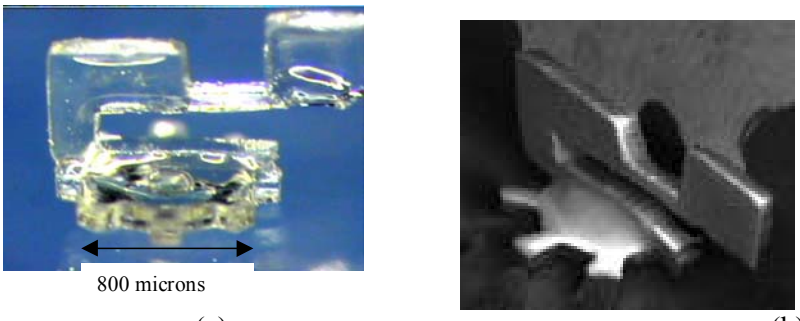

(a) (b)

Figure T3- 4 (a) Photograph of a complex three-dimensional pre-ceramic structure fabricated by bonding a gear and thermal actuator, both fabricated by Teflon-coated SU8 mold method. (b) SEM of the same structure following pyrolysis.

This method has also been used to fabricate the SiCN pressure sensor membrane, see Task 5. Also, any combination of these three methods can be used to create complex three-dimensional SiCN and polysilazane MEMS structures, at lower cost compared to CVD-based methods for SiC, for example.

Task 4: Design Knowledge Base

Content:

1. Development of Room-Temperature Microindentation Methods for Measuring Mechanical Properties of SiCN.
    - 1.1 Development of microindentation method (DARPA report Jan 2000)
    - 1.2 Use of microindentation for 3-point bending test on SiCN (DARPA report Jan 2001)
    - 1.3 Hardness testing of annealed SiCN (DARPA report June 2001)
    - 1.4 Digital Image Correlation and Calibration of micro tensile testing load frame (DARPA report June 2001)
    - 1.5 Error Analysis of Micro Tensile Testing and DIC (DARPA report Sept 2001)
    - 1.6 Measurement of E in SiCN using Micro Tensile Testing and DIC (DARPA report Sept 2001)
2. Measurement of SiCN-SiC composite properties
3. Fabrication issues
    - 3.1 shrinkage
    - 3.2 warping
    - 3.3 whisker formation from annealing (DARPA report June 2001)

This section describes the development and use of microindentation methods to measure mechanical properties of MEMS-scale SiCN samples. In addition, several key issues that arise during fabrication that need to be addressed for MEMS design, were investigated.

1. Development of Room-Temperature Microindentation Methods for Measuring Mechanical Properties of SiCN.

1.1 Development of Microindentation Method

Experiments were done to quantify room-temperature mechanical properties (Vickers Hardness, Youngs Modulus) of the SiCN using an instrumented microindentation technique. The idea (first reported in the DARPA technical report from Jan 2000) is to continuously measure the load vs. penetration depth during indention of a material. When coupled with appropriate analysis, a wide range of mechanical properties can be inferred. In support of this project, we purchased a commercial microindentor; it was delivered and set up at the end of December 1999. We have developed data reduction techniques to extract elastic moduli for use with ball indentors. An example of the type of data obtained from microindentation tests is shown in Figure T4- 1. Figure T4- 1(a) shows an indentation after the load has been removed in a 100 micron thick SiCN sample using a Vickers indentor. Figure T4- 1(b) shows the measured load vs. penetration depth curve during the indent process (loading and unloading). A key difference between our approach and existing approaches is the treatment of the small, finite dimensions of microcast samples. This is a significant issue with regard to mounting samples and obtaining repeatable material measurements.

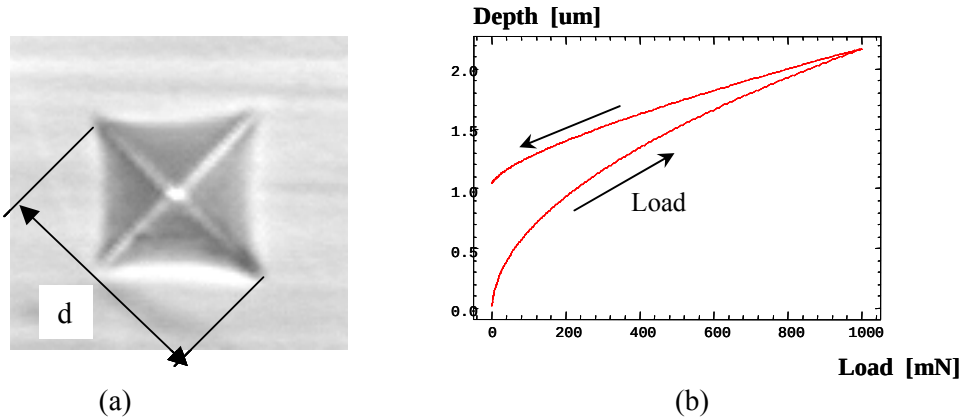

Figure T4- 1. (a) Optical micrograph showing the Vickers indentation after load removal (d = 3 microns); (b) load-indentation depth curve.

We have also measured elastic moduli of bulk SiCN samples as a function of porosity (recall that the microcast samples are fully dense). Figure T4- 2 shows the measured Young's and shear moduli as a function of density.

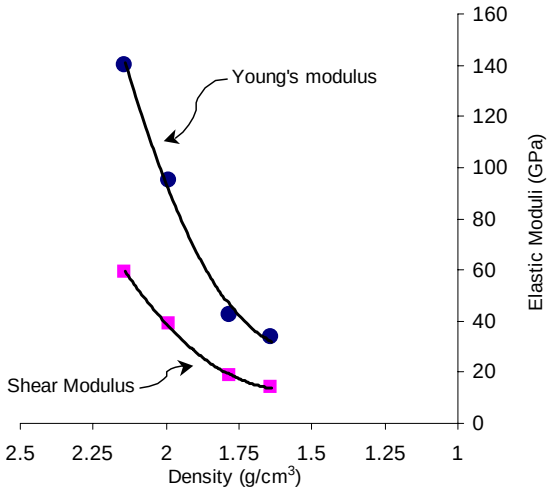

Figure T4- 2. Young's and shear moduli of bulk SiCN samples measured by pulse-echo ultrasonics as a function of material density.

1.2 Use of microindentation for 3-point bending test on SiCN

The microindentation system was used to measure the strength of SiCN MEMS-scale beams via three-point bending tests, as first reported in the DARPA technical report from Jan 2001.

From the force-displacement curve as shown in Figure T4- 3, the slope k can be calculated to get the critical force Fc. Analytical equations are then used to calculate Young's modulus and Strength.

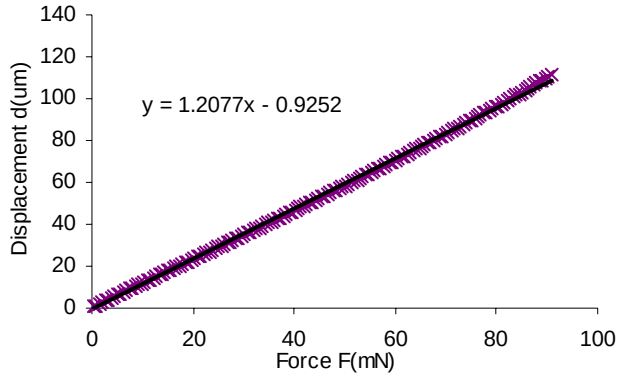

Figure T4- 3. Theoretical force-deflection curve for three-point bending test.

Three-point bending test design:

In order to remove the effect of indentation depth and use Eulor beam theory, the experimental setting was designed with following features:

- Small thickness bending beam (30~50 μm)
- Large span (2500~3500 μm)
- Large deflection (100~300 μm) under small loading (<100 mN)
- Negligible indentation depth (~0.5 μm)

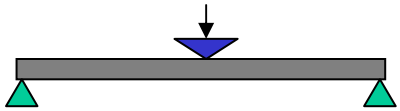

Figure T4- 4. Schematic of three-point bending experiment.

Test stage:

In the stage design, we did not use triangle wedges as supporters. Instead, a pair of sharp vertical edges were machined and stuck on a glass substrate with the required span. Notches were cut along the diameter of the support collar of the indentation head to allow space for the deflection of the beam ends. Figure T4-5 illustrates this concept.

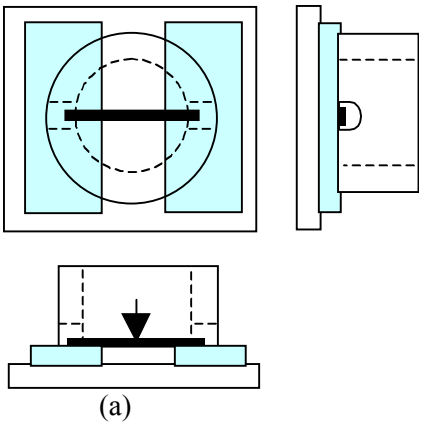

(a)

Edge profile

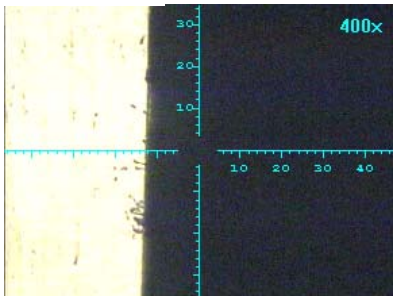

(b)

Figure T4- 5. (a) Schematic of stage and notch. (b) photograph of the edge.

Experimental results:

10 samples made by the direct-photopolymerization (see Task 2) were tested. The slope and critical force for each curve can be obtained from the plot shown in Figure T4- 6.

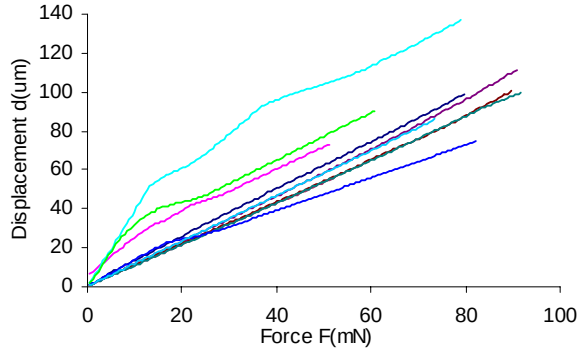

Figure T4- 6. Results of three-point bending tests. Sample dimension: L=1610 μm, w=220~260 μm, h=26~37μm

The average dimensions for 10 samples were found to be: Length=1610 μm, width =230 μm, height =30μm. From these, the average modulus of SiCN was calculated to be 147 GPa, and the average strength was 874 MPa. The scatters of the result are also plotted, in Figure **T4- 7**. Table T4- 1 gives the actual measured values of each sample.

Sample	1	2	3	4	5	6	7	8	9	10	Average
Fmax	79.7	51.2	52.5	79.6	90.8	89.9	91.7	82.1	73.4	60.9	75.18
k=h/F	1.221	1.225	1.063	1.491	1.208	1.092	1.093	0.849	1.162	1.252	1.166
E (Gpa)	138	137	158	113	139	154	154	198	145	134	147.0
Strength(Mpa)	930	597	613	929	1059	1049	1070	930	856	711	874.4

Table T4- 1. Measured values for each sample in the three-point bending test.

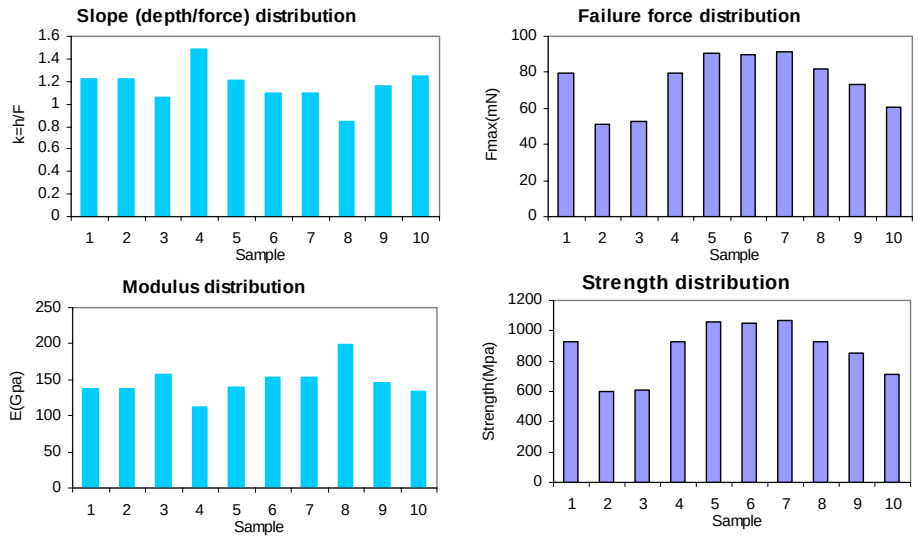

Figure T4- 7. Distribution of SiCN properties obtained from three-point bending tests.

For beams fabricated by direct-photopolymerization, there may be a variation in thickness due to the uneven spreading of the Ceraset layer on the substrate. Since thickness is a very sensitive parameter for the three-point bending test (Moment inertia $\propto h^3$), this represents one difficulty in the three-point bending experiments. Other defects in individual samples may cause the scatter in the data as well.

1.3 Hardness testing of annealed SiCN

If annealed at 1400 ^{o}C after pyrolysis, the SiCN becomes electrically conductive (see Task 1). However, the surface of the conductive ceramic is no longer shiny and smooth as it was after pyrolysis, because of the substantial increase in surface roughness from escaping hydrogen. An indentation test was conducted to determine if the mechanical properties of the annealed material differ from those of the as-pyrolyzed state. This was first reported in the DARPA technical report from June 2001. Unfortunately, due to the surface roughness and curvature, accurate measurements could not be made. The value of Vickers hardness ranged from 0.5 GPa to 5GPa even on the same sample surface. Even though the hardness values vary within the same sample, the overall hardness is much lower than that of non-annealed SiCN. Figure T4- 8(a) and (b) show two typical indents on the annealed ceramic surface. (c) Shows the reference image of a well-defined indent on an as-pyrolyzed SiCN surface with Vickers hardness around 14GPa for comparison. One reason for the substantial decrease in the hardness is the voids and bumps formed during the 1400 °C heat treatment.

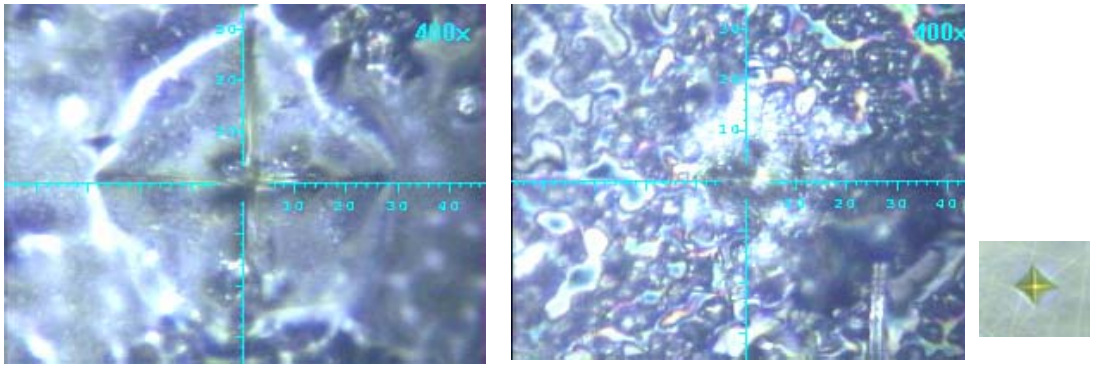

Figure T4- 8. Typical indents on (a) and (b) annealed and (c) non-annealed SiCN sample surface.

1.4 Digital Image Correlation (DIC) and Calibration of Micro Tensile Test Apparatus

The basic concept of digital image correlation is that by comparing digital images of the sample under testing from before and after deformation we can determine a displacement mapping that brings them into registry. The key assumption is the intensity distribution across a region to be correlated is unique and unaffected by deformation, except that it is deformed. These results were first reported in our DARPA technical report from June 2001.

Let the intensity fields before and after deformation be: G(X,Y), g(x,y)
Then the position of a point before and after deformation is: (x,y)=(X,Y)+(u,v)
The key assumption of DIC is therefore: g(x,y)= g(X+u,Y+v)= G(X,Y)

Components of DIC Measurement System:
Load frame: Microtensile load frame is used
Imaging system: Microscope and CCD camera
Data acquisition and post-processing system

Force Calibration of Microtensile Load Frame:

Force calibration is critical in order to obtain accurate force measurements during micro tensile testing and calculation of the longitudinal modulus and strength.

Force calibration steps, see Figure T4- 9:
Before calibration, the fixed platform is removed. The eddy sensors used to measure force are placed in the cross-head block facing the moving platform.
A holder connected with a string to the bonding plate is fixed to the moving platform.
A level gauge is used to ensure that the test apparatus is placed vertically during calibration.
A known weight is added incrementally to the mass holder.
After the reading is stabled, the voltage change of the force sensors is recorded both manually and automatically using LabView program.
A linear correlation of the applied force with the voltage reading is established as shown in Figure T4- 10.

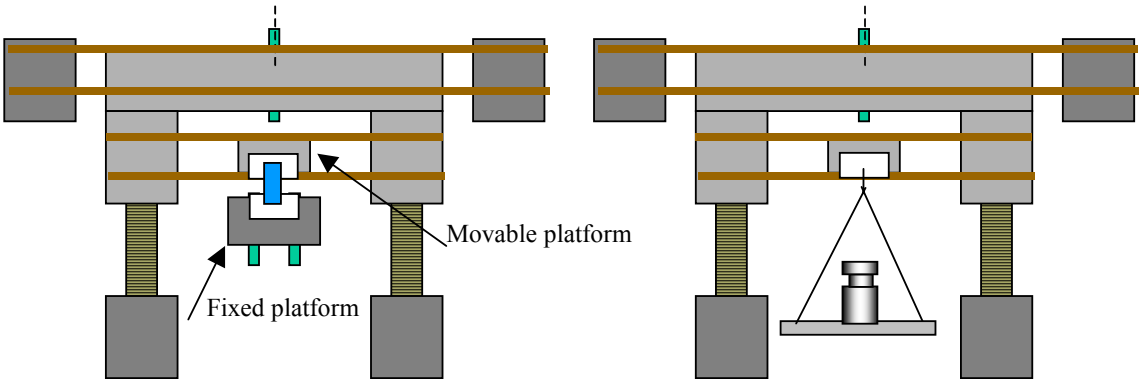

Figure T4- 9. Schematic of micro tensile apparatus and force calibration.

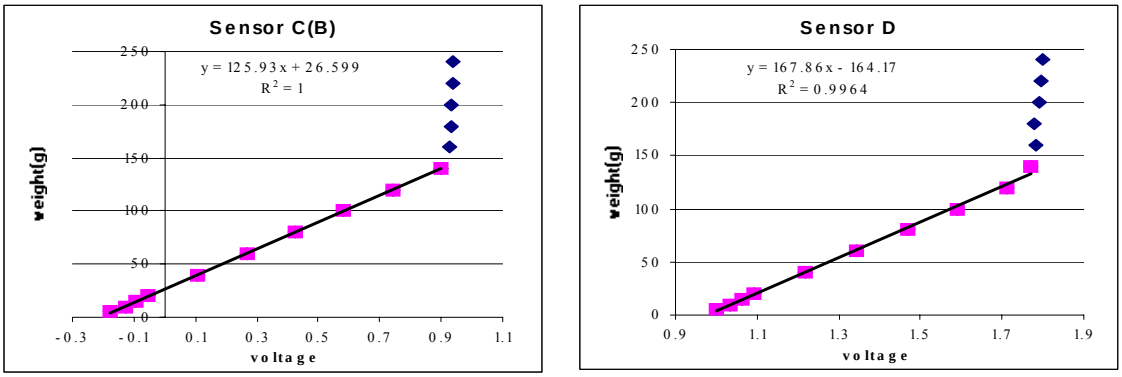

Figure T4- 10. A typical linear calibration curve fitting of the applied force with the sensor voltage reading.

Results of Force Calibration:

Figure T4- 11 compares the force calibration factors obtained through repeated calibrations, indicating that the calibration constants are consistent. The latest calibration value obtained is used as the parameter inputs.

Calibration of force

	D(gf/volt)	C(gf/volt)
old calibration	156.52	163.98

May 20, 2001 ------June 10, 2001

	D(gf/volt)	C(gf/volt)
calibration-1	161.53	125.93
calibration-2	162.99	126.73
calibration-3	162.16	127.70
calibration-4	161.44	125.60
calibration-5	163.06	126.84
DEVSQ	2.39	2.73

*DEVSQ:
Sum of squares of deviations of data points from their sample mean

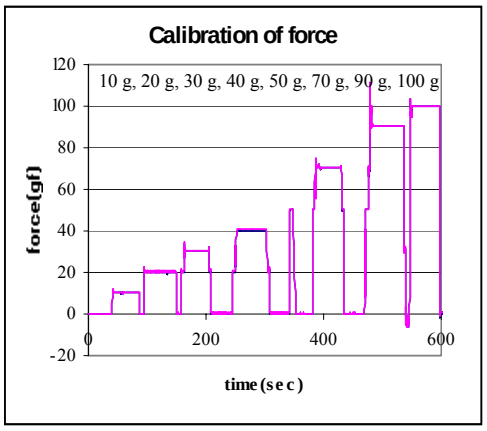

Figure T4- 11. Force calibration results.

Total Displacement Calibration of Micro tensile Load Frame:

Through taking DIC images of the translated movable platform, the relation between the displacement sensors A, B and the total displacement are established. Displacement calibration is necessary for keeping balanced movements of the two piezoelectric actuators. Results of displacement calibration are shown in Figure T4- 12.

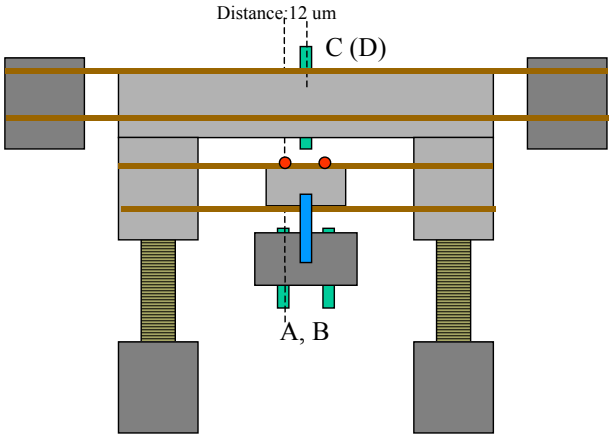

	A(um/volt)	Distance	Date
old calibration	28.53	~	2000 or before
calibration-1A	33.06	12mm	June 12,2001
calibration-2A	25.09	6mm	June 13,2001
calibration-3A	**25.27**	12mm	June 14,2001
average	27.81		

	B(um/volt)	Distance	Date
old calibration	28.50	~	2000 or before
calibration-1B	41.14	12mm	June 12,2001
calibration-2B	33.84	6mm	June 13,2001
calibration-3B	**35.85**	12mm	June 14,2001
average	36.94		

Figure T4- 12. Total displacement calibration of micro tensile testing load frame

Micro Tensile Testing and Data Acquisition:

Considering both the capability of the micro tensile-test apparatus and the difficulty of handling small samples, an optimal size for the SiCN tensile test specimens was chosen. Figure T4- 13 shows the mask design for the tensile test specimens, the dimensions given are those estimated after the 30% linear shrinkage of SiCN following pyrolysis.

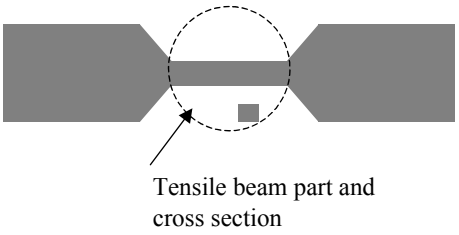

Dimension of the tensile beam part:

•Length: L= 400~450 μm

•Width: w= 70~80 μm

•Thickness t=40~45 μm

Note: Designed after shrink dimension is 400 × 70 ×40. However, the real dimension is not very accurate.

Figure T4- 13. Mask design of SiCN micro tensile test specimen.

Figure T4- 14 shows SEMs of SiCN test specimens for micro tensile testing. Specimens were fabricated using both microcasting and direct-photopolymerization methods.

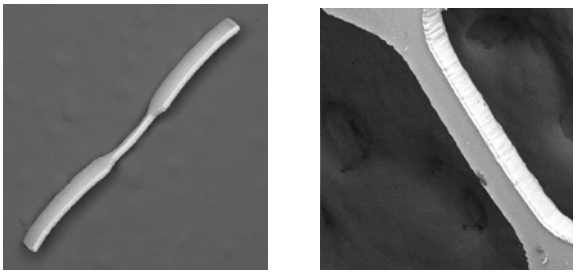

(a) (b)

Figure T4- 14. (a) SiCN micro tensile test sample fabricated by microcasting. Width of the narrow beam section is about 70 microns. (b) Closeup of the beam section.

We use the LabView™ program to control the displacement of the loading frame, acquire sensor data and convert them into force and total displacement. The software packages IMAQ configuration™ and Snapshot14.vi™ are used to take the images via a CCD camera during sample deformation.

Sample preparing and data acquisition steps:

1. The CCD camera orientation is adjusted to make sure the image frame is parallel to the spring in front of the force sensor.
2. The camera position is then fixed.
3. A pair of bond plate is fixed to the load frame.
4. The test structure is aligned with the CCD image frame.
5. Adhesive is applied to the bond plate and brought close to the ends of the sample frame.
6. The adhesive spreads and fills the space in between the test structures and the bond plates by capillary forces.
7. The adhesive is cured for over an hour.
8. The sample is loaded and images are taken for the DIC process.

Digital Image Correlation (DIC):

After tensile testing, the software **Yale DISMAP-2D 2000** is used to carry out the single image pair DIC. The corresponding DIC result can be converted into spreadsheet file. In this file, there are six variables: **u(x,y), v(x,y), du/dx(x,y), dv/dy(x,y), rotation(x,y).** At present, we use only the displacement variable u(x,y) to derive longitudinal strain. First we draw a chart of "displacement-u verses position-x ". Then a linear curve is fitted to get the slope as strain du/dx, Figure T4- 15.

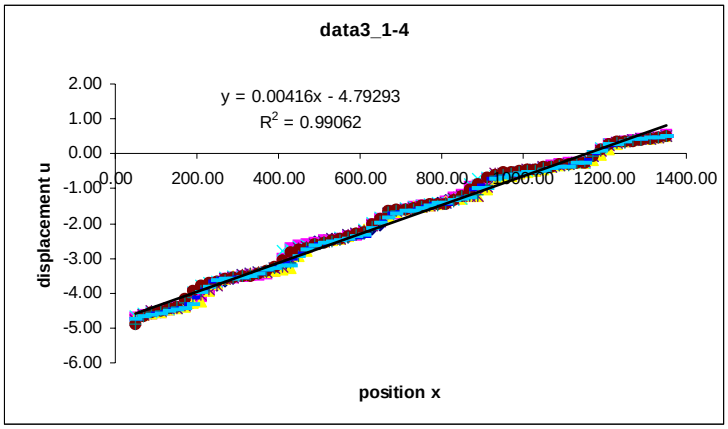

data1_	*Strain(du/dx)*
1	0
3	0.00300
4	0.00462
5	0.00641
6	0.00784

Figure T4- 15. DIC results of typical silicon tensile test sample.

From DIC of an artificial synthetic image of known strain, we find that when strain is smaller than 0.001, the fluctuation phenomena seen in Figure T4-15 can cause large errors as shown in Figure T4- 16 and Table T4- 2. When both strain and stress at different loading levels are known, the longitudinal modulus can be calculated.

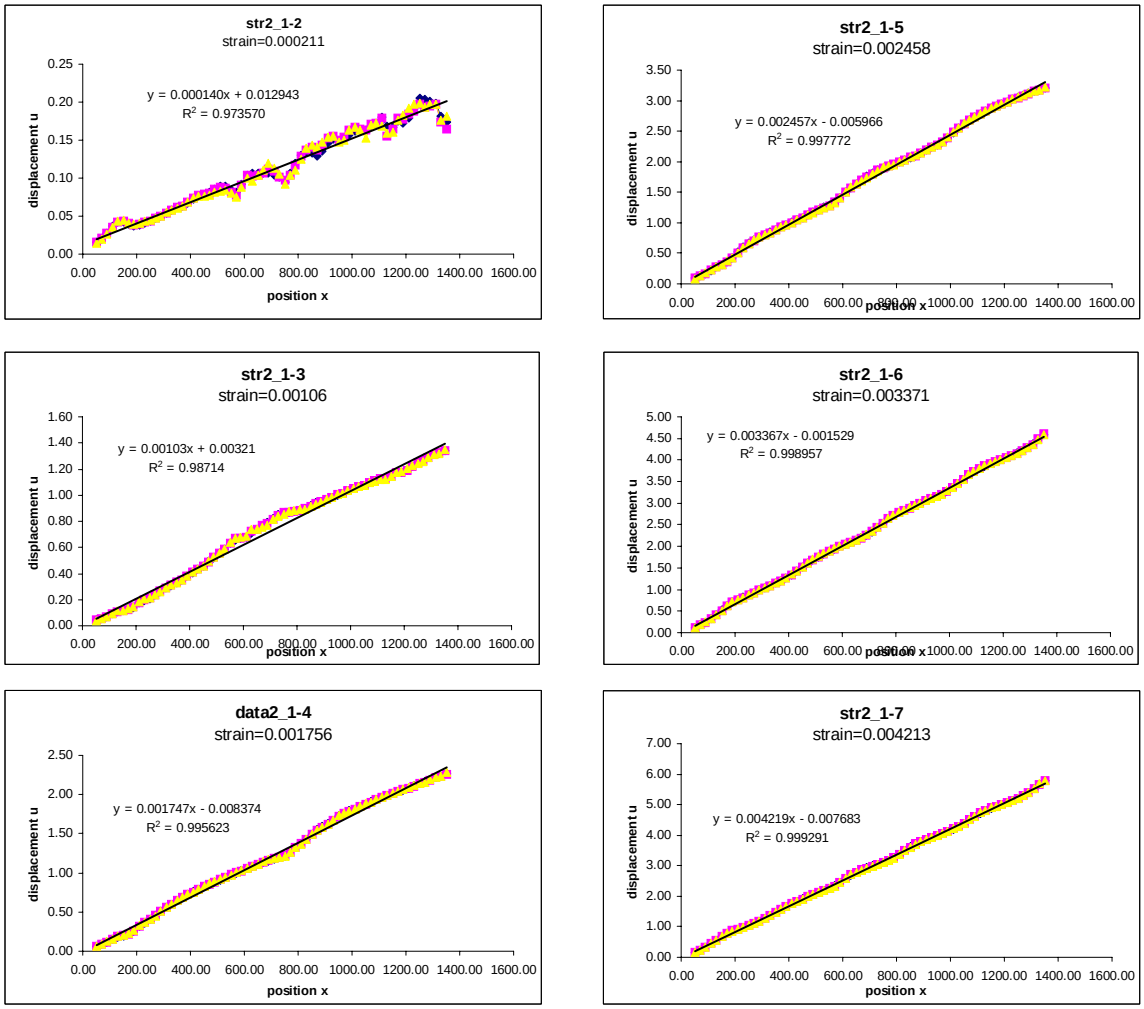

Figure T4- 16. DIC results of artificial synthetic image with different strain.

Periods of Fluctuation (Total pixel in longitudinal direction =1300)

Data	Strain	Periods	Stretch	Strain	Periods
2_1-2	0.00018	0.23	2_1-2	0.00021	0.27
2_1-3	0.00088	1.14	2_1-3	0.00106	1.38
2_1-4	0.00162	2.11	2_1-4	0.00176	2.28
2_1-5	0.00252	3.28	2_1-5	0.00246	3.20
2_1-6	0.00334	4.34	2_1-6	0.00337	4.38
2_1-7	0.00430	5.59	2_1-7	0.00421	5.47

Image	Periods	Real strain	DIC strain	Error(%)
Str2_1-2	0.27	0.000211	0.000140	-33.65
Str2_1-3	1.38	0.001060	0.001030	-2.83
Str2_1-4	2.28	0.001756	0.001747	-0.51
Str2_1-5	3.20	0.002458	0.002457	-0.04
Str2_1-6	4.38	0.003371	0.003367	-0.12
Str2_1-7	5.47	0.004213	0.004219	0.14

Table T4- 2. Periods of fluctuation in DIC.

1.5 Error Analysis of Micro Tensile Testing and Digital Image Correlation

A quantitative knowledge of the error associated with measurements is crucial when reporting measured property values. Thus, we have analyzed the error inherent in the micro tensile testing and digital image correlation procedures and equipment.

DIC Error of Artificial Synthetic Images :

Using Digital Image Processing functions in Mathematica™, a deformed image with uniform strain compared with the original image can be artificially synthesized. Since we know the relative deformation, pairs of artificial synthetic images can be used to study the accuracy and resolution of the DIC analysis software. Figure T4- 17 shows an image that was used as an original image for DIC error analysis.

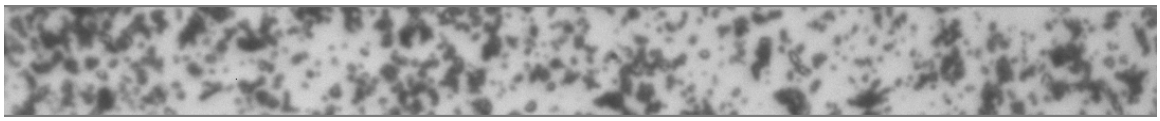

Figure T4- 17. Original image for artificial synthetic images serial (1424 × 121 pixel)

In Figure T4-18, image 0 to image 20 span an artificial strain range of 0.015, which is a large enough elastic strain for most of brittle material, e.g. silicon and SiCN ceramic. We can see that the absolute error of strain is within 0.00015. The relative error of strain decreases with increasing strain (Figure T4- 19). The relative error is smaller than 2% if we use strain data larger than 0.001. Therefore the DIC software itself is reasonably accurate.

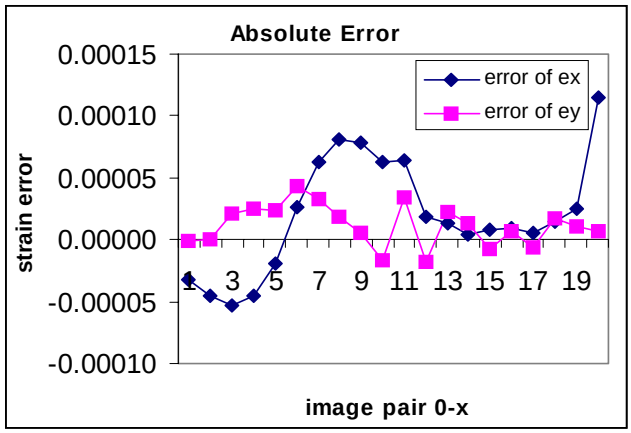

Figure T4- 18.DIC absolute error of strain

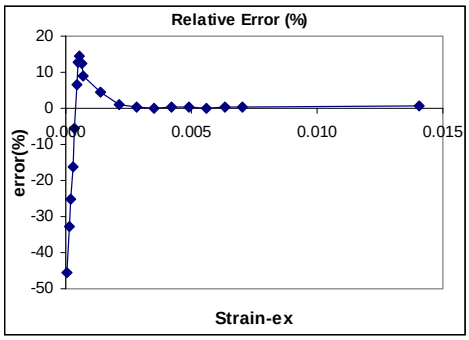

Figure T4- 19. DIC relative error of strain

Error Caused by Micro Tensile Test System:

(a) Strain Error due to Defocused Images

In order to obtain more accurate results or detailed information of strain distribution, a large magnification objective is preferred in the optical system used with the CCD camera to perform DIC. However, the depth of focus for such large magnifications is very small. The micro sample has dimensions ranging from 10 to 1000 μm. To fulfill the capacity of our 1.6M pixel CCD camera, we use an objective of 40× with a depth of focus around 1.7 μm. Because of the instability of the loading frames as well as optical system, the image tends to be out of focus during the testing. Defocusing not only degrades the image quality in spatial resolution but also causes deformation of the image, which produces an additional strain error in DIC result.

Figure T4- 20 shows a schematic of the optical system used in DIC. The focus distance between objective and sample can be changed randomly or systematically during testing because of the movement of the optical system and loading frame, which can be as large as several microns. The out-of-plane displacement of a typical micro-scale tensile test sample itself is only around 0.1μm, and thus can be omitted in error analysis.

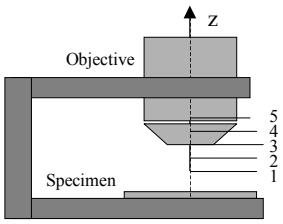

Figure T4- 20. Optical focusing system

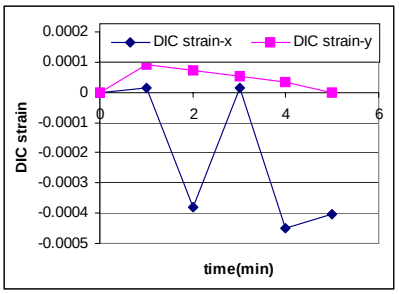

Figure T4- 21. Error due to instability of optical focusing system

(b) Defocusing Caused by Instability of Optical Focusing System.

Even though the loading frame is undisturbed before applying the load, the movement of the camera shutter opening and closing can cause defocusing. In Figure T4- 21, we can see that the error is randomly distributed. The strain error caused by the instability of the optical focusing system is smaller than 0.0003 for our system. Since this random error is small compared to the systematic error, it is negligible in the following analysis.

(c) Defocusing Caused by Focal Distance Change

First three definitions are needed: The strain of the test sample caused by the stress is called **real strain** which is unknown. The **DIC strain** result is composed of real strain and an additional **fake strain,** which is caused by the deformation of CCD image of the sample due to defocus.

In order to give a quantitative measurement of the effect of defocusing on the fake strain, we manually adjust the focus distance between the sample and objective. Because there is no load and real strain in these cases, the DIC results represent only fake strain. From image-1 to image-8 in Figure T4- 22, the objective was lowered gradually towards the tensile sample. From observing the images, we find that the images go from defocused to focused, repeatedly. Also, the sample image gradually increases in size even though the sample itself does not. This means that the fake strain is positive, as shown in Figure T4- 23(a).

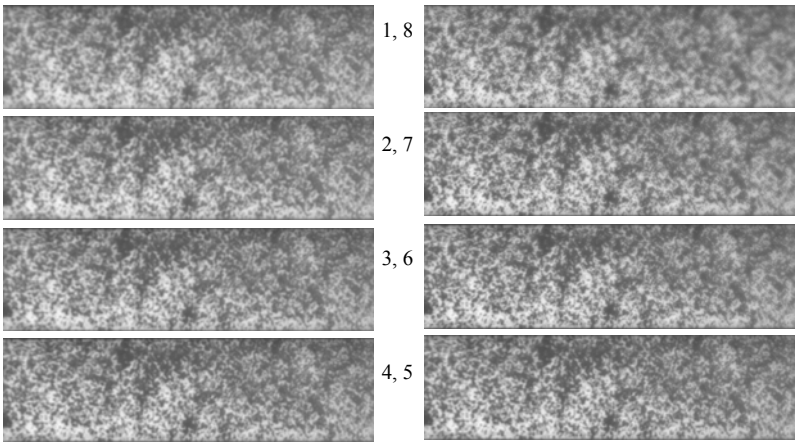

Figure T4- 22. Serial defocused images controlled by manually adjusting the focus distance in z. direction.

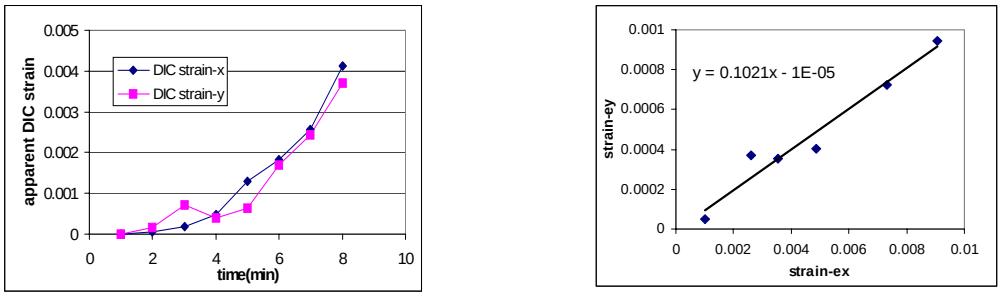

(a) (b)

Figure T4- 23. (a) Fake strain. (b) Fake strain in practical test

Only by adjusting the focusing system and gradually lowering the objective do fake strains appear in both x and y directions with comparable values. Thus the defocusing does cause fake strain and has to be considered. We can also assume that the fake strains in both x and y directions have about the same values if sample is not tilted under the objective.

A typical DIC result for a simple tensile test, shown in Figure T4- 23(b) is difficult to interpret. Both longitudinal strain (ex) and lateral strain (ey) cannot be positive as it appears in the Figure. The explanation is that during the tensile test the loading frame with sample mounted on it moved out of plane towards the objective, thus the positive fake strain gradually increased in both directions. Since the fake strain is larger than the real negative lateral strain, the apparent DIC lateral strain, which is the combination of a positive fake strain and a negative real strain is also positive and increasing.

Therefore we have found that there is a tendency for positive fake strain in our DIC system. The fake strain can cause 10~ 25% under-estimation of longitudinal modulus and cannot be eliminated.

(4) Effect of Objective Magnification on Defocusing Error

The depth of focus for the objective with magnification of 20× is around 3.5 μm, which is twice that of the objective with 40× magnification. So the 20× objective should give better results with respect only to fake strain verses degree of defocusing. See Figure T4- 24. The 20× objective defocus range is almost five times that of 40× with same fake strain. However there are also tradeoffs to using a lower magnification, in that lower magnifications will sacrifice the image spatial resolution and thus the DIC resolution.

Objective Magnification: 40 ×

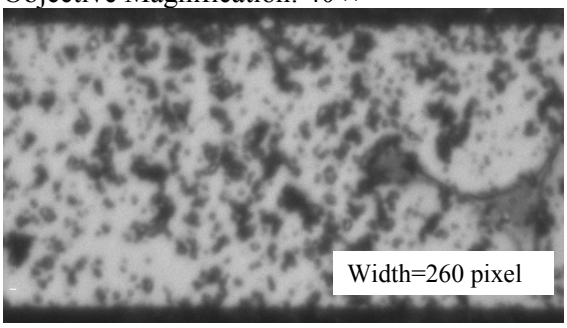

Objective Magnification: 20 ×

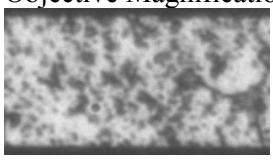

Width=110 pixel

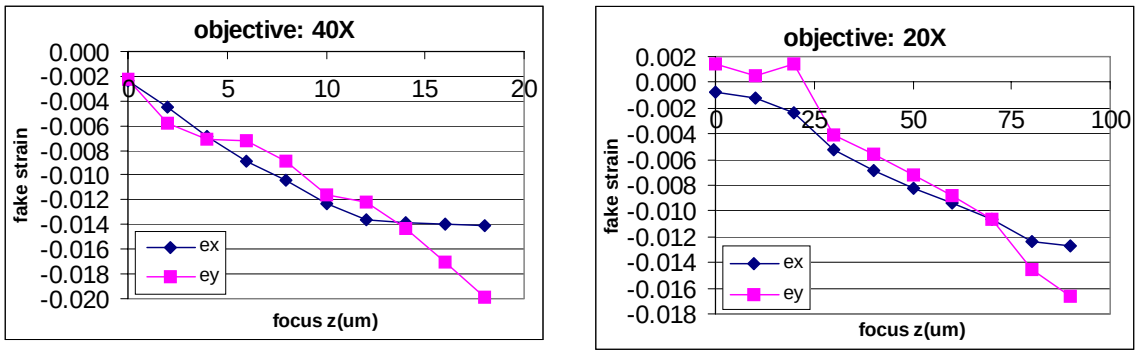

Figure T4- 24. Effect of objective magnification on defocus error

(5) Defocusing Error due to Misalignment and out of Plane Movement of Loading Frame

Even for the same tensile sample, the degree of defocusing varies unpredictably from one test to another. Figure T4- 25 shows DIC strain results for three tests of one sample.

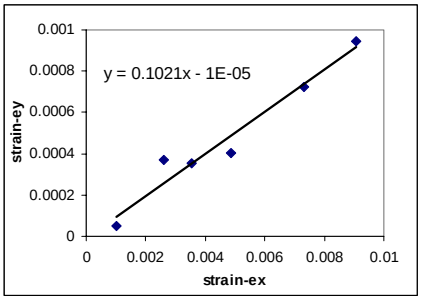

(a)

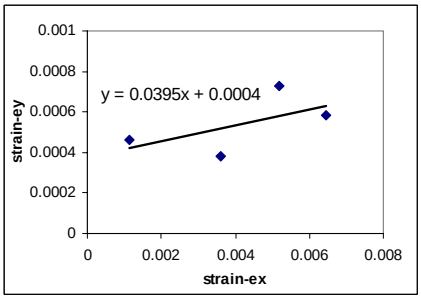

(b)

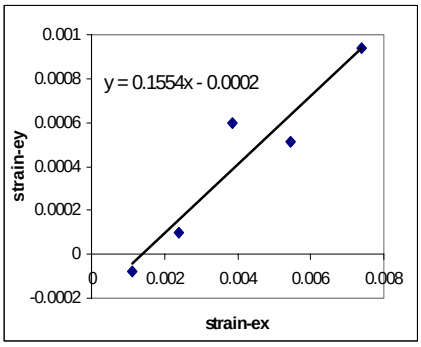

(c)

Figure T4- 25. Corresponding DIC strain in x and y direction for three tests on one sample.

Correction of defocusing error by solving equations:

Techniques to correct for errors in DIC due to defocusing have been developed and are outlined below:

(1) Assumptions:
Additional fake stains are caused by parallel defocusing of DIC images.
At any point, fake strains in both x and y directions are the same.
Poisson's ratio of the test material is known.

(2) Correction of defocus error

Following is the code used to correct the strains:

ϵ_x : du/dx, DIC strain in longitudinal (x) direction, $\epsilon_x = \epsilon_{x1} + \epsilon_{x2}$ (1);

ϵ_{x1} : real longitudinal strain
ϵ_{x2} : fake strain caused by out of focusing of DIC images
ν : Poisson's ratio. For epitaxial sillicon, $\nu_{<110>} = 0.06$, $\nu_{<100>} = 0.28$;
ϵ_y : dv/dy, DIC strain in lateral (y) direction, $\epsilon_y = \epsilon_{y1} + \epsilon_{y2}$ (2);
ϵ_{y1} : real laterial strain, $\epsilon_{x1} \times \nu = -\epsilon_{y1}$ (3);
ϵ_{y2} : fake strain, $\epsilon_{x2} = \epsilon_{y2}$ (4);

So, If ϵ_x, ϵ_y, ν, are known, ϵ_{x1}, ϵ_{x2}, ϵ_{y1} ϵ_{y2} can be solved using four equations above;
Example Mathematica calculation: epitaxial Silicon <110> tensile test sample;

```
εx = 7.40 * 10^-3;
εy = 9.4 * 10^-4;
ν = 0.06;
NSolve[{εx == εx1 + εx2, εy == εy1 + εy2, εx1 * ν == -εy1, εx2 == εy2}, {εx1, εx2, εy1, εy2}]
```

```
{{εx1 → 0.00609434 , εx2 → 0.00130566 , εy1 → -0.00036566 , εy2 → 0.00130566 }}
```

Figure T4- 26 and Figure T4- 27 show the uncorrected and corrected results for elastic modulus. The curve fitting slope is the elastic modulus in units of Pa. Table T4- 3 gives the results for epitaxial silicon that are used as a standard micro tensile test sample. The results match the published results for the material.

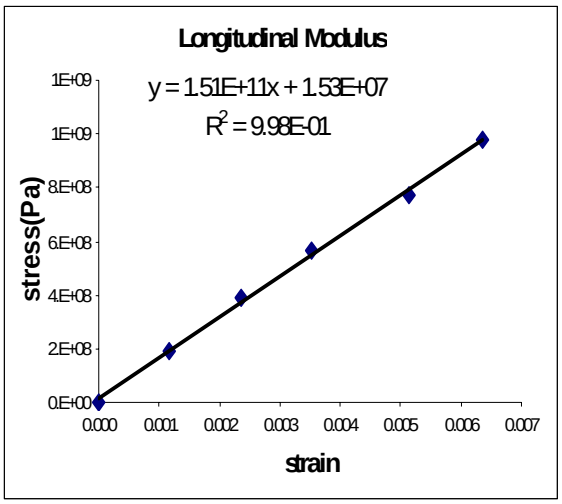

Figure T4- 26. Uncorrected results/

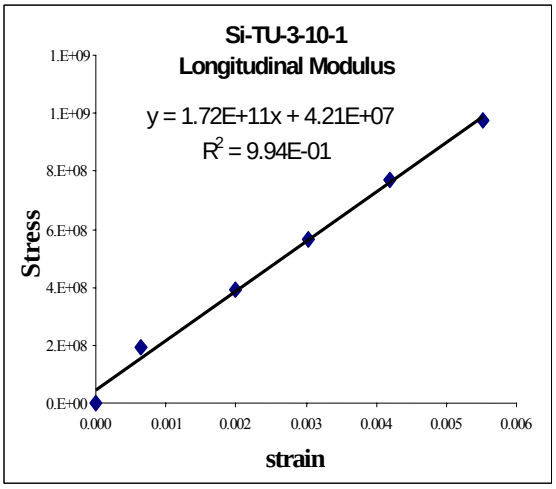

Figure T4- 27. Corrected results.

Epitaxial silicon <110>

E(Gpa) calculated by Real Strain

	Si-TU-3-8	Si-TU-3-9	Si-TU-3-10	Si-TU-3-11
test-1	166	174	172	165
test-2	~	~	169	~
test-3	~	~	168	~
Average	166	174	170	165

Epitaxial silicon <100>

E(Gpa) calculated by Real Strain

	Si-DR-1-1	Si-DR-1-2	Si-DR-1-3
test-1	128	125	122
test-2	~	133	130
test-3	~	~	131
Average	128	129	126

Table T4- 3. Measured values of elastic modulus for silicon.

Therefore, despite systematic errors in the DIC system due to defocusing, analytical corrections can be made to obtain accurate measurements of elastic modulus.

1.6 Measuring Elastic Modulus of SiCN Micro Tensile Test Specimens

Micro tensile testing and DIC analysis were performed on SiCN micro-scale samples and the error correction techniques described above were used to obtained the elastic modulus of SiCN. Because the SiCN sample exhibits warpage from pyrolysis, the defocusing degree was very large, as shown in Figure T4- 28.

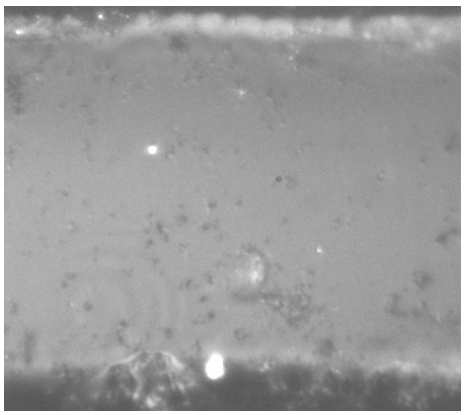

Image 1 (at loading force 0.059N)

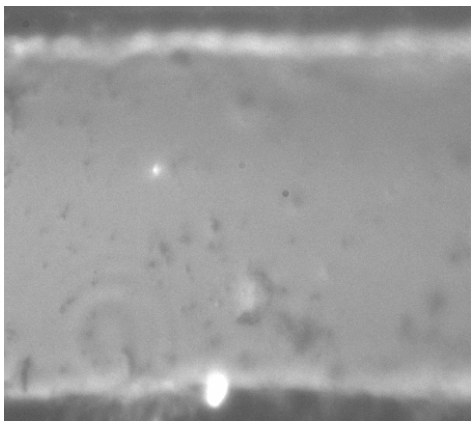

Image 2 (at loading force 0.914N)

Figure T4- 28. Defocused images taken during micro tensile test of SiCN micro sample.

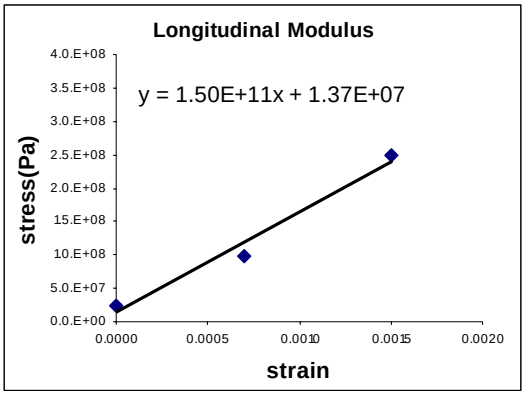

DIC result before correction

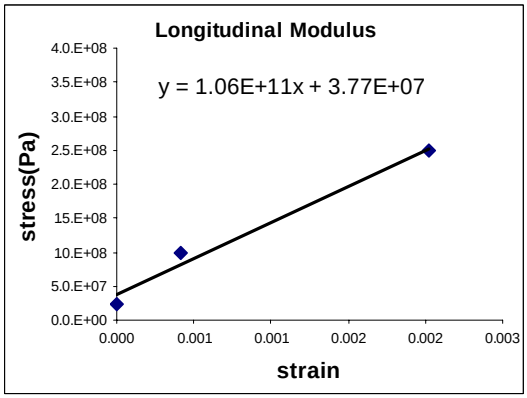

DIC result after correction

Figure T4- 29. Corrected results for elastic modulus. (curve fitting slope)

For the same SiCN sample, one result of elastic modulus obtained was 150GPa, while another result was 106 GPa. The result from indentation testing, as a reference, is 150GPa.

Figure T4- 30 is an SEM image of SiCN tensile samples fabricated using contact-photopolymerization (see Task 2). Since the samples are very thick, it is possible to polish the samples to obtain appropriate micro-scale samples with better surface conditions (flatness and pattern richness) for micro tensile testing and DIC analysis in the future.

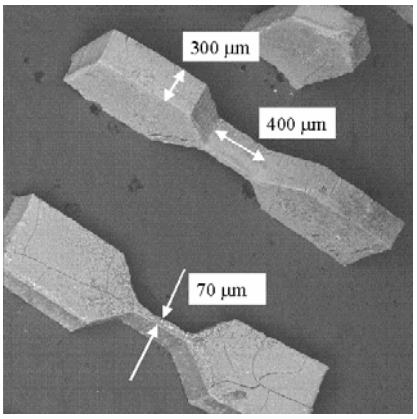

Figure T4- 30. SEM image of SiCN tensile sample fabricated using contact-photopolymerization and modified HIP processes (see Tasks 1 and 2).

2. Measurement of SiCN-SiC Composite Properties

An interesting phenomenon observed was the effect of adding particles of SiC to the precursor, thereby obtaining SiCN-SiC composites. The SiC nano powder is added to the precursor and thermosetting, crosslinking and pyrolysis are performed as usual. Different effects were observed when various amounts of SiC were added. More detail can be found in the DARPA technical report from June 2000.

A system of standardizing test samples was adopted to ensure as much consistency in size and processing as possible from one sample to another. The following is the procedure used to obtain such standard micro cast samples for micro-indentation testing:

1. The precursor contains 2-5% catalyst
2. In the case where SiC particles are added (see below), the average diameter of a SiC particle is 0.3 microns.
3. The SiC powder (if used) is introduced into the liquid precursor, and the mixture is stirred and shaken before casting.
4. Standard molds consist of holes drilled into aluminum or copper plates. Each hole has a diameter of 1500 microns and thickness of 400 microns.
5. Ceraset is used as a "glue" to attach a piece of aluminum foil to the bottom of the plate and thermal set.
6. Then, the precursor is cast into the holes and thermal set.
7. After thermal setting, the aluminum foil is peeled off, and demolding is done by punching the samples out of the holes.
8. The samples are then crosslinked and pyrolyzed.

This is shown schematically in Figure T4- 31.

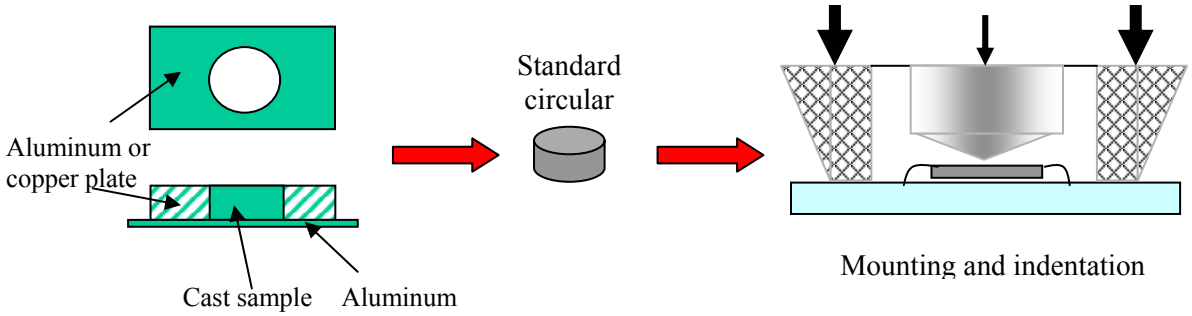

Figure T4- 31. Procedure for obtaining standard sized samples for indentation testing.

Since it is difficult to control the relative fractions of SiC and Ceraset™, it is more convenient to use a qualitative knowledge of SiC percentage to pursue the following goals in the final material:

1. evenly distributed SiC particles throughout the material
2. low shrinkage
3. high material properties
4. as few voids as possible
5. as few cracks as possible (macro and micro)
6. good surface properties

Three categories of SiCN-SiC composites were studied, depending on percentage of SiC added. Composites of low SiC percentage are those that contain 2-5% (by weight) SiC, composites of medium SiC percentage are those that contain ~10% SiC, and composites of high SiC percentage are those that contain ~20% SiC.

Composites of low SiC percentage (2-5%)

When the percentage of SiC powder is small (~2%), a steady suspension of SiC particles in liquid Ceraset™ is formed. Big particulate aggregates may also appear in the suspension. The final pyrolyzed sample may also contain scattered voids.
It was found that compared to a SiCN sample (without SiC), a small increase (~6%) in effective modulus was observed using indentation testing. Also, the shrinkage has decreased from 28% for SiCN to 26% for the composite.

Because of the effect of compliance in the epoxy used to mount the sample, the effective modulus is about 8% lower when using 1000mN loading force compared with 10mN. Thus results from using 10mN loading force are more representative of the real modulus value. Figure T4- 32 compares the measured effective modulus for various loading forces.

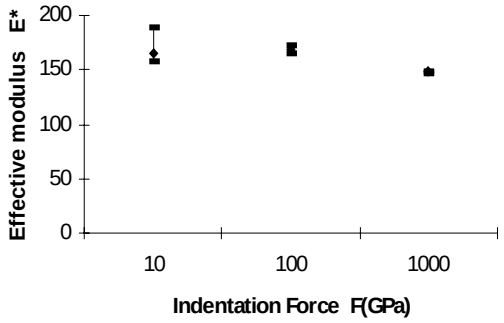

(a)

Standard SiCN+SiC(low%) sample

F(mN)	10	100	1000	Change
Ave. E*(Gpa)	165	168	148	10%
Max E*(Gpa)	189	172	149	21%
Min E*(Gpa)	157	166	147	6%

HV=15

Standard SiCN sample

F(mN)	10	100	1000	Change
E*(Gpa)	157	152	145	8%

(b)

Figure T4- 32. (a) Measured effective modulus of low percentage composite vs. loading force used during indentation. (b) Comparison of measured effective modulus of low percentage composite with pure SiCN for various loading forces.

Composites of medium percentage SiC (~10%)

When the percentage of SiC particles added exceeds 2% weight, the additional SiC particles tend to sink to the bottom of the container, forming an unstable mixture of SiC and Ceraset. By placing a mold at the bottom of the container, this sinking phenomenon can be used to obtain cast samples of a very thick mixture. However, as shown in Figure T4- 33, within the cast sample itself the SiC particles will sink to the bottom before thermal setting is completed, thus there is a shrinkage mismatch between the top and bottom of the sample, which causes large cracks on the top surface. Thus, the elastic modulus measured by the indentation test will increase towards the bottom of the sample, as shown in Figure T4- 34(a).

Indentation at different heights within the sample was done by polishing the sample gradually from the top surface before testing.

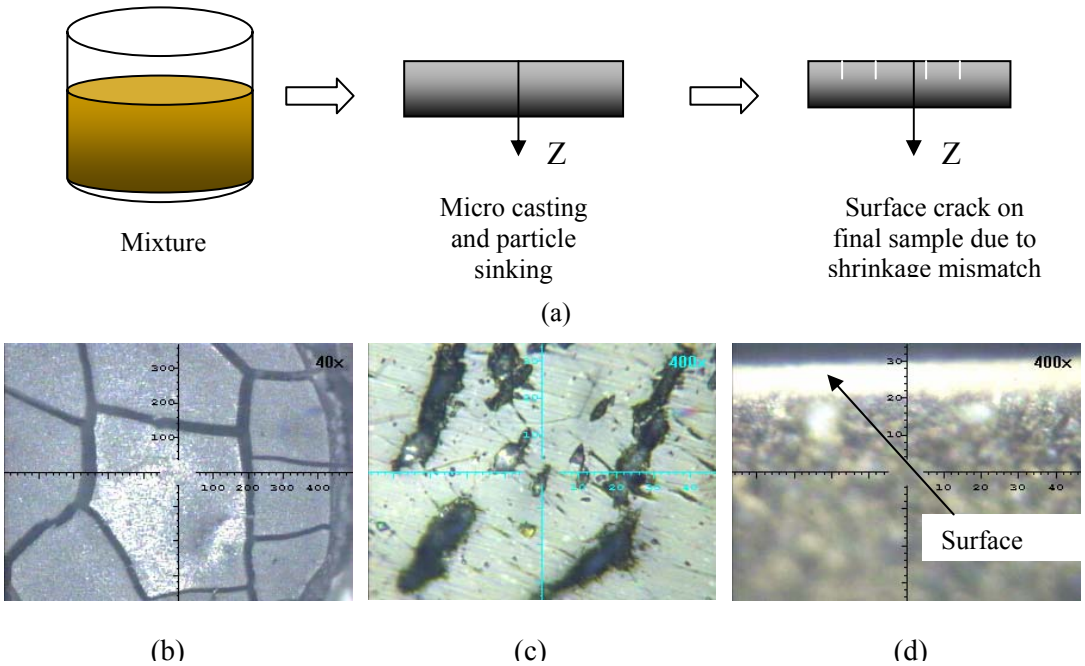

Figure T4- 33. (a) Schematic of cracking process. (b) – (d) Photographs (taken from the micro indentator) showing (b) large top surface cracks, (c) internal cracks, (d) surface layer.

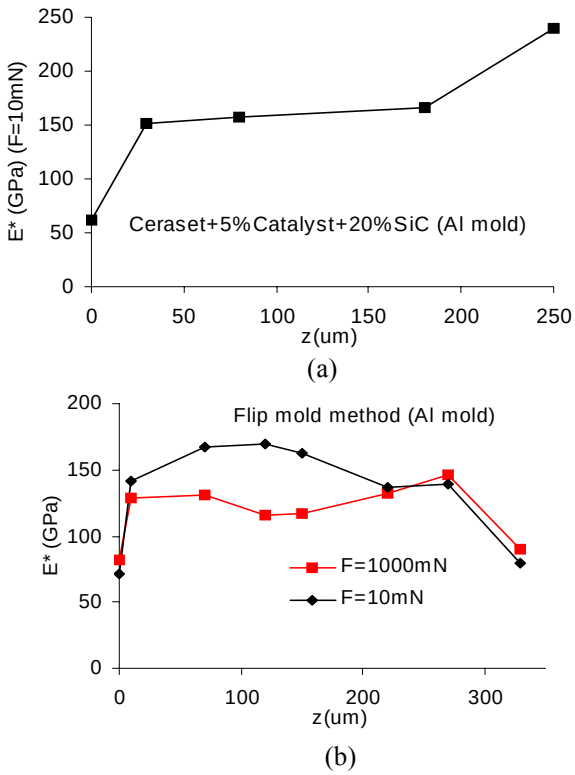

Figure T4- 34. Measured elastic modulus vs. distance from the top surface of the sample (a) sample with sunken SiC particles (b) sample prepared using the Flip Mold method.

In order to prevent the SiC particles from sinking to the bottom of the sample, the Flip Mold method is employed, in which the sealed mold is flipped upside down after 20 seconds of thermal setting to allow the sunken particles to redistribute. This results in a composite with more evenly distributed particles, and therefore more uniform properties and shrinkage. Thus the top surface cracks can be eliminated. Results are shown in Figure T4- 34(b).

It was also observed that after pyrolysis there is a brown, 8 micron-thick surface layer surrounding the sample. This surface layer is SiC, and is due to the withdrawal of Ceraset due to shrinkage, leaving behind SiC on the surrounding surface. Just below this layer, the effective modulus is relatively high (230 GPa). Several unsuccessful attempts to prevent this were tried, including polishing the surface after thermal setting and crosslinking, coating a layer of pure Ceraset in the early stages of thermal setting, and solidification of the surface layer by increasing the thermal setting temperature to 200 ^{o}C. Finally, this problem was solved by using Shear Mixing.

Since the shear strength of the particle and fluid mixture is low, applying a shear force can crush the particle aggregates so that they can mix well with the liquid Ceraset. This is commonly accomplished in industry by roller mixing. The approach adopted here was to use a knife and glass substrate to apply shear force to a portion of the mixture.

By using shear mixing, a well-mixed viscous paste is formed, which can still be micro cast. The final composite sample has evenly distributed particles and properties, and both the SiC surface layer as well as top surface cracks are avoided. However, voids and surface property degradation still exist.

A major problem with increasing the percentage of SiC particles is the formation of voids. These voids are dense and have a large volume fraction. Figure T4- 35 shows the increasing number of voids for composites with increasing percentage of SiC added.

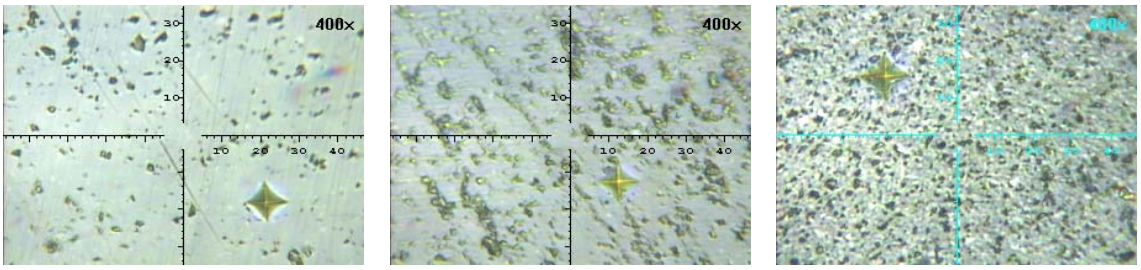

5% weight SiC 10% weight SiC 20% weight SiC

Figure T4- 35. Photographs taken under the micro indentor, showing the increasing number of voids (black dots) with increasing weight % SiC.

Void formation is due to several factors such as:

1. Shrinkage mismatch of liquid Ceraset and solid SiC particles.
2. Moisture or air bubbles trapped in the mixture.

Following is a list of unsuccessful attempts to prevent void formation:

1. Refining SiC by evaporating SiC water suspension to extract the smaller SiC particles.
2. Heating and drying the SiC to eliminate moisture before mixing.
3. Putting the sample in a vacuum drying chamber before thermal setting.
4. Applying mechanical pressure during the early stages of thermal setting.
5. Applying isostatic pressure by oil (600 psi) during thermal setting.

One reason that voids should be considered is because they give rise to the concept of local vs. global material properties. When 10mN indentation load is applied during testing, the indented area is only 1/100 of the area obtained from using 1000mN force. This means that the indent impression for 10mN may or may not be on a void. This uncertainty produces a large scatter in the effective modulus data, and is referred to as the local property of the composite. While using 1000mN force, however, the indentation is large enough to span tens of voids, so the resultant modulus is the average or global value for the composite. From Figure T4- 36(b) we see that although the maximum value for effective modulus in the composite is higher than that for SiCN, the average value is less than that for SiCN. Thus when the percentage of SiC exceeds its solubility limit in Ceraset, the dense voids have a negative effect on the nano composite structure.

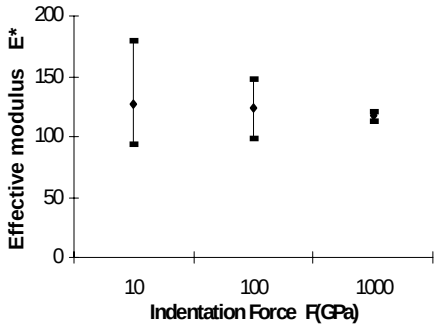

Standard SiCN+SiC sample

F(mN)	10	100	1000	Change
Ave. E*(Gpa)	127	124	118	7%
Max E*(Gpa)	179	148	120	33%
Min E*(Gpa)	94	99	113	-20%
Dev of of E*	33%	20%	3%	
Dev of hmax	13.4%	8.5%	1.5%	

Standard SiCN sample

F(mN)	10	100	1000	Change
E*(Gpa)	157	152	145	8%

Figure T4- 36. Effective modulus of medium percentage SiCN+SiC composite and SiCN.

In addition to voids, air bubbles may also be present in the final composite. These air bubbles may have been trapped in the mixture during shear mixing and retained in the final sample. Large bubbles may be up to 200 microns in diameter. Because of the expansion of the air, the height of the sample will increase instead of decreasing (by shrinking) during thermal setting. This is shown in Figure T4- 37. This has also been observed in samples placed in a vacuum chamber. This phenomenon is likely to happen with the increase in SiC percentage.

Attempts to prevent air bubble formation include curing at 100 ^{o}C to drive out the air, as well as the same techniques used to try to prevent void formation. All have not been successful. One possible solution is to do the mixing in a vacuum chamber.

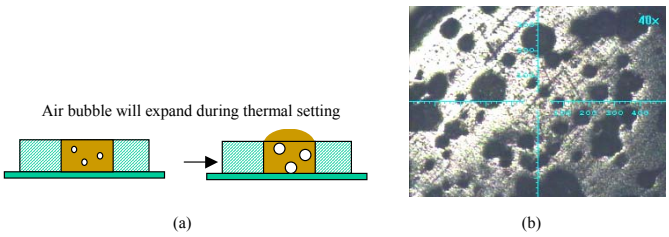

Figure T4- 37. (a) Schematic of air-bubble effect. (b) Photograph (taken under the micro indentor) of air bubbles in composite.

Composites of high percentage SiC (~20%)

It was found that the average measured effective modulus of composites with high percentage SiC is lower than that of SiCN; however, because the voids are dense and even smaller than the size of the indents caused by 10mN loading force, the scatter in the data is low. It was also observed that if SiC percentage is extremely high, no global shrinkage occurs.

Some measurements of effective modulus were taken for pure SiC powder, by indenting on the SiC aggregates. The results are:
F=10mN: E*=160GPa (SiC E=405GPa)
F=1N: E*=130GPa HV=10GPa

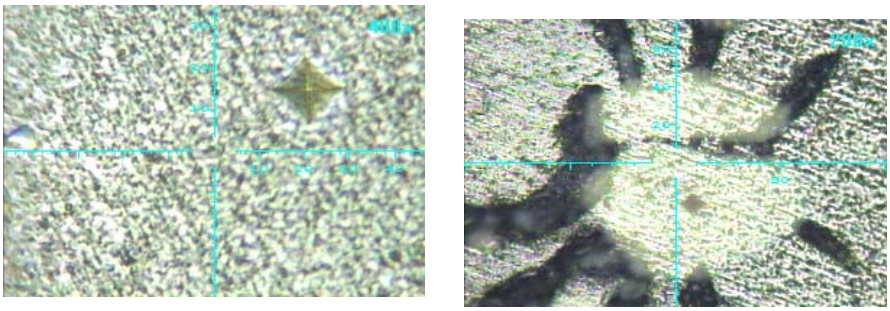

high % SiC composites Cracks around big SiC aggregates

Figure T4- 38. Photographs (taken under micro indentor) of high percentage SiC composite.

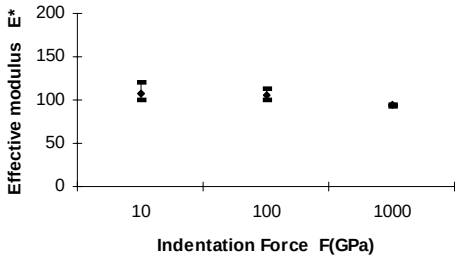

Standard SiCN+SiC(high%) sample

F(mN)	10	100	1000	Change
Ave. E*(Gpa)	107	106	94	12%
Max E*(Gpa)	121	113	95	21%
Min E*(Gpa)	100	100	93	7%

Figure T4- 39. Measured effective modulus of composite with high percentage SiC.

Nano particle composites model

Because of the conflict between the shrinking Ceraset matrix and the non-shrinking solid SiC particles, several conclusions can be drawn:

1. Adding a small percentage of SiC will result in large shrinkage and small, sparse voids.
2. Adding medium percentage of SiC will result in large voids and cracks due to the incompressibility of the contacted SiC particle cluster.
3. Adding a large percentage of SiC will result in evenly distributed small voids

These are shown schematically in Figure T4- 40. In the future sintering the ceramic after pyrolysis should be investigated as another possible solution to preventing void formation.

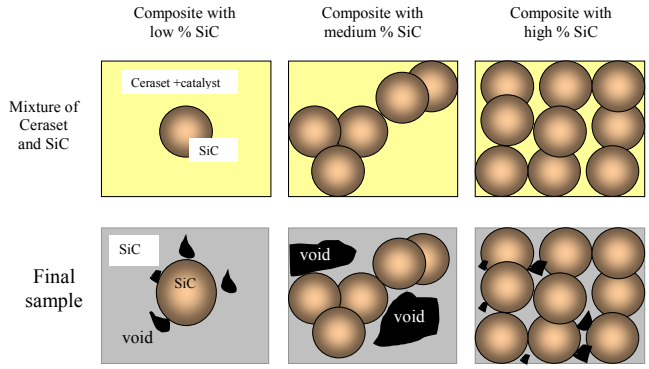

Figure T4- 40. Schematic of the effect of increasing the percentage of SiC on void formation.

3. Fabrication Issues

3.1 Dimensional Change from Pyrolysis

One of the most important characteristics of the SiCN material process that has to be considered during fabrication is the dimensional change during pyrolysis due to gas evolution and material densification. This dimensional change from pyrolysis for MEMS-scale samples has been measured at about 34% in all directions, while shrinkage from crosslinking alone is less than 1%. This section reports the methods used to obtain this result, and discusses its implications in the development of the fabrication process and also in the design of SiCN MEMS.

Figure T4- 41 is a schematic of three test structures used to measure the shrinkage from crosslinking and pyrolysis. Each test structure consisted of two squares arranged diagonally, with the side of each square being L = 200 microns long in the fabrication mask. The test structures were fabricated on an existing polymer layer by direct-photopolymerization method (see Task 2), so that the entire structure containing the test structures was allowed to shrink uniformly while maintaining their orientation for easy identification for measurements at each stage of the material process.

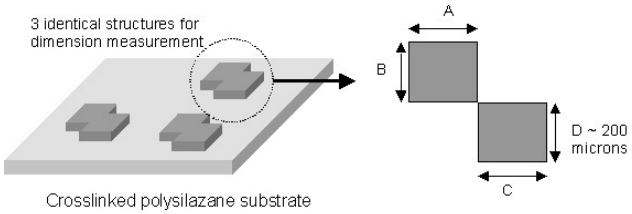

Figure T4- 41. Schematic of test structures for measuring dimensional change.

Each dimension (A,B,C,D) for each of the three test structures was measured three times using a calibrated scale under an optical microscope with a 20x magnification. This was done after photopolymerization, then after crosslinking, and then again after pyrolysis.Figure T4-42(a) shows typical results for one test structure, results for other test structures being very similar.

As seen in Figure T4-42(a), the dimensional change is roughly uniform in all directions, since each dimension (A,B,C,D) changes by similar amounts. From measuring each dimension on each test structure

three times after each stage in the process (for a total of twelve measurements of L for each stage of the heat-treatment process), average shrinkages were calculated. By averaging the shrinkages of A,B,C,D for each of the three test structures, the overall shrinkage of each test structure was calculated as shown in FigureT4-42(b). Then, by further averaging the shrinkages over all the test structures, the average shrinkage for the SiCN MEMS fabrication process was obtained. The final results show that the average linear shrinkage (relative to the size of the structure immediately after polymerization) is 1.0% after crosslinking, and 34.1% after pyrolysis. Figure T4- 42 shows the dramatic size change between a crosslinked and a pyrolyzed SiCN micro combustion chamber. The dimensional change from pyrolysis is therefore significant and has to be accounted for during MEMS design, modeling and fabrication, and packaging. For example, fabrication masks for SiCN MEMS should be scaled up in size by about one-third from the final desired specifications. This "one-third rule" has been found to work very well in the design and fabrication of SiCN MEMS. Note that if polysilazane MEMS are the desired end-result, shrinkage need not be considered since the dimensional change from crosslinking is less than 1%.

By contrast, the shrinkage of SiCN parts fabricated using the lost-mold process ranged from 15 to 20 %, which is significantly less than that for demolded, free-standing structures (see DARPA technical report from June 2000 for more detail).

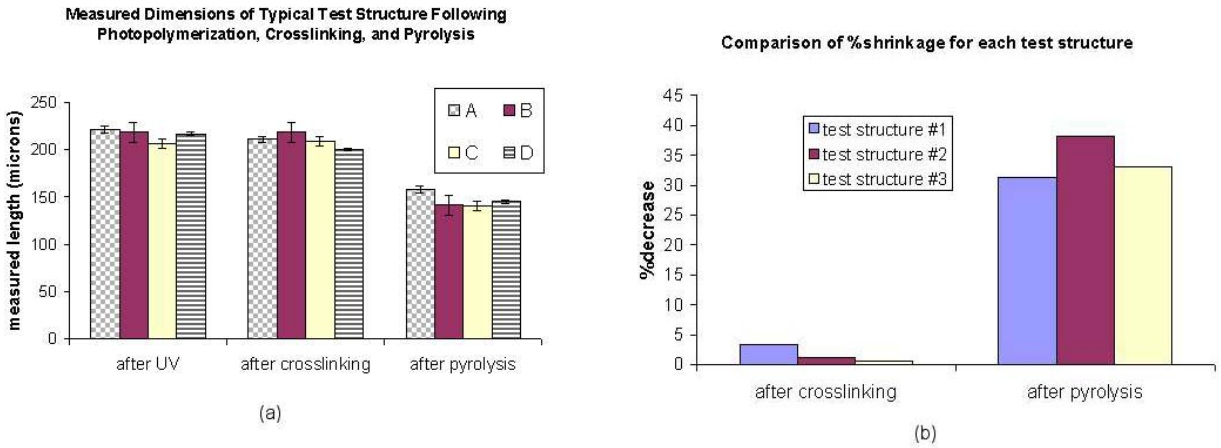

Figure T4- 42. (a) Graph showing dimensional change for one of the test structures. The error bars are the largest standard deviations for each dimension represented over the course of the entire experiment. (b) Percent shrinkage for each test structure from crosslinking and pyrolysis.

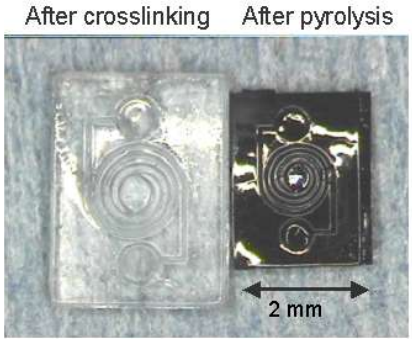

Figure T4- 42. Photograph of a crosslinked combustion chamber (left) beside a pyrolyzed combustion chamber (right), showing the reduction in size in pyrolyzed samples. The pyrolyzed combustion chamber measures 3 mm x 2 mm.

3.2 Warping

Another issue in SiCN MEMS fabrication is warping of SiCN structures following pyrolysis. This phenomenon has been observed in some MEMS-processed SiCN, but has not been quantified.

The reason for warping is not fully understood at present. It could be attributed to several factors or combinations of factors, such as uneven photopolymerization (since UV light originates from the top of the layer to be polymerized), polymer absorption of rinsing solution following the polymerization step, or uneven gas diffusion during pyrolysis. It was found that the warping could be almost completely eliminated by polymerizing the underside of the structures (after it had been removed from the silicon substrate) with a piece of transparent glass on top acting as a weight, or by placing a weight on top of the structure during pyrolysis. High-purity graphite blocks are used for this purpose because their porosity enables gas diffusion out of the material as it evolves into SiCN. Also, application of pressure during pyrolysis seemed to help, but is believed to result in trapping of gaseous byproducts within the final material thus leading to increased porosity as well as different chemical composition. Pyrolyzed SiCN pieces that are annealed without physical constraint will also become warped, thus suggesting that uneven gas diffusion is likely the cause.

In general, warping is undesirable because it leads to difficulties in packaging and coupling of SiCN components. Hence, to avoid warping the polymer structures are sandwiched in between graphite blocks (with graphite foil as an intermediate layer) during pyrolysis and annealing. Resultant structures are extremely flat, exhibiting a surface height variation of 1-2 microns over a surface area of 200 microns x 200 microns (and thickness 30 microns), as measured under a laser interferometric microscope for ten structures.

Despite the desirability of flat components, this interesting phenomenon may be advantageous in certain applications where pre-stressed MEMS structures could be used, such as micro turbine blades for use in micro power generation systems.

3.3 Whisker Formation from Annealing

As reported in Tasks 1 and 2, annealing of the SiCN following pyrolysis lowers the electrical conductivity, which is advantages for MEMS applications especially at room temperature. However, one problem encountered during annealing is that of oxidation on the surface of the annealed devices. Following annealing, the samples are covered with a white film. On MEMS devices this film is usually

very thin, appearing like strands of cobweb which are not bonded to the SiCN structures but instead surround them, making it difficult to remove without breaking the devices. Although compositional testing of the white film has not been done, we think that it is oxidation due to trapped oxygen within the SiCN structures. Figure T4- 43 shows SEMS of the annealed thermal actuators surrounded by the white oxidation. The application of pressure during pyrolysis in the HIP could have trapped oxygen within the SiCN, thereby leading to oxidation during annealing.

Also, before annealing the SiCN structures are a shiny and smooth black, whereas after annealing they were a duller color. Examination under SEM revealed that the surface of the annealed SiCN was considerably rougher than that of the as-pyrolyzed structures. Figure T4- 44 shows the increase in surface roughness and the oxidation. But there was no noticeable loss in mechanical strength, at least not from handling the structures.

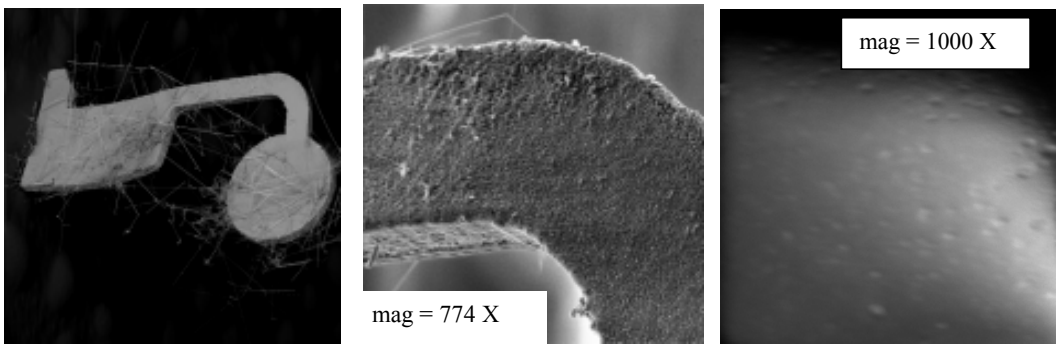

Figure T4- 43. (a) Annealed sample, showing the oxidation which is the surrounding cobweb-like strands.

(b) Closeup of the same structure (magnification = 774X), showing the rough surface following annealing. (c) Surface of as-pyrolyzed sample from the same experiment, at a magnification of 1000X, showing that the as-pyrolyzed sample's outer surface is indeed much smoother than that of the annealed samples. Each pore in this picture was measured under SEM to be about 1-5 microns in diameter.

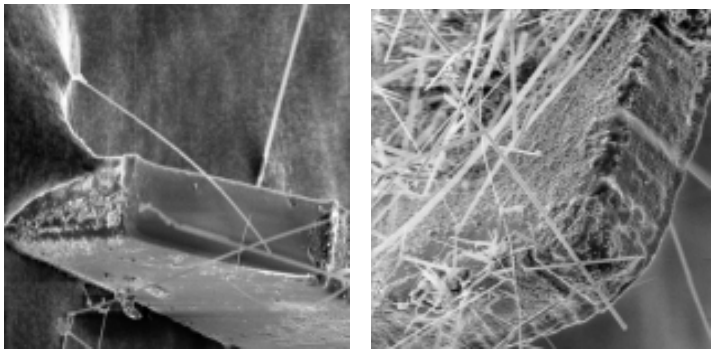

Figure T4- 44 (a): Broken surface of the thermal actuator, showing its cross-section (70 microns thick).

This picture shows that the inner surface of the SiCN is still smooth like after pyrolysis, only the outer surface is roughened from annealing. (b): Magnification = 1000X. Outer surface of the annealed thermal actuator, the grass-like structures are the oxidation.

While these whiskers cannot, to our knowledge, be chemically removed, they are not bonded to the structure and as such can be physically removed by gentle brushing with a fine-tipped paintbrush.

Despite this, whisker-formation should be minimized if possible because of the risk that their removal poses to SiCN structures that are small or delicate. For example, the gap separating the arms of a lateral thermal actuator, when fabricated in SiCN, could contain these whiskers. Physical removal of the whiskers places the device's delicate "hot-arm" at risk of being broken. Furthermore, if the whiskers are left on the structure they may interfere with the device movement or functioning.

Task 5: High-Temperature Devices

A variety of SiCN MEMS devices have been successfully designed, fabricated and demonstrated. These devices provide tangible evidence that the primary objective of this project has been fulfilled.

The MEMS devices that have been implemented can be divided into two categories: (1) "traditional" MEMS devices that were originally implemented in silicon technology, (2) devices which are unique to this project, not being realizable by other MEMS technologies.

The purpose of the first category of devices is to show that existing MEMS design knowledge can be leveraged in SiCN MEMS technology, i.e. devices that have been made from silicon can also be made from SiCN. Examples are the vertical piston electrostatic actuator and the lateral thermal actuator. The second category consists of a new class of devices: micro ultrahigh-temperature heaters that are shown to heat up to 1500 ^{o}C continuously for over 24 hours. This category also includes a high-temperature polymer transmission grating made from the SiCN precursor.

Two designs were singled out for more in-depth analysis and characterization, the purpose being to use these MEMS devices to obtain fundamental properties of SiCN.

Content:

1. Vertical Piston Electrostatic Actuator
2. Micro Glow Plug
3. Pressure Transducer Membrane
4. High-Temperature Polymer Transmission Grating
5. Lateral Thermal Actuator and Microgripper
6. Magnetic Sensor/Actuator
7. Thermopneumatic Array
8. Caps for MEMS Device-Level Packaging
9. Micro Combustion Chamber

1. Vertical Piston Electrostatic Actuator

The design of this device follows that of a typical parallel-plate electrostatic actuator. In this case, the top movable plate is SiCN, while the ground electrode is gold on alumina substrate. The SiCN part is fabricated independently of the substrate. The substrate, which is obtained commercially, is patterned to produce the desired gold traces and wiring. Indium solder (3 microns thick) is selectively deposited on the substrate bond pads using evaporation and lift-off techniques. Then, the SiCN part is attached to the substrate by flip-chip bonding technique so that the SiCN movable plate is suspended 3 microns above the ground electrode. Details of the fabrication and assembly of the electrostatic actuator can be found in our DARPA technical report from September 2000.

Two generations of designs were implemented, as shown in Figure T5- 1 and Figure T5- 2. The 1st generation design consists of a square plate supported symmetrically by four flexures, while the 2nd generation design consists of a circular plate suspended by three flexures which are attached to a frame, the frame being bonded to the substrate on three sides.

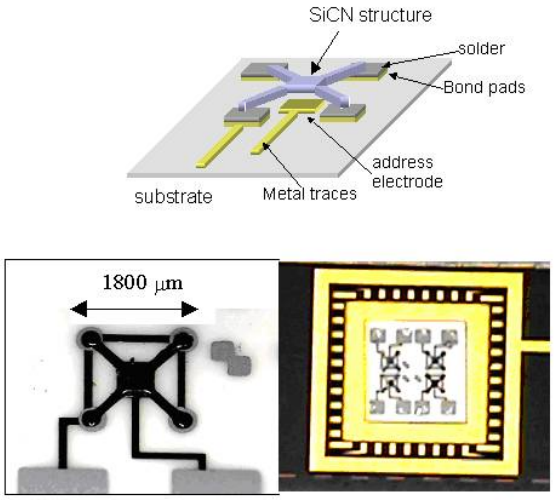

Figure T5- 1. Schematic and photograph of the 1st generation electrostatic actuator, and a packaged array of four actuators.

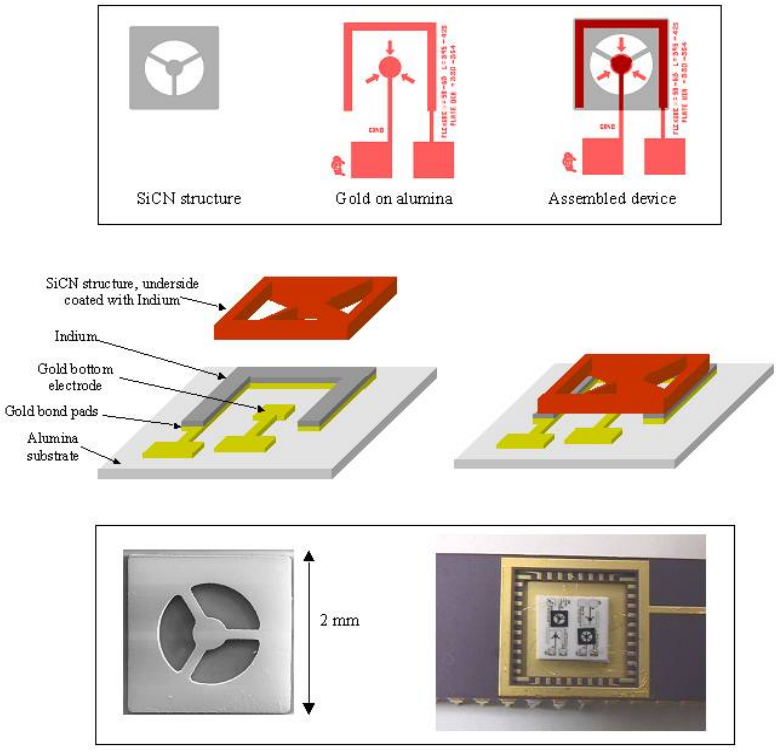

Figure T5- 2. 2nd-generation SiCN electrostatic actuator.

Top: CAD layouts of the masks for the SiCN component and the receiving substrate. Middle: schematic of the device configuration. (Note: the ground electrode is depicted as being square, while in the actual device it is circular.) Bottom: SEM of the SiCN component, and photograph of a packaged array of two devices.

Modeling and Testing Results for the 2nd generation actuator

Various levels of DC voltage were applied to the device, and the deflection was measured using a Zygo laser interferometric microscope. Five to ten measurements were taken for each input voltage.

The data for this device was used as a starting point to find Youngs Modulus, E, of SiCN. First a simple analytic model was used to describe the actuator's voltage-deflection behavior. The analytical model is based on equating the applied electrostatic force from the voltage (treating the device as a parallel plate capacitor) with the mechanical restoring force in the device's flexures, which are treated as simple cantilever beams with an end load (see DARPA report Sept 2001).

The data was then replotted as V^2 vs. deflection, resulting in a straight line. The slope of this line, which is $V^2/(z_o\text{-}d)$ where z_o is the initial air gap between the ground electrode and the SiCN, was then put into the analytical equation and the terms in the equation were rearranged to solve for E. The value of E obtained in this way was 150 GPa.

This value is only a starting value, however, due to the simplifying assumptions used in applying the equations. These simplifying assumptions are: (1) the flexures can be treated as simple cantilever beams, when in reality they are not rigidly fixed at one end because they are instead fixed to a frame and which is also suspended. Any deflection or deformation in the frame would allow the supposedly fixed end of the flexure to move as well. (2) The SiCN plate is assumed to stay parallel to the ground electrode during deflection. However, because the frame is bonded only along three edges, the fourth edge could deflect, causing an increase in deflection for the flexure on that side of the frame and leading to an overall tilting of the circular plate. (3) By using the parallel plate-equation we are assuming that the charge distribution on the top and bottom electrodes are equal an opposite. However, in reality the bottom electrode is larger in area than the SiCN plate. (4) As seen in Figure T5- 2, the ground line runs under a portion of the frame, and this could cause actuation of the frame itself.

The effects of these factors were investigated using the Coventorware™ finite element package from Coventor, and were found to influence the modeled deflection and hence the estimation of Youngs Modulus. By making the FE model as accurate as possible by accounting for the larger ground electrode area, the ground line running under the frame, and the presence of the Indium layer on the SiCN, the FEM is able to capture the non-idealities in the device that the analytical model cannot account for. Figure T5-3 shows the modeled deflection of the SiCN device from 300 volts, the deflection has been exaggerated 300 times in the figure in order that the deformation of the plate can be more clearly seen.

The deflection of the center of the plate was measured during experiment, and is compared with that in the FEM. The value of Youngs Modulus was varied in the FEM and the resulting deflection compared with that of the experiment. The value of Youngs Modulus that causes the finite element model to correspond most closely to the experimental deflection values is 140-155 GPa. The analytical and FE model is compared with the experimental data, as shown in Figure T5- 4.

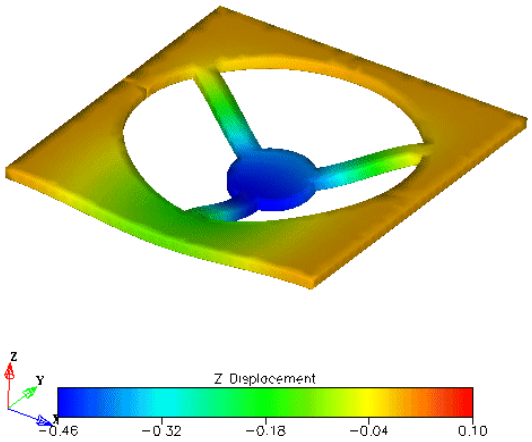

Figure T5- 3. Finite element model of deflected SiCN actuator at 300 volts, deflection is exaggerated 300 times. Legend is in microns.

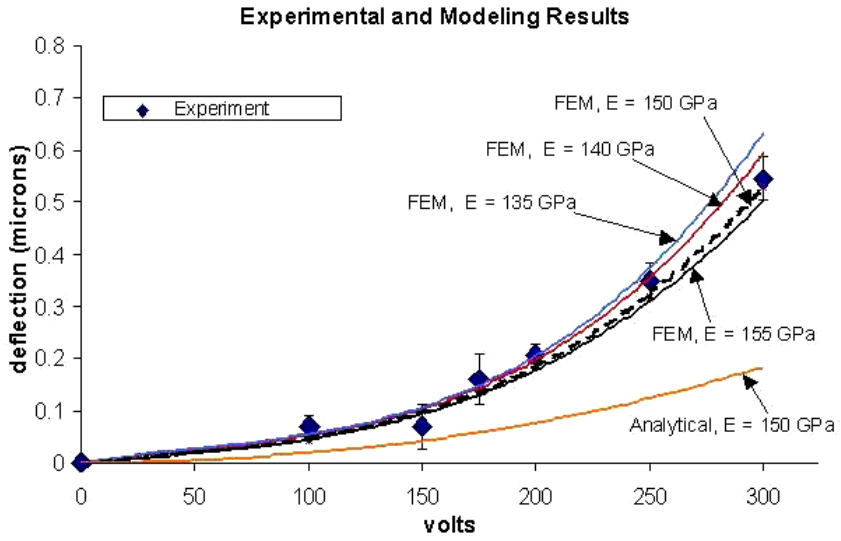

Figure T5- 4. Experimental, analytical and finite element results for the 2nd generation electrostatic actuator.

The experimental curve is based on data for two devices, the error bars being the standard deviation for 10 measurements.

Modeling and Testing Results for the 1st generation actuator

The design of the 2nd generation actuator was based on the need for increased mechanical robustness in the SiCN structure (compared to the 1st generation design) to withstand manual assembly and flip-chip bonding.

However, one limitation with the 2nd-generation actuator was its asymmetry, which led to deviation from ideal parallel-plate behavior. This resulted in significant differences between finite element and analytical

models as shown in Figure T5- 4. Thus, due to the design of the actuator – which was to increase robustness for packaging yield – analytical models were limited in use and FEM was instead heavily relied on.
We therefore returned to the 1st-generation design due to its inherent symmetry. When combined with refined fabrication and packaging techniques, fabrication yield significantly improved to where five devices were successfully tested for actuation. Furthermore, due to increased planarity of the fabricated structures, laser interferometry produced more consistent results with higher precision and less scatter compared to the early devices of both designs.

Figure T5- 5 shows a typical set of data for one of these new devices. Each data point on the plot represents an average of ten measurements, and the error bars represent the standard deviation.

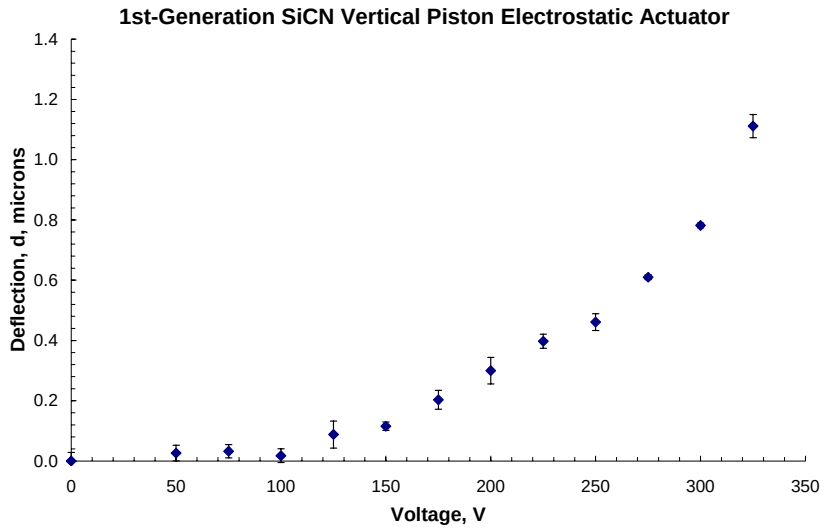

Figure T5- 5. Typical characteristics of a 1st-generation SiCN vertical piston electrostatic actuator.

Figure T5- 6 shows the results for this particular device when re-plotted as V^2 vs. $d(z_o-d)^2$, where V is the voltage, d is the deflection, and z_o is the initial separation between the actuator movable plate and the bottom electrode, which from theory should be a linear relationship. The high linearity of the data in this plot confirms the reliability of the data obtained. The Young's Modulus obtained from fitting the analytical model to the data is E = 145 GPa, which is in good agreement with results obtained from tensile testing, and which also agrees with the results obtained from the 2nd-generation actuator via FE modeling.

More detail on the 2nd- and 1st-generation actuator has been reported in the DARPA technical reports from September 2001 and June 2002, respectively.

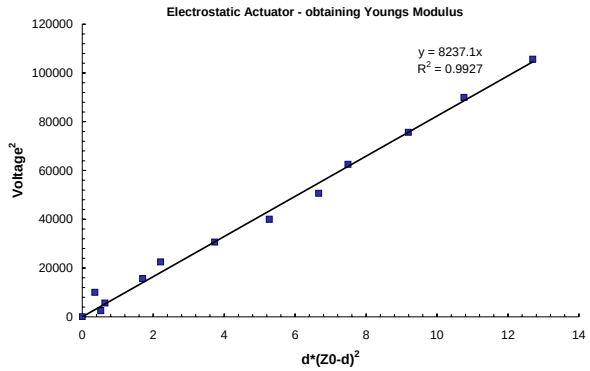

Figure T5- 6. 1st-generation actuator data after linearization, for extraction of Young's Modulus.

2. Micro Glow Plug

This project has led to the development of a new class of Microsystems: micro ultrahigh-temperature (> 1000 ^{o}C) heaters. This concept is exemplified by a device which we call the Micro Glow Plug, a device for which a nonprovisional U.S. patent application has been filed.

The Micro Glow Plug was conceived as a result of our investigations in Task 1 and Task 2, specifically, the combination of electrical properties with integrated micromachining/synthesis for SiCN. The multifunctional nature of SiCN being such that its electrical conductivity can be tailored, the Micro Glow Plug is simply a resistive heater that is designed to provide a hot spot of up to 1500 ^{o}C. Devices have been actuated continuously (generating temperatures over 1200 ^{o}C) in air for over 24 hours in d.c. mode. To our, knowledge, in the current MEMS literature there are virtually no MEMS resistive heaters which can heat to this high of a temperature continuously in an oxidizing environment. Similarly, glow plugs which do heat to these temperatures in oxidizing environments, are not as economical in design and manufacture as MEMS.

Glow plugs are temperature ignition devices commonly employed in diesel and natural gas engines. Several drawbacks are associated with these large-scale devices: Three different materials and manufacturing processes are required to fabricate the glow tip thus driving up device cost. This is because the filament which typically is made from a metal needs to be protected from oxidation by encasing material and sheath, while thermal management such as for the electrical contacts is also needed. The device is large due to the manufacturing processes used yet the entire heating element heats up to the maximum temperature (1200 ^{o}C), leading to high power consumption (20-100 Watts), slow response (5-10 seconds) and the need for additional materials for thermal management of the electrical contacts. Figure T5- **7** shows a schematic and photographs of conventional glow plugs.

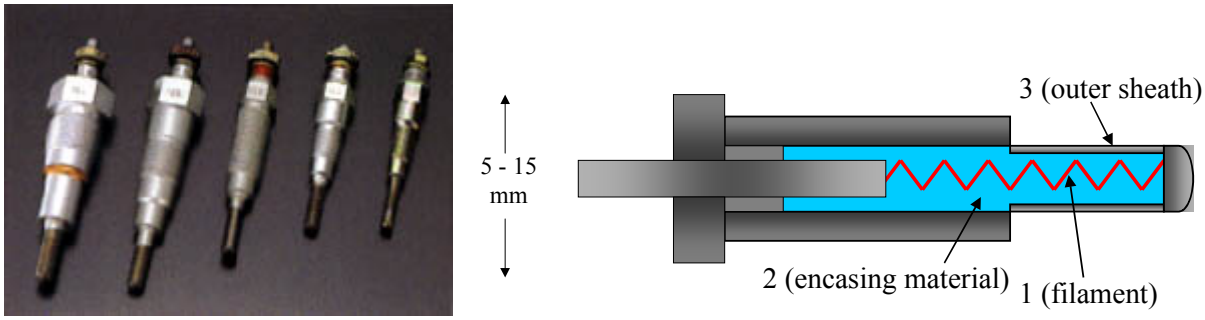

Figure T5- 7. Left: Photograph of conventional diesel glow plugs, typical length 30-50 mm.

Photos courtesy of Robert Bosh Corp. (http://www.bosch.com) Right: Schematic of the major components of a glow plug.

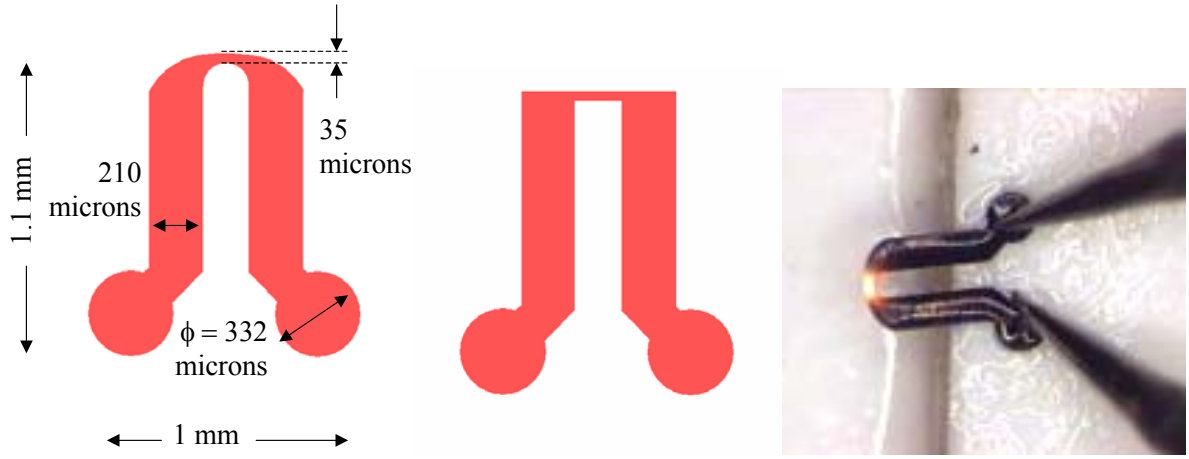

Figure T5- 8. (a) Schematic of a "U"-shaped glow plug. (b) Schematic of a "Pi"-shaped glow plug. (c) Photograph of a U-shaped device glowing from 50 mA applied current.

Temperature ignition in diesel engines is but one example of an existing application involving harsh environments that could benefit from the reduced size, response time and power consumption offered by microsystems but which so far has remained unfulfilled due to material limitations. Until now no MEMS technology existed that could miniaturize a diesel glow plug because of the extremely high ignition-temperatures that need to be achieved. Furthermore, the device would be subjected to chemically corrosive environments and high thermal shock. These requirements alone immediately make material selection the prime factor that eliminates most of the existing MEMS technologies. Even within the broad class of materials known as ceramics such a combination of high-temperature corrosion resistance, thermal shock resistance, creep resistance, electrical conductivity, micromachineability and low manufacturing cost is uncommon. Figure T5- 8 shows the design and photograph of one Micro Glow Plug (MGP) developed through this project.

Thus, the SiCN Micro Glow Plug is a device which we believe has the potential to penetrate new markets previously untouched by MEMS.

	Conventional Glow Plugs	SiCN Micro Glow Plug
Size	Length 30-50 mm	Length 1.1 mm
Temperature	1200 ^{o}C	1200 ^{o}C
Power Requirement	20-100 Watts	3 Watts
Response Time	5-10 seconds	0.5 seconds
Fabrication Complexity	3 materials 3 process	1 material 1 process

Table T5- 1. Comparison between conventional glow plugs and SiCN Micro Glow Plug.

Modeling and Characterization of Device Performance:

Referring to Figure T5- 8, the glow tip of the device is referred to as the "web" and the flexures on either side of the web are the "cold arms".

The devices were characterized according to the following: (1) web temperature vs. current, (2) electrical conductivity vs. temperature, (3) device lifetime vs. current, (4) resistance change vs. time. Figure T5- 9 shows the experimental setup used for device characterization.

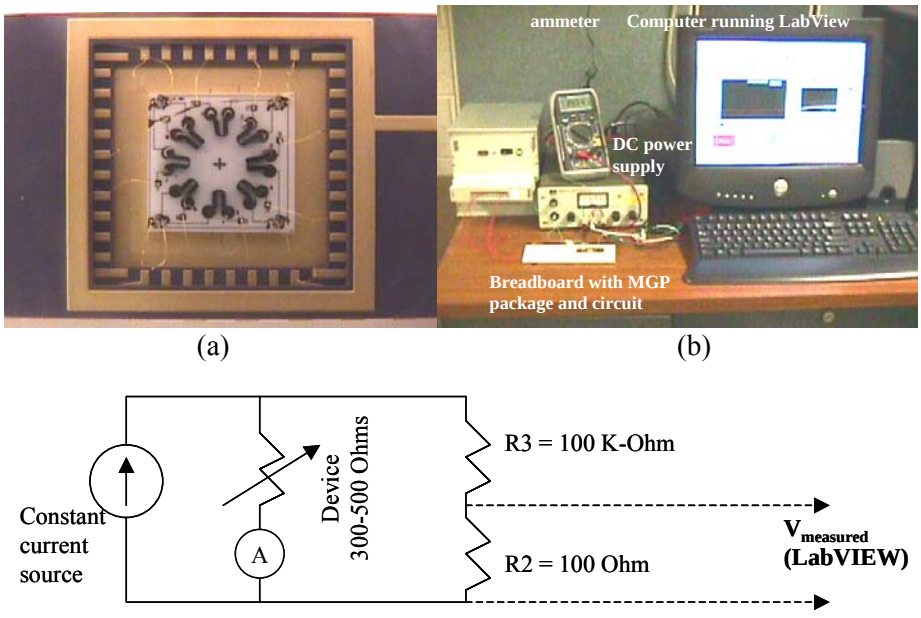

Figure T5- 9. (a) Photograph of an array of packaged Micro Glow Plugs. (b) Experimental system used for MGP characterization. (c) Schematic of the circuit used in the experimental system.

The experimental setup consists of a constant-current source, voltage-divider circuit (designed so as to maintain constant current within the device to within 1% variation), ammeter, and a computer running the LabView data acquisition software. Each MGP within an array was tested one at a time. A LabView

program was written to calculate and record the MGP resistance (in a 2-probe configuration) in real-time, as a lumped circuit element.

Figure T5- 10 and Figure T5- 11 show typical data collected for the MGPs. For these experiments, only "pi"-shaped devices were used due to the simpler web geometry that makes for easier analytical modeling. Also, all devices used had been fabricated in the same fabrication run to minimize as much as possible variations in SiCN thickness and process history. As seen in these figures, there are two distinct temperature regimes in which the measurements and property behavior were stable as expected. These two regimes are separated by a transition region, which corresponded experimentally to the first appearance of visible red glow within the web. Experimentally, measurements taken within this region were unstable, hence the relatively fewer number of data points. Figure T5- 11 shows the resistance of the SiCN actually increasing with temperature within this transition region, which is contrary to its expected semiconductive behavior that is displayed within the two stable regimes. It is unclear what the cause of the transition region is – we believe it to be related to changes within the structure of the material, the onset of increased radiation heat loss, or effects of contact resistance. In the analysis, these two regimes are treated separately.

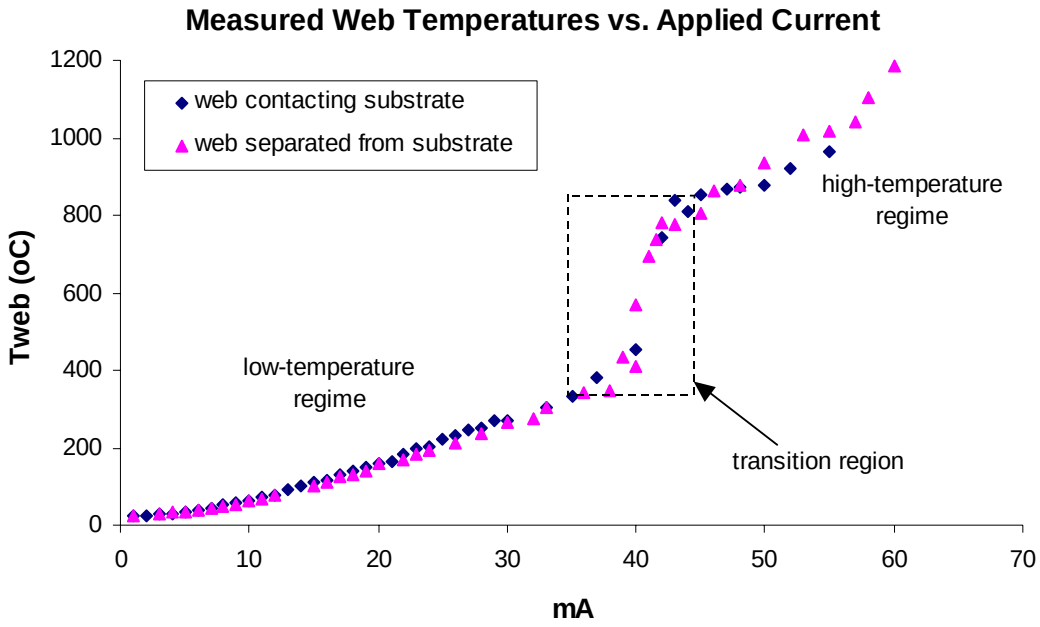

Figure T5- 10. Measured steady-state web temperature vs. operating current in two devices. Temperature was measured using a Type K thermocouple of diameter 1 mil.

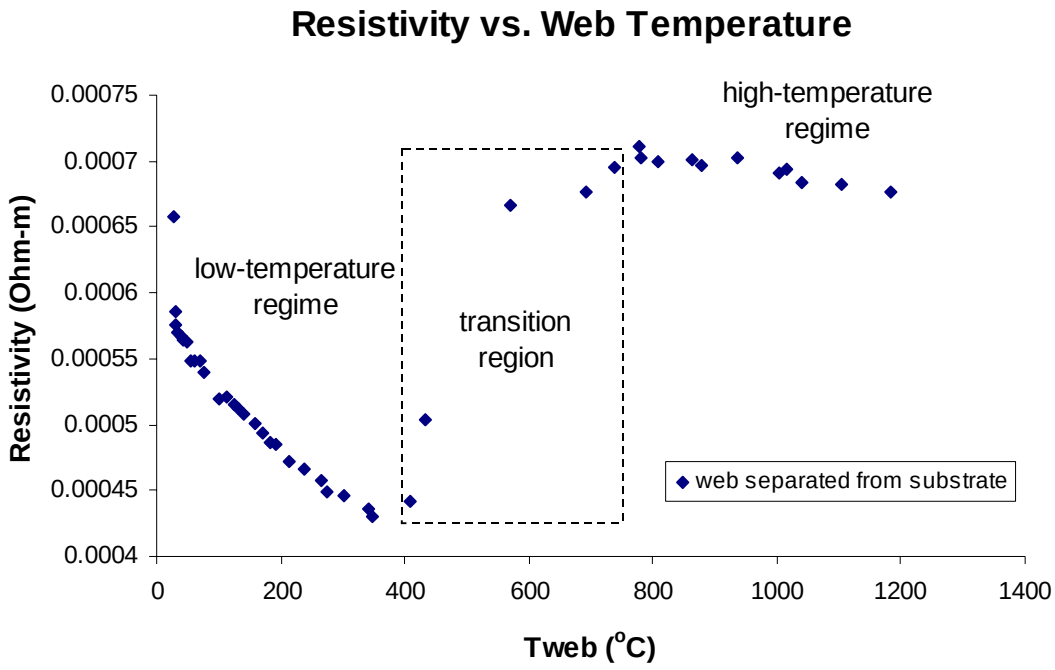

Figure T5- 11. Measured resistivity vs. web temperature for one MGP.

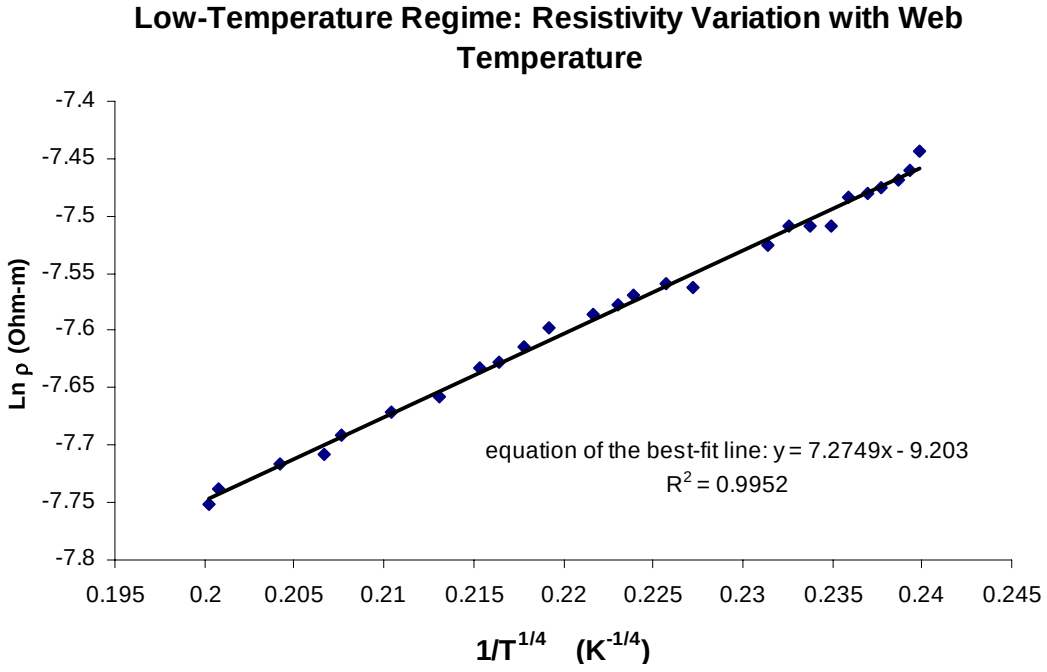

Figure T5- 12. Temperature-dependence of resistivity for MGP, showing the presence of the Mott Variable Range Hopping conduction mechanism.

Figure T5- 12 shows the resistance-temperature results for the low-temperature regime, plotted as a function of $T^{-1/4}$. The high linearity of the data indicates that the conduction mechanism within the SiCN follows Mott's 3D Variable Range Hopping behavior, which is characteristic of amorphous

semiconductors and which was also observed by Herman et al (see Task 1) for non-MEMS processed SiCN and SiBCN. According to the VRH model, the temperature-dependence of resistivity is given by:

$$\rho = \rho o \exp^{(\frac{\xi}{T})^{1/4}}$$

where the Mott-temperature ξ and the pre-exponential ρ_o are material-specific constants, and T is the temperature. By extrapolating the data in Figure T5- 12 as well as that for the high-temperature regime, ξ and ρ_o were found to be the following:

	Low-temperature regime	High-temperature regime
ξ	1.8×10^3 K	5.08×10^2 K
ρ_o	0.0002 Ω–m	0.0009 Ω-m

Table T5- 2. Mott VRH parameters for the low- and high-temperature regimes, found from MGP.

The temperature-dependence of the MEMS-processed SiCN resistivity has therefore been found in-situ. We expect that these values should differ from that of SiCN processed through the non-MEMS route due to difference in material composition as confirmed by material characterization via FTIR and x-ray diffraction.

A lumped analytical electro-thermal model was constructed to verify the Mott parameters obtained. The model consists of a simple heat-transfer analysis, whereby the heat losses from the web considered are conduction to the cold arms, conduction to the underlying substrate, natural convection, and radiation. The heat-generation in the model utilizes the Mott VRH parameters from Table T5- 2. As seen in Figure T5- **13**, the analytical model agrees well with the data especially in the low-temperature regime. The disparity between model and data in the high-temperature regime is attributed to difficulties in temperature measurement due to the thermocouple softening and eventually melting at such high temperatures. Temperature measurement using non-contact methods (such as with a pyrometer of infrared camera) have proved difficult due to the small spot size of the web that needs to be focused.

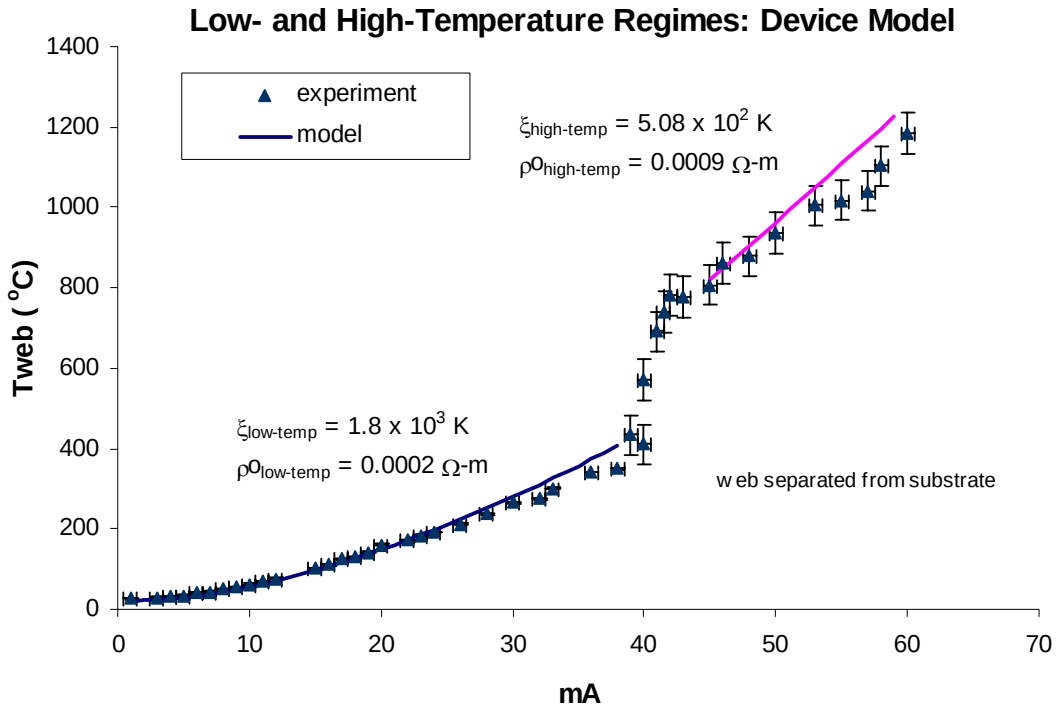

Figure T5- 13. Analytical model compared with experimental results.

Devices were also operated to failure under constant d.c. current. Figure T5- 14 shows the lifetimes of MGPs within one array. As expected, the higher the applied current, the sooner the devices fail. The lifetime is related to the rate at which the SiCN oxidizes at the high web temperatures generated, the temperature in turn being related to the operating current. Figure T5- 15 shows the typical lifetime chart for one device as it is operated at constant current until failure. The device resistance increases with time since the oxide layer growth decreases the useable web cross-section for current conduction. "Failure" occurs when the resistance has increased to where the finite power supply (120 V, 100 mA) is unable to continue supplying current through the device. Figure T5- 16(a) shows the oxide layer on a failed device. However, the suddenness of the point of failure suggests that other failure mechanisms are involved, such as cracking due to excessive gas evolution from the material at high-temperatures, as evidenced by the large cracks shown in Figure T5- 16(b). However, oxidation dominates the lifetime behavior – i.e. resistance change – over most of the lifetime.

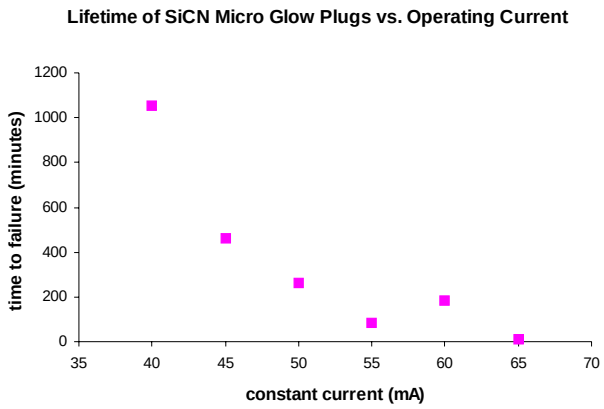

Figure T5- 14. Device lifetime vs. operating current.

Measured lifetimes have so far ranged from a few minutes to 18 hours of continuous operation at temperatures high enough to achieve visible glow.

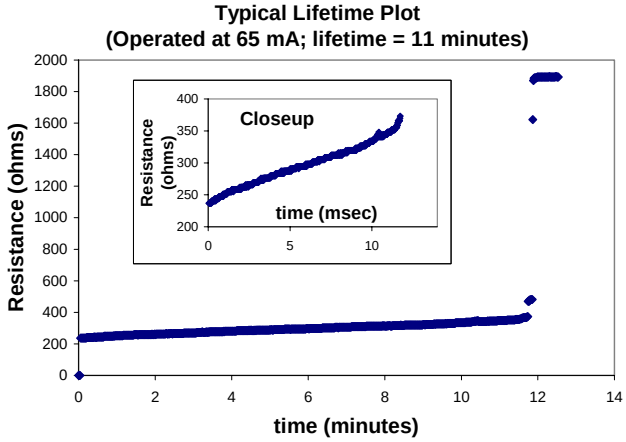

Figure T5- 15. A typical lifetime graph for one device.

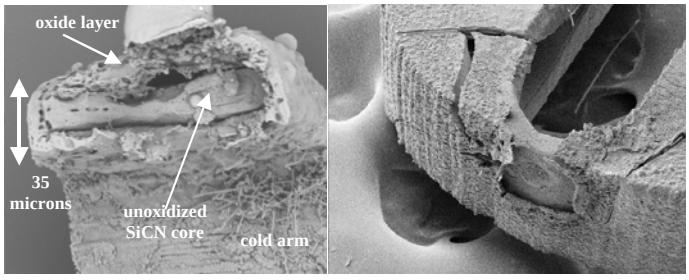

(a) (b)

Figure T5- 16. SEMs of MGPs after failure.(a) Cross-section of the web, showing oxidation layer. (b) Outer surface of the web and cold arms, showing macroscopic cracks that also contribute to failure.

By measuring the oxide layer thickness under SEM and obtaining the operating temperature via the electro-thermal model and VRH data, the oxidation activation energy for the SiCN can be obtained from the Deal-Grove model [B.E. Deal and A.S. Grove, *J. Applied Physics*, vol. 36, no. 12, pp. 3770-3778, 1965]:

$$\omega^2 = \tau\alpha e^{\frac{-Q}{RT}}$$

where ω is the oxide thickness, τ is time, α is the pre-exponential for oxidation, Q is the activation energy for oxidation, T is the temperature, and R is the universal gas constant. An Arrhenius plot of the MGP data is shown in Figure T5- 17. From this plot Q and α are found to be: Q = 81-88 kJ/mol, $\alpha = 3.2 \times 10^{-11}$ to 1.5×10^{-10} m^2/s. More detail on the modeling and characterization can be found in our DARPA technical report from June 2002.

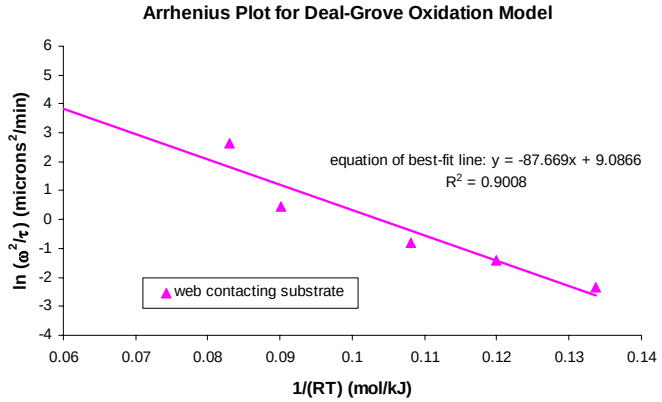

Figure T5- 17. Arrhenius plot for MGP oxidation behavior.

SiCN Micro Glow Plug as an Ultrahigh Temperature Igniter

In addition to the device characterization described in the previous section, the MGPs were also used successfully as high-temperature igniters, being used to ignite thermite [A. C. Davies, The Science and Practice of Welding, 8th ed. Cambridge University Press, New York, 1984.]. Thermite is a solid-state explosive that has an ignition temperature of about 1200 °C. Due to this high ignition temperature, thermite is commonly ignited with a strip of burning magnesium ribbon or other vigorous reactions. The thermite reaction itself is highly exothermic, producing temperatures above 2000 °C. Uses of thermite include welding (known as the Goldschmidt process) and in military incendiary weapons.

In this experiment, thermite was made by mixing Fe_2O_3 with Al powder in a 3:1 ratio. When the temperature of the mixture is raised to above 1200 °C (the ignition temperature), an oxidation-reduction reaction occurs resulting in molten iron:

$$2Al(s) + Fe_2O_3 \rightarrow Al_2O_3(l) + 2Fe(l)$$

In each experiment, a single MGP was used to ignite 5 grams of thermite. This is 25,000 times the mass of the MGP itself. Wires were soldered to the pins on the ceramic package, and the package was placed within a beaker (both glass and plastic beakers were used) and buried in the thermite. Due to the self-propagating nature of the thermite reaction, a single MGP operating at 25 mA was able to fully ignite all of the thermite, completely engulfing the ceramic package in molten iron. There was no trace of the MGP or the ceramic package following this reaction. Figure T5- 18 is a video still showing the extent of the

reaction within a 30-mL glass beaker initiated by a single MGP. (Not shown are subsequent video stills in which the glass beaker and then the alumina plate on which it was placed shattered from the extreme thermal shock.)

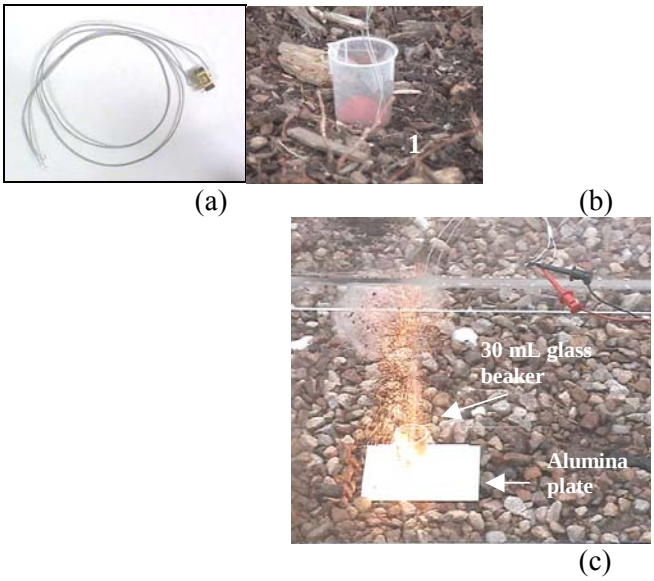

(a) (b)

(c)

Figure T5- 18. Photographs of Micro Glow Plug igniting thermite. (a) Photograph of a single packaged device. (b) Photograph of the package immersed in a 30 mL plastic beaker. (c) Photograph of a reaction within a glass beaker.

We have therefore proven that the MGP can indeed function as a ultrahigh-temperature MEMS-scale igniter. Furthermore, this experiment also points to the future possibility of harnessing the power of thermite reactions on the micro scale, such as to produce very powerful micro-thrusters.

Resistive heaters that operate on the same principle were designed and fabricated.
Figure T5- **19** shows one such heater "melting" a piece of Pyrex glass, the glass-transition temperature of the glass being around 850 ^{o}C.

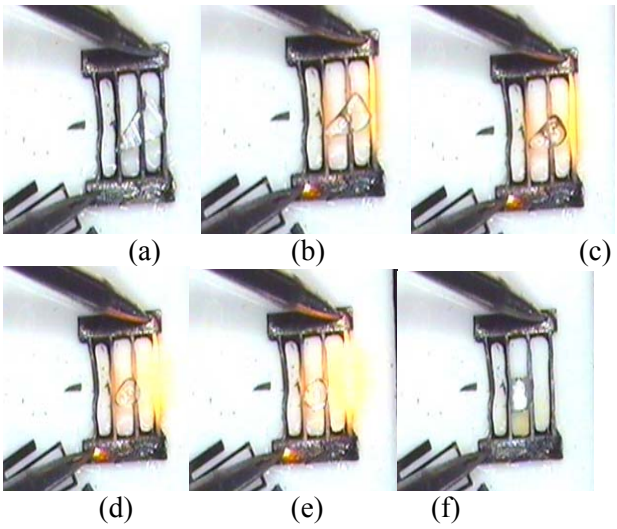

Figure T5- 19. SiCN resistive heater melting a piece of glass.

The electrical contact pads are 1.6 mm long, 330 microns wide. The widths of the heating lines are, from left to right, 50 mcirons, 40, microns, 30 microns, 20 microns, and all are about 2 mm long. The entire device is about 200 microns thick. This entire sequence took about 2 seconds.

3. Pressure Sensor Membrane

Figure T5- 20 shows a schematic and the fabrication approach of a SiCN pressure sensor membrane. It is a double-layered SiCN structure, consisting of a membrane with a support layer underneath. This structure may then be mounted onto a substrate, and, if the appropriate metallization is done, the membrane deflection in response to applied pressure may be measured capacitively. The final membrane thickness was 35 microns, diameter was 800 microns, and the total length of the support structure was 2 mm.

Once fabricated, the pressure transducer membrane was flipped upside down and the frame was attached to a silicon wafer using non-conductive epoxy. While this does not create a hermetically sealed environment under the membrane, the purpose of this bonding was simply to attach the SiCN structure to a surface so that mechanical point loads could be applied to the membrane. For actual pressure sensing applications, hermetic sealing of the interface between the SiCN frame and silicon wafer would be necessary to create a reference pressure under the membrane. In addition, since only the physical structure of the pressure sensor has been fabricated, metallization and packaging techniques would need to be developed in order to obtain electrical signals.

A micro-indentation machine was used to simulate transducer loading. This instrument accurately measures the position of a small probe (10 microns in diameter) while the load is varied. Figure T5- 21 shows the result of deflection testing for one of the transducer units. The probe was placed in the center of the membrane. The data closely matches the modeled response, the load-deflection curve being largely linear until local stress close to the probe tip caused fracture near the tip. The value of Young's Modulus used in the model was 150 GPa, as measured using indentation techniques. The analytical deflection was obtained by modeling the membrane as a circular plate with clamped edges and an applied point load. More details can be found in our DARPA technical report from June 2000.

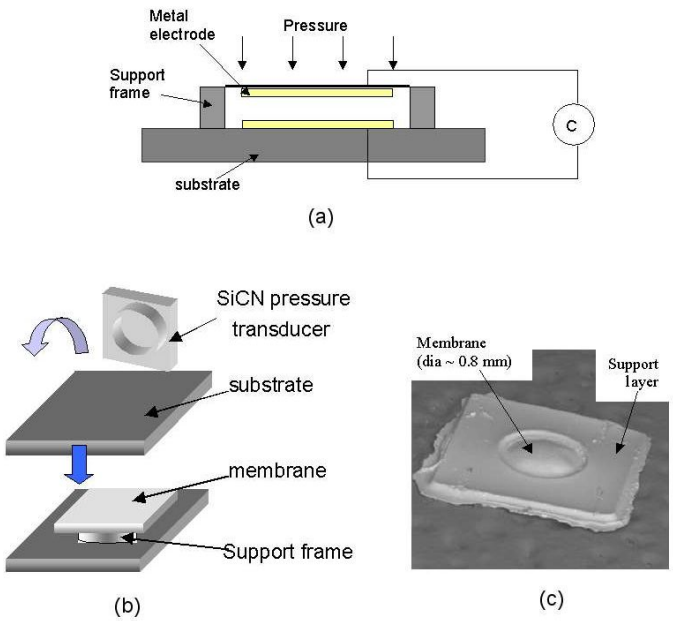

Figure T5- 20. (a) principle of operation of pressure sensor. (b) schematic of fabrication approach. (c) SEM of pressure transducer without substrate, upside down. The membrane is about 35 microns thick.

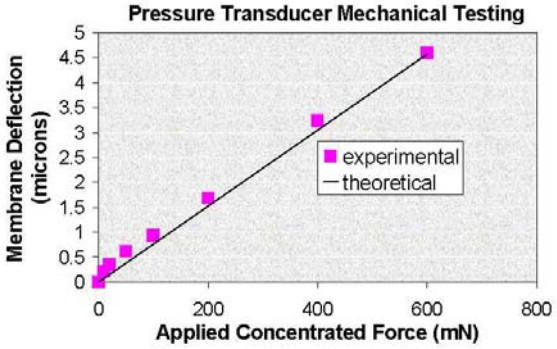

Figure T5- 21. Results of analytical modeling and mechanical testing of pressure transducer membrane.

4. High-Temperature Polymer Transmission Grating

The SiCN polymer-precursor, Ceraset^{TM}, is by itself a unique material, being a poly-urea-methyl-vinyl-silazane which is a new class of hybrid organic/inorganic polymeric glass. Polysilazane exhibits the following favorable properties: it is highly transparent in the infrared to ultraviolet range, the UV absorption being closer to that of silicate glasses than to other polymeric glasses such as polycarbonate and PMMA. Furthermore, it has been shown to remain thermally stable at temperatures up to 230 ^{o}C without losing optical transparency, whereas the aforementioned polymers exhibit decrease in transparency or material degradation at such temperatures. Add to that our low-cost polymer-forming techniques – microcasting and photopolymerization – and we have demonstrated that we can leverage the technology originally developed for creating SiCN MEMS, to also create polymeric optical MEMS.

We have chosen to demonstrate this concept in the form of a simple transmission grating made from Ceraset™. Gratings were fabricated by Microcasting in Teflon-coated SU8™ molds (see Task 2). Details are found in the DARPA technical report from September 2001.

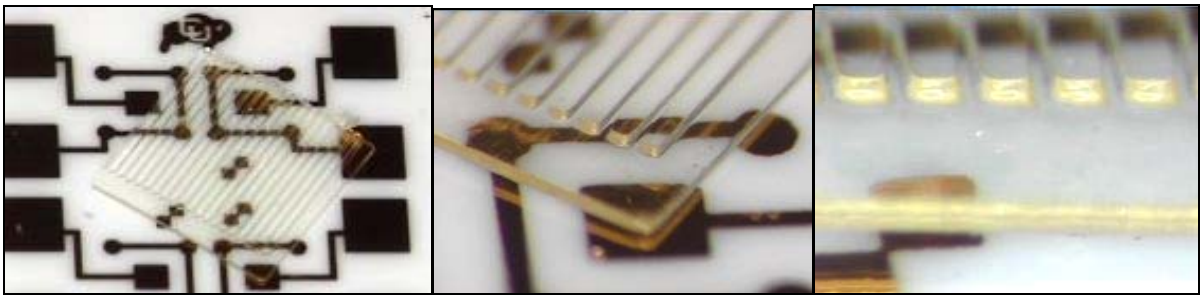

(a) (b) (c)

Figure T5- 22. Photographs of polysilazane transmission grating, placed on a piece of alumina with arbitrary gold patterns.

Entire grating is 3mm x 3m. (b) and (c) show closeups of the grating grooves.

Figure T5- 22 shows photographs of the fabricated gratings. The width of each grating element is 100 microns, and the gap between elements is 50 microns (thus the pitch is 150 microns). The height of the elements (or groove depth) is 40 microns, and the thickness of the base plate is 75 microns. Compared to gratings made commercially or by other technologies, this grating is very coarse, the line dimensions being one or two orders of magnitude greater. Much finer features are possible with carefully controlled cleanroom processing and the use of higher resolution photomasks. In this case, since only a demonstration device was intended without a specific application, feature sizes were increased for ease of fabrication. Furthermore, because polishing was not performed in this case, the surfaces of the grating are not as smooth as that of glass gratings, although in the future polishing could be added to decrease surface roughness as well as to planarize the surfaces.

To demonstrate their high-temperature effectiveness, the gratings were placed in an oven at 250 ^{o}C for several minutes prior to testing. PMMA and polycarbonate material samples that were placed in the same oven partially melted or degraded. The gratings were then tested in the setup shown in Figure T5- 23, using a He-Ne laser (wavelength 632 nm). The resulting diffraction pattern is shown in Figure T5- 24.

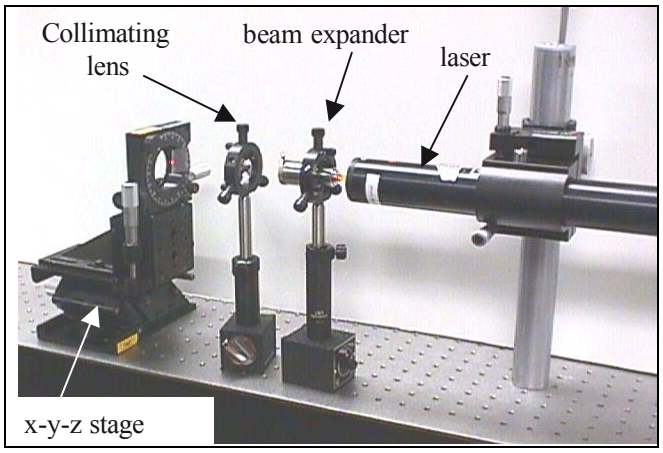

Figure T5- 23. Experimental setup.

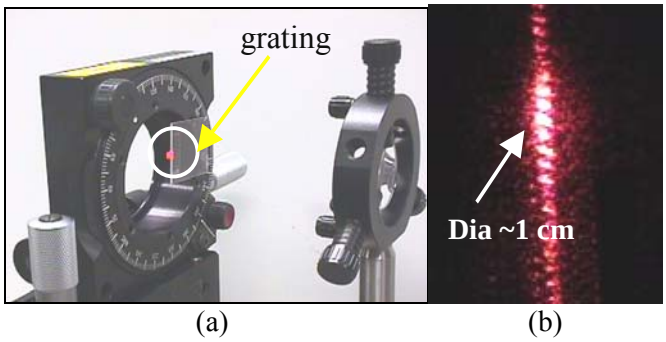

Figure T5- 24 (a) shows the closeup of the mounted grating. The laser spot is focused on the grating. (b) Resulting diffraction pattern.

Because the ratio of wavelength to grating pitch $\lambda/P << 1$, we expect to see a high number of diffraction orders, as in Figure T5- 24(b). The distance from the m=0 to m=+/- 1 order is about 1.2 cm, for a screen placed 10 feet from the grating. A power meter was used to measure the intensity of each diffracted order. The relative efficiency of the grating for each order was computed by taking the ratio of the intensity of each order to the intensity of the beam passing straight through the material non-diffracted. The results are shown in Figure T5- 25.

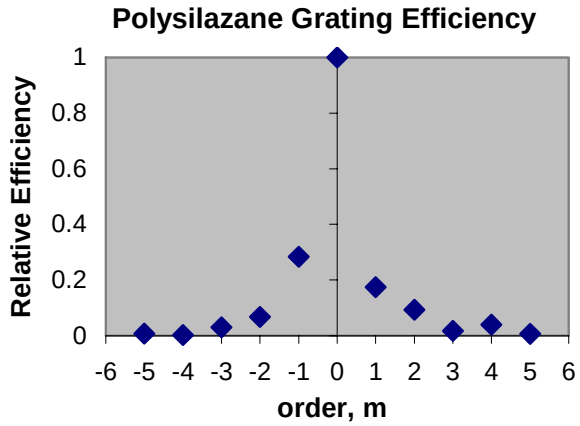

Figure T5- 25. Relative efficiency for each diffracted order, for wavelength of 632 nm.

Grating efficiency can be improved by use of higher resolution photomasks and refined cleanroom processing to reduce line widths, by polishing the grating surfaces to achieve smoother and more planar surfaces, and by controlling the incident beam angle more carefully to obtain more accurate efficiency measurements.

Since the incident beam was normal to the back plane of the grating (i.e. incident angle = 0), the grating equation simplifies to:

$$P \sin \lambda_m = m\lambda \qquad (4)$$

where P is the pitch of the grating (in this 150 microns), m is the order of diffraction, and λ is the wavelength of the incident beam. Thus the expected angle of the first diffracted order (m = 1) was calculated from Equation 4 to be 0.24 ^{o} from the normal. By measuring the distance between the m=0 and m=1 spot (1.2 cm), and measuring the distance between the screen and the grating (10 feet), the experimental diffraction angle was computed to be 0.21 ^{o}, which is in good agreement with the predicted angle.

We have thus demonstrated a low-cost micromachined phase transmission grating made out of polysilazane that is operational following heating in 250 ^{o}C environment.

5. Lateral Thermal Actuator and Microgripper

Figure T5- **26** shows a SiCN thermal actuator. The actuator and the microgrippers shown in this section were made by microcasting (although contact-photopolymerization would also give the required geometrical definition not previously possible with non-contact photopolymerization). Following demolding, the devices were pyrolyzed and annealed in the HIP in a combined cycle. The cycle consisted of:
Filling the chamber with N2 to a pressure of 200 PSI.
Heating to 1000 ^{o}C at a rate of 10 ^{o}C/minute.
Holding at 1000 ^{o}C for 4 hours (the pressure has increased to 425 PSI)
Heating to 1400 ^{o}C in 1 hour
Holding at 1400 ^{o}C for 5 hours
Cooling to room temperature at a rate of 10 ^{o}C/minute.

The devices were then attached to pieces of alumina substrates using epoxy, and placed under a probe station for testing. Electrical probes were placed on the actuators' bond pads and a d.c. current was applied. It was found that at 30 mA applied current the actuators deflected about 18 microns, and at the same time noticeable glowing occurred in the hot arm. The time taken for the glowing to occur was about 1 second. Due to the lower thermal expansion coefficient of SiCN as compared with polysilicon, the SiCN actuator deflects much less relative to its size; nevertheless, we expect that this actuator would outperform silicon or metal devices in high temperature or corrosive environments.

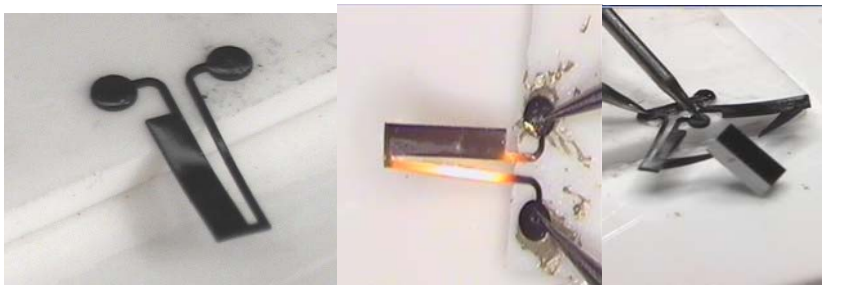

(a) (b) (c)

Figure T5- 26. (a) Photograph of SiCN thermal actuator, length 2.2 mm, thickness 85 microns. (b)Thermal actuator glowing from 30 mA applied current. (c) Microgripper mounted on alumina substrate, supporting a 1 mm x 2 mm x 0.5 mm thick silicon chip.

A micro-gripper was designed by combining two thermal actuators connected in parallel, as shown in Figure T5- **26**(c). The actuators, which are of the same dimension as those shown in Figure T5- **26**(a), share bond pads and thus move at the same time from the same applied current. The gripper's bond pads were attached to the edge of a piece of alumina using epoxy, so that the gripper itself was suspended over the edge. Figure T5- 27 shows the gripper tilting the polysilazane diffraction grating (see previous section) so that the lateral component of the grating's motion was about 50 microns. Compared with surface-micromachined grippers, the SiCN grippers are capable of supporting larger masses, given our capability for high aspect-ratio fabrication. Furthermore, the low thermal conductivity of SiCN would ensure that such grippers would not heat up the object it manipulates as much as grippers made from bulk-etched silicon, or metal devices made from the LIGA process. The chemical inertness of SiCN also makes the acutators more suitable than silicon or LIGA-fabricated devices for operation in harsh environments.

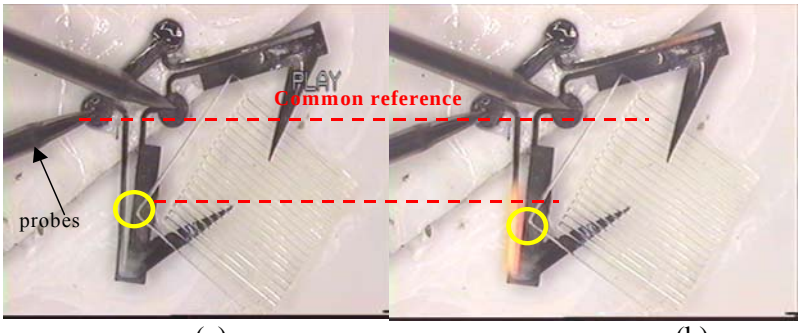

(a) (b)

Figure T5- 27. SiCN microgripper moving a polymer diffraction grating.(a) before actuationg. (b): During actuation, the position of the grating's corner has moved approximately 50 microns.

6. Magnetic Sensor/Actuator

We have exploited the multifunctional nature of polymer-derived ceramics by tailoring the electrical conductivity for MEMS applications, as evidenced by the Micro Glow Plug and Lateral Thermal Actuator.

Another way to obtain multifunctional properties is to form composites with SiCN. This can be easily accomplished because of the polymer-nature of the starting material. For example, a simple magnetic sensor/actuator was made by synthesizing Fe_3O_4 (magnetite)-SiCN composites. 30 wt% Fe_3O_4 nanopowders (diameter 100 nm, from Reade Advanced Materials, Inc.) was added to the Ceraset™ precursor which also contained 5 wt% DMPA photoinitiator, and the mixture was placed in an ultrasound bath for up to an hour immediately before micromachining in order to disperse the particles and prevent agglomerates from forming.

MEMS structures were then made by direct-photopolymerization method. For this high weight percentage of magnetic particles, the polymerized structures responded to the magnetic field of a magnetic stirring rod. Following pyrolysis in the HIP the SiCN was crack-free, and exhibited stronger attraction to the bar magnet compared to the previous polymer state. Figure T5- 28 shows a fabricated Fe_3O_4-SiCN device being deflected in the bar magnets magnetic field. The device is in the shape of the Micro Glow Plug although the material was not annealed and the device was not tested as such. Following pyrolysis, the ceramic devices were simply placed on a piece of cardboard over the bar magnet. The work done toward this avenue was only qualitative, thus the magnetic particles were not aligned, nor was the bar magnet's magnetic field measured or the deflection measured. No material characterization was performed either.

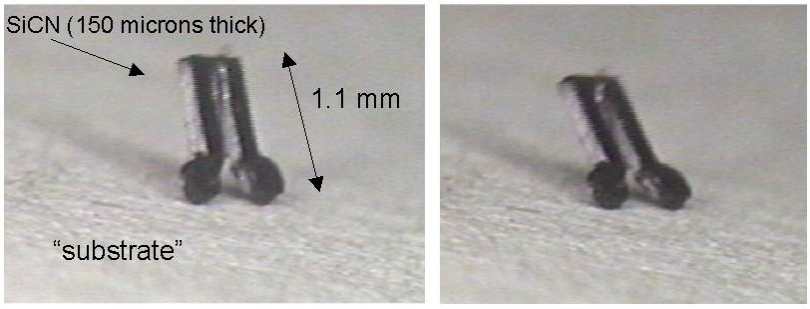

Figure T5- 28. A MEMS structure (in the shape of the Micro Glow Plug) fabricated from Fe_3O_4 -SiCN composite, shown here when it is deflected back and forth by an external magnetic field.

7. MEMS Thermopneumatic Tactile Feedback Display Device

(courtesy of Prof Y.C. Lee and Mr. Erwin Hoo, Dept. of Mechanical Engineering, University of Colorado at Boulder)

(The following is paraphrased from E. Hoo, "Initial Investigation of a MEMS Thermopneumatic Tactile Feedback Display Device," *Independent Study, University of Colorado, Dept. of Mechanical Engineering,* May 2002.)

The focus of this project was to design, fabricate and implement a MEMS-based tactile array that can ultimately be used to aid the seeing-impaired. The investigators (Prof. Lee and Mr. Hoo) had determined that this device should take the following form:

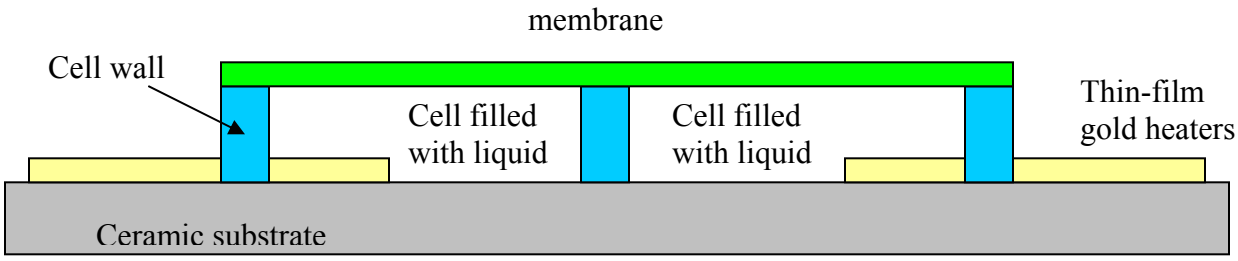

Figure T5- 29. Schematic of the cross section of a tactile array. Ceraset™ was used as the cell wall.

The principle of operation consists of fabricating arrays of "cells" on a substrate, covered with a flexible membrane. The cells are filled with a low-boiling point liquid. Current passing through the thin-film gold heaters on the substrate would heat up the liquid, forming a bubble which would deflect the membrane by an amount detectable by a human finger. When many cells are actuated, an effect similar to Braille can be created.

The personnel of this DARPA SiCN project had aided the graduate student researcher in the Tactile-Device project in designing and developing a prototype centered around the use of Ceraset™ for fabricating the cell walls, an integral part of the design. The commercial thick epoxy photoresist, SU-8™, had been the original choice due to its recent widespread use in the MEMS academic community for fabricating fluidic channels. However, it was found that Ceraset™, when used with the Contact-Photopolymerization technique developed through this project (see DARPA report June 2001), provided superior results – i.e. microfluidic channels with higher-aspect ratio, fabricated with fewer processing steps and with more planar surfaces for membrane bonding. Furthermore, the high optical transparency of the polysilazane opens new avenues for testing involving visual detection, although this was not performed. Testing showed that the prototype was able to generate bubbles within the cells (the working fluid was Fluorinert, FC-72, the membrane was latex.) shows a single-layered cell structure, while Figure T5- 31 shows a double-layered cell (see Task 3). There was no observable delamination of the layers during device testing, nor was there any chemical corrosion of the cell layers. Ceraset™, along with the photopolymerization fabrication technique developed through this DARPA project, therefore appears to be highly applicable in the presently "hot" area of microfluidics research. This effort was first reported in our DARPA technical report from June 2002.

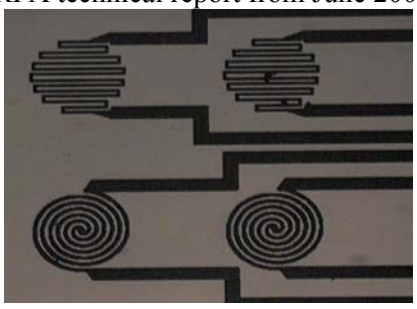

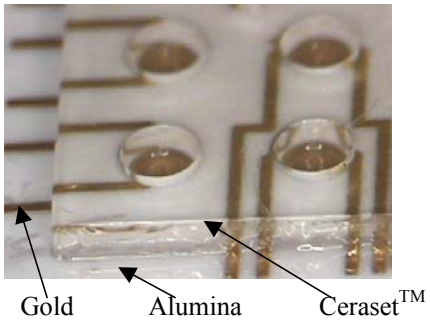

Figure T5- 30. Left: Photograph of the top view of the alumina substrate, with patterned gold heaters. The line width of the spirals is 35 microns. Right: Photograph of the fabricated Ceraset™ cells (about 500 microns thick) on the substrate. (Photos courtesy of Mr. Erwin Hoo, University of Colorado.)

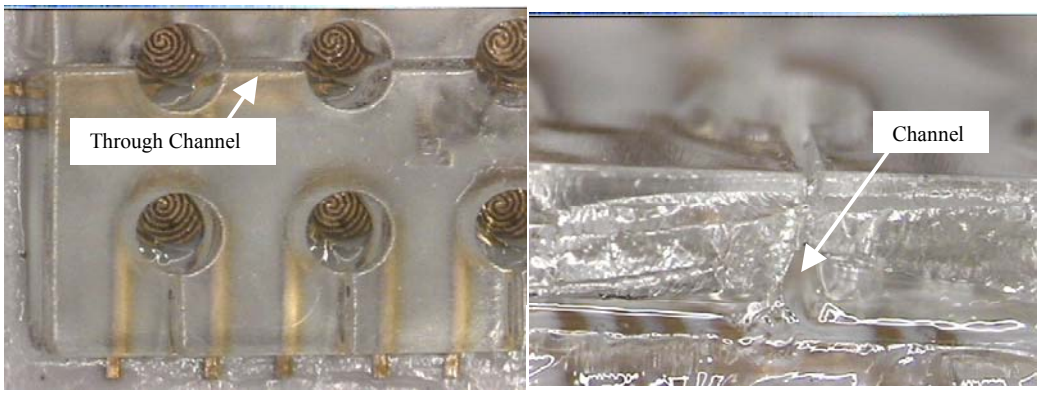

Figure T5- 31. Double-layered Ceraset™ cells on substrate.

Left: top view, showing slight misalignment with the underlying heaters. Note that the heaters on the substrate are visible through the two polymer layers. Right: Side view, looking into a channel. Clearly visible are the two polymer layers, which together are about 1 mm tall. (Photos courtesy of Mr. Erwin Hoo, University of Colorado.)

8. "Micro Packages for Nano Devices"

(supported by DARPA; PI: Prof Victor M. Bright; Postdoctoral research associate: Kevin Harsh; Dept of Mechanical Engineering, University of Colorado at Boulder)

Another funded MEMS project that benefited from the SiCN-MEMS technology centers around the idea of fabricating micro "caps", or enclosures directly on top of surface-micromachined devices for device-level vacuum packaging. SiCN was found to be a good candidate for a first prototype due to the combination of low-cost fabrication /manufacturing flexibility which is characteristic of polymer fabrication, and the robust mechanical properties of ceramics. Figure T5- 32 shows scanning electron micrographs of two of these micro packages. This effort was first reported in our DARPA technical report from June 2002.

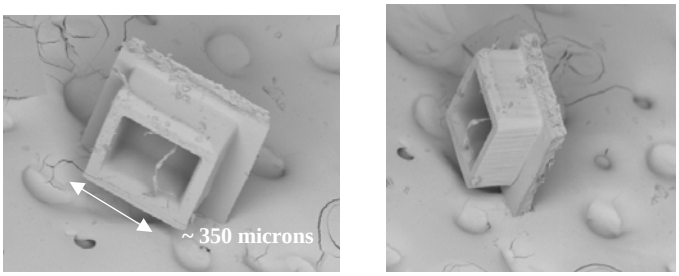

Figure T5- 32. SiCN "caps" for device-level encapsulation of MEMS. Courtesy of Dr. Kevin Harsh.

9. SiCN Micro Combustion Chamber

MEMS based devices are being considered for electric power generation by converting the stored chemical energy of liquid hydrocarbon fuels to electrical energy on a micro scale. The attractiveness of this goal is based on the fact that hydrocarbon fuels have enthalpies of combustion on the order of 45,000

kJ/kg. For a power rating of 1 mW, an energy conversion system with just 1% overall efficiency would be able to operate approximately 100 hours on about one gram or 1 cm^3 of fuel. However, current materials are limited in temperature range and demonstrated lifetimes, and operational issues of ignition and heat losses remain. As part of a DARPA funded research project to develop high temperature materials for use in MEMS devices, we have been working to design, fabricate and test combustor configurations and assess methods for flame ignition and stabilization and heat transfer control.

Design and Fabrication

The fabrication approach for the SiCN combustion chamber has been to use the direct-photopolymerization method (see Task 3) to fabricate a floor layer, then to fabricate a channel layer on top of that, and to fabricate separately a lid layer that would then be bonded onto the channel layer using the Polymer-Bonding method (see Task 3). The geometry of the channels has undergone several design changes. Initially a straight channel was made (see DARPA technical report from January 2000), then a swiss-roll configuration was made (see DARPA technical report from January 2001). However, to simplify calculations a return to a straight channel was then implemented, as reported in our DARPA technical report from September 2001.

It is important to design the overall dimensions of the chamber to enable gas diffusion out of the material during pyrolysis, preventing cracks. This is especially important since the chamber, comprising of three layers that need to be rigid enough to be manually assembled, is an especially thick structure with thickness on the order of 300 to 500 microns. The design and photographs of the combustion chamber are shown in
Figure T5- **33** and Figure T5- 34, respectively.

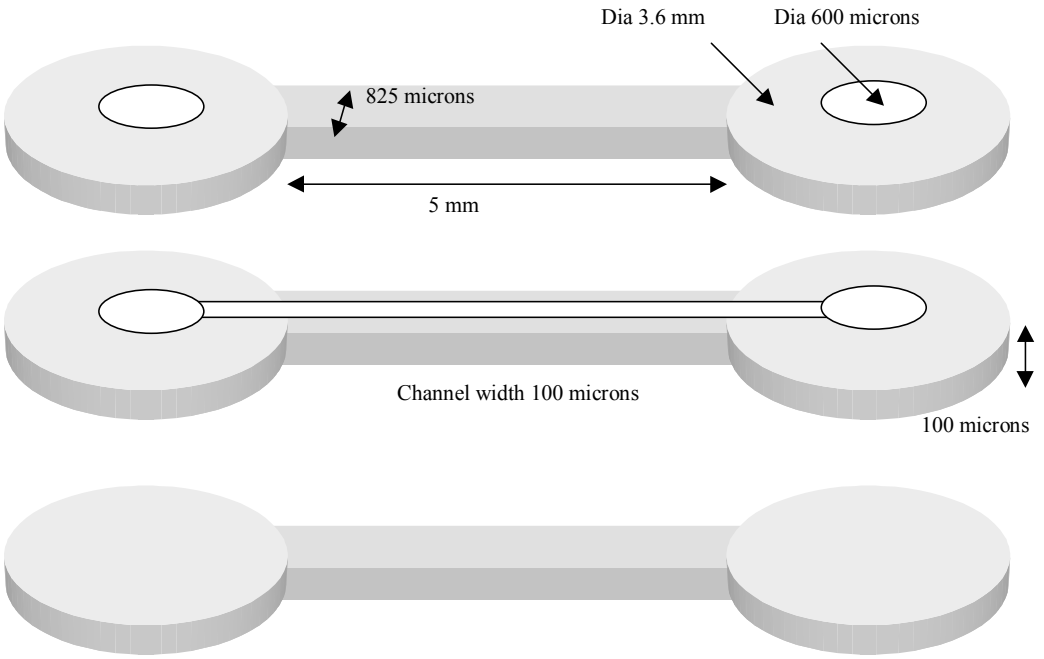

Figure T5- 33. Schematic of new chamber design.

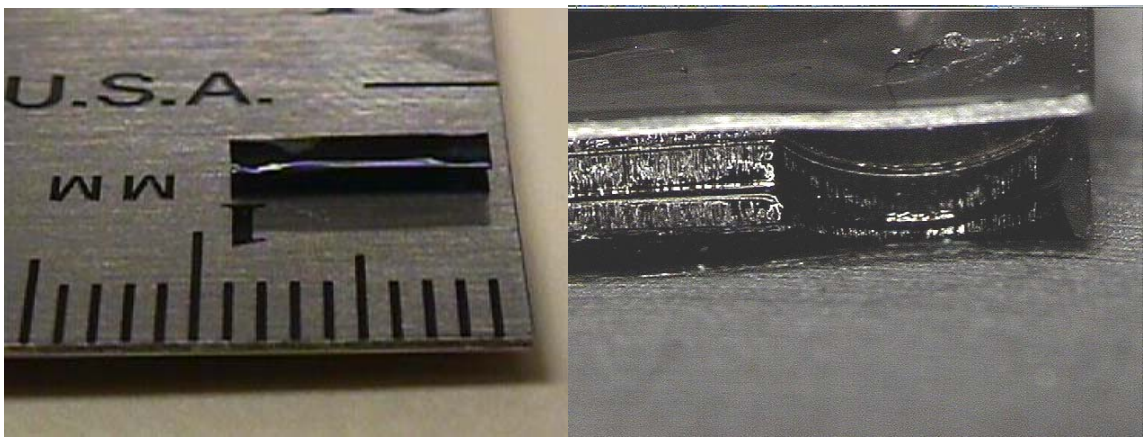

(a) (b)

Figure T5- 34. (a) SiCN combustion chamber on a metric ruler. (b) Closeup of the sideview of the combustion chamber, showing the three layers bonded together.

Modeling

The calculations were carried out using the CHEMKIN application CRESLAF. CRESLAF predicts the velocity, temperature, and species profiles in two-dimensional (planar or axisymmetric) channels. The program accounts for finite-rate gas-phase and surface chemical kinetics and molecular transport. The model employs the boundary-layer approximations for the fluid-flow equations, coupled to gas-phase and surface species continuity equations. The program employs the CHEMKIN, SURFACE CHEMKIN and TRANSPORT software packages for the gas-phase and surface chemical reaction mechanisms and for the transport properties.

CRESLAF solves the parabolized Navier-Stokes equations. To simplify the numerical procedure somewhat, the equations are recast using the Von Mises transformation, in which the cross-stream coordinate is replaced by the stream function as an independent variable. An additional transformation of the stream function is invoked that accounts for possible mass loss (or gain) in the gas due to deposition (or etching) at the reacting surfaces. The equations are:

Conservation of momentum:

$$\rho u\frac{\partial u}{\partial x}-\frac{\rho u}{M}\left(\xi\frac{dM}{dx}-\frac{dM_l}{dx}\right)\frac{\partial u}{\partial \xi}+\frac{dp}{dx}=\frac{\rho u}{M^2}\frac{\partial}{\partial \xi}\left(\rho u\mu y^{2\alpha}\frac{\partial u}{\partial \xi}\right)+g\left(\rho_i-\rho\right)$$

Conservation of species:

$$\rho u\frac{\partial Y_k}{\partial x}-\frac{\rho u}{M}\left(\xi\frac{dM}{dx}-\frac{dM_l}{dx}\right)\frac{\partial Y_k}{\partial \xi}=\dot{\omega}_k W_k-\frac{\rho u}{M}\frac{\partial}{\partial \xi}\left(y^{\alpha}\rho Y_k V_{k,y}\right)\qquad \left(k=1,\ldots,K_g\right)$$

Conservation of energy:

$$\rho u c_p \frac{\partial T}{\partial x} - \frac{\rho u c_p}{M}\left(\xi \frac{dM}{dx} - \frac{dM_l}{dx}\right)\frac{\partial T}{\partial \xi} = \frac{\rho u}{M^2}\frac{\partial}{\partial \xi}\left(\rho u \lambda y^{2\alpha}\frac{\partial T}{\partial \xi}\right) - \sum_{k=1}^{K_g}\dot{\omega}_k W_k h_k$$

$$-\frac{\rho^2 u y^{\alpha}}{M}\sum_{k=1}^{K} Y_k V_{k,y} c_{pk}\frac{\partial T}{\partial \xi}$$

In addition, the Ideal Gas Law is used as the equation of state. The gas phase chemistry was GRI-Mech 3.0[1] and the surface chemistry that of Deutschmann, et al.[2]

Model Results

The configuration explored is a channel of 200 microns in diameter. The length is 2 mm. For the calculations reported here, we used an entrance velocity of 400 cm/sec. Therefore, the average residence time is 0.5 msec. Because the small scale of the channel, the gas temperature rapidly assumes the temperature of the channel walls. For example, the thermal entry length

$$l_t = 0.05 D R_e P_r$$

is about one diameter.

A series of calculations assuming constant temperature were first carried out. The results are shown in Figure T5- 35 which plots centerline methane concentration as a function of distance through the reactor. As can be seen, no reaction occurs at 750 K. At 1000 K, reaction rates are sufficient to deplete most of the methane by the end of the reactor. Reaction rates become extremely fast for higher temperatures.

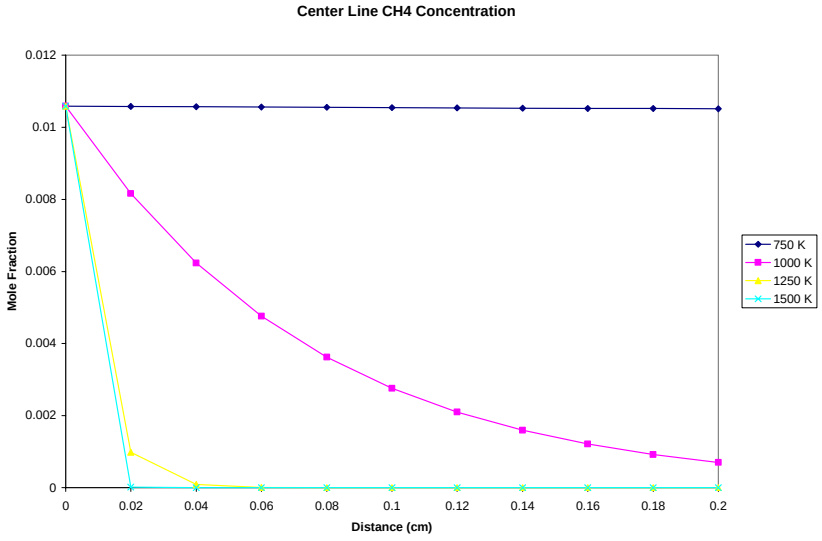

Figure T5- 35. Results of constant-temperature calculation.

An additional series of calculations were carried out assuming adiabatic conditions. This simulates a high degree of thermal control, with a thermal ignition device of some kind heating the gas prior to the entrance of the reactor. The results are shown in Figure T5- 36. Shown is the centerline gas temperature as a function of distance through the reactor. At temperatures above about 775 K, the reactor displays classic catalyst light off curves, with rapid reaction following an incubation period.

An interesting finding is that surface reactions dominate the chemistry. Figure T5- 37 shows the light off curve at 800K with and without gas phase reactions being included. As can be seen, the inclusion of gas phase reactions make no difference in the result. This was the case for all conditions examined.

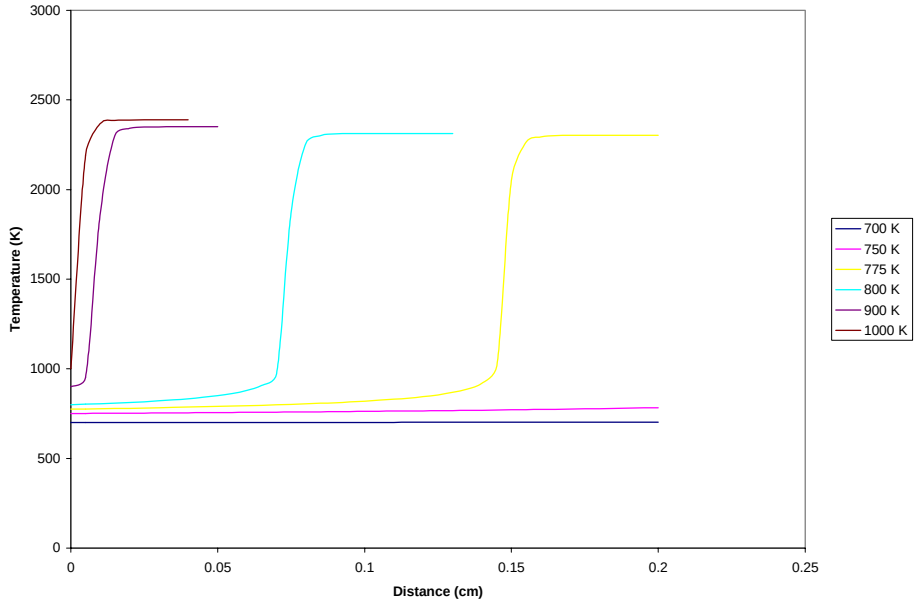

Figure T5- 36. Results assuming adiabatic condition.

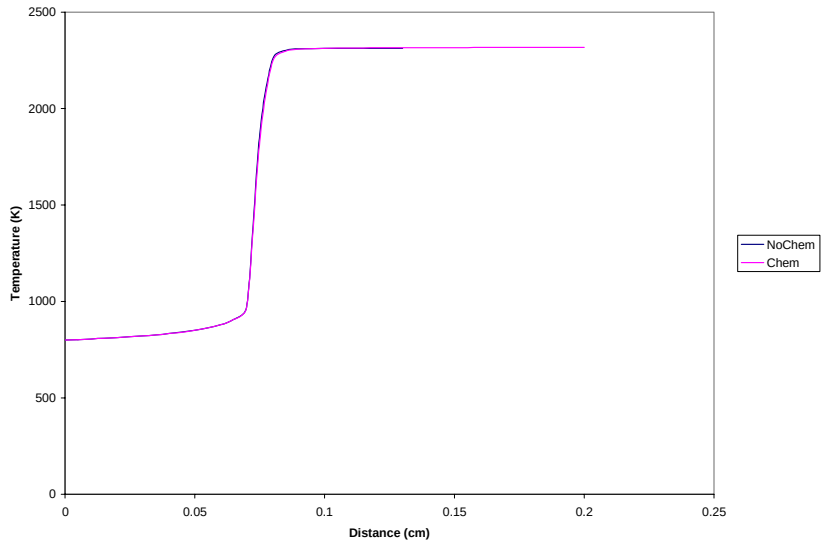

Figure T5- 37. Light-off curve at 800 K.

Conclusions

The main conclusion to be reached is that it will be extremely difficult to sustain reactions unless heat transfer is controlled and the reactor walls are catalytic for the reactants present. Gas phase reactions are fairly slow, and heat transfer is very rapid.

References for this section

1. Gregory P. Smith, David M. Golden, Michael Frenklach, Nigel W. Moriarty, Boris Eiteneer, Mikhail Goldenberg, C. Thomas Bowman, Ronald K. Hanson, Soonho Song, William C. Gardiner, Jr., Vitali V. Lissianski, and Zhiwei Qin, `http://www.me.berkeley.edu/gri_mech/`

2. Deutschman, O., R. Schmidt, F. Behrendt and J. Warnatz, Proceedings of the Combustion Institute, Volume 26, 1747 (1996).

Design of the Fluidic Flow System for Testing

A fluidic system for testing the combustion chamber has been designed, as shown in Figure T5- 38 and which was first reported in our DARPA technical report from September 2001. Based on results from Chemkin simulations (see DARPA report June 2001), this flow system is designed to provide small quantities of methane and oxygen in precise amounts as needed for combustion.

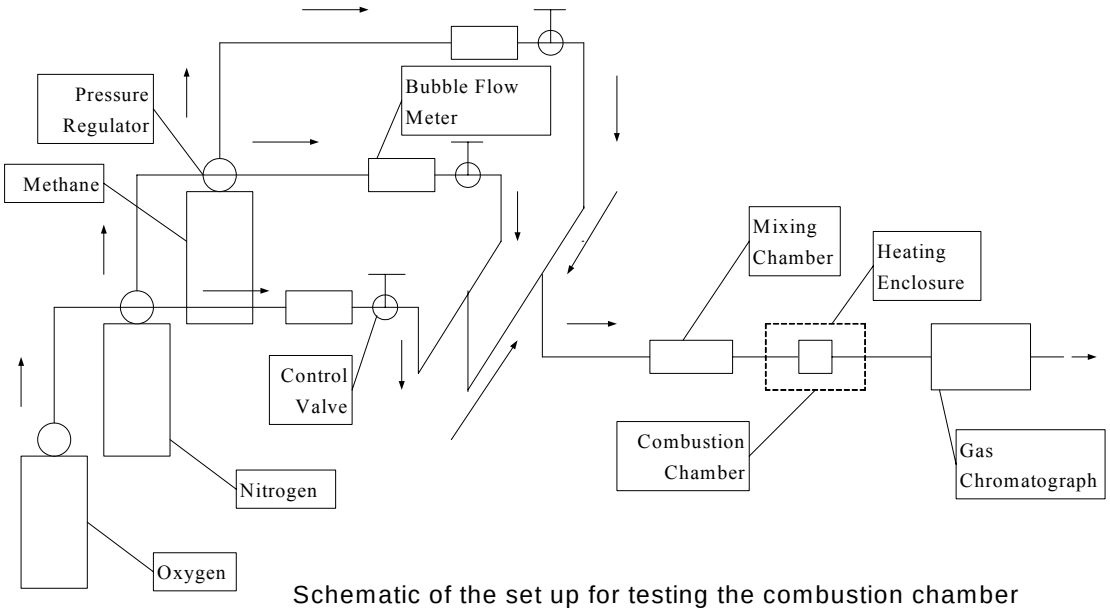

Figure T5- 38. Schematic for the SiCN combustion chamber integration into an experimental combustion system.

Task 6: Integration Technology

Several levels of integration have been demonstrated:

1. *Integration of SiCN MEMS with silicon-MEMS infrastructure.* These include the use of techniques that have been applied to the fabrication and packaging of commercially fabricated surface-micromachined MEMS. Examples of these techniques include XeF_2 etching, flip-chip bonding, wire-bonding, DIP packaging, and the use of basic photolithography systems and techniques. Furthermore, we have proven that we can leverage existing MEMS design knowledge to design SiCN MEMS, i.e. devices that have been made with silicon technology can also be implemented in SiCN and polysilazane technology. Examples of such devices (see DARPA reports Jan 2000 to present) include electrostatic and thermal actuators, pressure sensors, microfluidic channels, optical gratings. This level of integration is a significant achievement of this project because it enables SiCN MEMS technology to be more readily incorporated commercially.

2. *Integration of MEMS and Polymer-Derived Ceramic Fields*. Not to be underestimated is the significance of merging the two relatively new fields of MEMS and polymer-derived ceramics (PDCs). Prior to this project, these two fields existed separately, both being new areas of research that are less than twenty years old. Apart from the work performed by this group, research in the PDCs centers almost exclusively on synthesis and characterization of materials. The concept of fabricating micro devices from PDCs that can be used both in real-world applications and at the same time for in-situ property measurement, is completely novel to the PDC community. Because of this, this project has spawned new funded research into PDCs here at University of Colorado, based on devices such as the Micro Glow Plug and the electrostatic actuator.

3. *Integration between MEMS and software.* Finally, one new and exciting development in this project is work towards interfacing the Micro Glow Plug to a real-time "Human Machine Interface". This interface consists of a computer-controlled system that operates and characterizes the device to both provide real-time feedback on the device performance as well as to predict remaining device lifetime. This system is the result of a collaboration with faculty from Civil, Environmental and Architectural Engineering Department here at C.U.-Boulder, and would take SiCN MEMS research to the next level.

3. Administration

3.1 Personnel

Principal Investigator: Dr. Victor M. Bright
Co-Investigators: Dr. Rishi Raj, Dr. Martin L. Dunn, Dr. John W. Daily,
Postdoctoral Research Assistants: Dr. R.A. Saravanan (started June 2001), Dr. Linan An (until Dec 2000)
Graduate Research Assistants: Ms. Li-Anne Liew, Ms. Yiping Liu, Mr. Badrinarayan P. Athreya (started Jan 2001), Mr. Ruiling Luo (until Jan 2001), Mr. Tsali Cross (started January 2001)
Professional Research Assistant: Ms. Ann Geesaman

3.2 Publications Resulting from this Project:

1. L.A Liew, V.M. Bright and R. Raj, "A Novel Micro Glow Plug Fabricated from Polymer-Derived Ceramics: In-Situ Measurement of High-Temperature Properties and Application to Ultrahigh Temperature Ignition, Sensors and Actuators A: Physical, Volume 104, Issue 3, 15 May 2003, Pages 246-262

2. L.A. Liew, R.A. Saravanan, V.M. Bright and R. Raj, "Processing and Characterization of Silicon Carbon-Nitride Ceramics: Application of Electrical Properties Towards MEMS Thermal Actuators, Sensors and Actuators A: Physical, Volume 103, Issues 1-2, 15 January 2003, Pages 171-181.

3. T. Cross, L.A. Liew, V.M. Bright, M.L. Dunn, J.W. Daily, and R. Raj, "Development of Fabrication for Ultra-High Aspect Ratio Polysilazane MEMS", Sensors and Actuators A: Physical, Volume 95, Issues 2-3, 1 January 2002, Pages 120-134

4. R.A. Saravanan, L.A. Liew, V.M. Bright and R. Raj, "Silicon Carbon-Nitride Ceramics – a High-Temperature Semiconductor Material for MEMS Applications," *Proceedings of the 35th International Symposium on Microelectronics (IMAPS 2002)*, International Microelectronics and Packaging Society, Denver, CO, September 4-6, 2002.

5. L.A. Liew, V.M. Bright and R. Raj, "A Novel Micromachined Glow Plug for Ultrahigh Temperature Ignition Applications," *Proceedings of the 2002 Solid-State Sensor, Actuator and Microsystems Workshop (Hilton Head 2002)*, June 2-6, Hilton Head Island, South Carolina, pp. 243-246, 2002.

6. Y. Liu, L.A. Liew, R. Luo, L. An, M.L. Dunn, V.M. Bright, J.W. Daily and R. Raj, "Application of Microforging in SiCN MEMS Structure Fabrication," *Sensors and Actuators*, vol. A-95, no. 2-3, pp. 143-141, 2002.

7. L.A. Liew, Y. Liu, R. Luo, T. Cross, L. An, V. M. Bright, M. L. Dunn, J. W. Daily and R. Raj, "Fabrication of SiCN MEMS By Photopolymerization of Pre-Ceramic Polymer," *Sensors and Actuators*, vol. A-95, no. 2-3, pp. 120-134, 2002.

8. L.A. Liew, W. Zhang, V. M. Bright, L. An, M. L. Dunn and R. Raj, "Fabrication of SiCN Ceramic MEMS Using Injectable Polymer-Precursor Technique," *Sensors and Actuators*, vol. A-89, no. 1-2, pp. 64-70, 2001.

9. L.A. Liew, V.M. Bright, M.L. Dunn, J.W. Daily and R. Raj, "Development of SiCN Ceramic Thermal Actuators," *Proceedings of the 15th Annual International Conference on Micro Electromechanical Systems (MEMS2002)*, Las Vegas, Nevada, pp. 590-593, Jan 20-24, 2002.

10. T. Cross, L.A. Liew, V.M. Bright, M.L. Dunn, J.W. Daily and R. Raj, "Fabrication Process for Ultra High Aspect Ratio Polysilazane-Derived MEMS," *Proceedings of the 15th Annual International Conference on Micro Electromechanical Systems (MEMS2002)*, Las Vegas, Neveda, pp. 172-175, Las Vegas, Nevada, Jan 20-24, 2002.

11. L.A. Liew, T. Cross, V.M. Bright and R. Raj, "Fabrication of Novel Polysilazane MEMS Structures by Micro Casting," *Proceedings of the 2001 ASME International Mechanical Engineering Congress and Exposition (IMECE 2001)*, CD-Vol.2, No. MEMS-23920, New York, NY, Nov 11-16, 2001.

12. L.A. Liew, W. Zhang, L. An, S. Shah, R. Luo Y. Liu, T. Cross, K. Anseth, M.L. Dunn, V.M. Bright, J.W. Daily and R. Raj, "Ceramic MEMS – New Materials, Innovative Processing and Future Applications," *American Ceramic Society Bulletin*, Vol. 80, no.5, pp. 25-30, May 2001.

13. L.A. Liew, Y. Liu, R. Luo, L. An, V.M. Bright, M.L. Dunn, J.W. Daily, and R. Raj, "Fabrication of a MEMS SiCN Pressure Sensor Using Photopolymerization," *Proceedings of the 47th International Instrumentation Symposium*, Denver, Colorado, 6-10 May 2001.

14. Y. Liu, L.A. Liew, R. Luo, L. An, V.M. Bright, M.L. Dunn, J.W. Daily, and R. Raj, "Fabrication of SiCN MEMS Structures Using Microforged Molds," *Proceedings of the 14th Annual International Conference on Micro Electromechanical Systems (MEMS2001)*, pp. 118-121, Interlaken, Switzerland, Jan 21-25, 2001.

15. L.A. Liew, R. Luo, Y. Liu, W. Zhang, L. An, V.M. Bright, M.L. Dunn, J.W. Daily, and R. Raj, "Fabrication of Multi-Layered SiCN Ceramic MEMS Using Photo-Polymerization of Precursor," *Proceedings of the 14th Annual International Conference on Micro Electromechanical Systems (MEMS2001)*, pp. 86-89, Interlaken, Switzerland, Jan 21-25, 2001.

16. L. An, W. Zhang, V.M. Bright, M.L. Dunn and R. Raj, "Development of Injectable Polymer-Derived Ceramics for High Temperature MEMS," *Proc. Thirteen Annual International Conference on Micro Electro Mechanical Systems (MEMS 2000)*, Jan 23-27, 2000, Miyazaki, Japan, pp 619-23.

3.3 Patents/Inventions:

1. L.A. Liew and R. Raj, "Ultrahigh Temperature Micro Glow Plug," *Non-Provisional Patent Application filed November 7, 2001 by Patton Boggs LLP; PB Ref: 13743.101; C.U. Ref No.2001.037B.*
2. L.A. Liew, R. Raj, R.A. Saravanan, A. Saha, V.M. Bright, "Microsystems Fabricated from Polymer-Derived, Multifunctional Si-C-N Ceramics," *Invention Disclosure submitted to the C.U. Office of Technology Transfer and Industry Outreach, February 27, 2002, C.U. Ref No. 2002.078B.*

3.4 Student Theses:

1. L.A. Liew, “Polymer-Derived Silicon Carbonitride as a New Technology for Microelectromechanical Systems.” Doctoral Thesis, University of Colorado at Boulder, Department of Mechanical Engineering, 2002.

2. T. Cross, “Phenomenological Studies of Photopolymerization in Poly-urea-methyl-vinyl-silazane for Applications in the Fabrication of Polymer-Derived Ceramic MEMS Devices,” Masters Thesis, University of Colorado at Boulder, Department of Mechanical Engineering, 2002.

4 Extension Project: Micro-Packages for Nano-Devices

4.1 Summary of Research Objectives

Packaging of MEMS is a critical technology necessary to bring MEMS components to real applications. The objectives of this seed research project are to investigate a new micro-packaging technology to create a high-vacuum, hermetically sealed local environment for nano-devices integrated with other electronic or RF circuits. The basic premise (Figure MC-1) is to create a localized micro-cap over the MEMS structure and then form a glass (or other hermetic material) droplet on the device using existing jet-based technologies. The process fits within the standard manufacturing infrastructure, and due to its excellent manufacturability, it can be scaled to package MEMS or nano devices. The package size can range from millimeter size to 10 μm x 10 μm x 10 μm. Such a micro-package will be critical to the advancement of micro and nano-devices such as nano sized resonators that require high vacuum and clean environment to maintain Q's on the order of 10,000 or higher, or very advanced RF MEMS where localized packaging can greatly affect device performance.

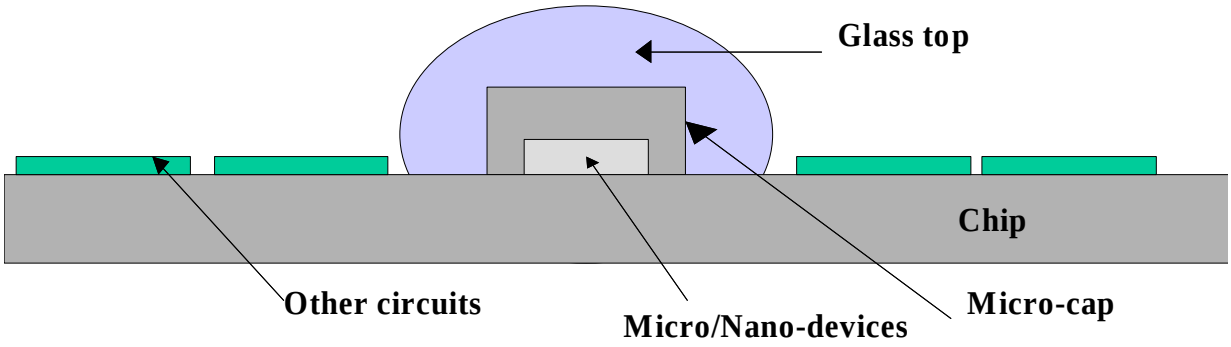

Figure MC-1: Micro-package for nano-devices on a chip.

The research objectives are to develop and demonstrate a proof of principle encapsulated MEMS device using this technology. Particularly, two challenges were identified in the initial proposal:

Challenge 1: Precision creation of the micro-cap: Proposed studies: we will improve micro-cap design, either using solder deposition and reflow to achieve polysilicon box, or other micro-fabrication technologies to create caps ranging from 10 to 1000 microns across.

Challenge 2: Deposition of glass droplets in vacuum: Proposed studies: we will demonstrate the deposition of hermetic sealing droplets (glass or other) in vacuum using laboratory tools. The major challenges are tooling and outgasing. A simple laboratory-dispensing tool will be designed and prototyped. The entire tool containing sealing material and actuation unit will be located inside a vacuum chamber. Hermetic suitability of these materials will be characterized in details to understand how low a vacuum and/or hermetic environment can be achieved.

Deliverable: The final deliverable for this project will be to demonstrate a MEMS sensor hermetically sealed in vacuum. The sensors performance will be measured as a function of time to demonstrate the vacuum and hermetic sealing levels.

5. Technical Report

5.1 Task Schedule

For reference, the schedule of tasks determined through the duration of the project is included below. The blue shaded time period blocks indicate task completion. The progress of individual tasks is given in Section 2.2.

Task 1	Creation of the micro-cap through precision solder-assembly or micro-fabrication	Q1	Q2	Q3	Q4
1	Evaluate the creation of a micro-cap using precision solder self-assembly	■	■	■	
2	Evaluate the creation of a micro-cap using other microfabrication technologies	■	■	■	
3	Design a MEMS sensing device to monitor the performance of the microcap		■		
4	Fabricate proof of principle micro-cap structures		■	■	■
5	Fabricate proof of principle MEMS sensing structures		■	■	
6	Experimentally verify/calibrate the MEMS sensing structures			■	■

Task 2	Deposition of glass droplets in vacuum	Q1	Q2	Q3	Q4
1	Outline, and evaluate packaging system and required process	■	■	■	■
2	Design, construct, and test preliminary vacuum encapsulation system	■	■		
3	Evaluate appropriate sealing materials for application suitability		■	■	
4	Demonstrate preliminary encapsulated MEMS sensor in micro-package			■	■
5	Experimentally evaluate the preliminary micro-package			■	■

5.2 Task Summary

Task 1. Creation of the Micro-Cap through precision solder-assembly or Micro-fabrication

1a. Evaluate the Creation of a Micro-Cap Using Precision Solder Self-Assembly

The first of the two possible basic cap types is a solder assembled structure. The idea is to use a solder self assembled structure, fabricated with the standard MEMS technologies, as the framework of the lid. Solder self-assembly uses the surface tension properties of molten solder or glass as the assembly mechanism. The solder method involves using a standard hinged plate with a specific area metalized as solder wettable pads. Once the solder is in place, it is heated to its melting point, and the force produced by the natural tendency of liquids to minimize their surface energy pulls the free plate away from the

silicon substrate (Figure MC-2). Solder is a predominant technology for electronics assembly and packaging. It is not only used for electrical connections, but also for sub-micron accuracy alignment in many packaging applications such as optoelectronic passive alignment. Using solder, hundreds or thousands of precision alignments can be accomplished with a single batch reflow process, and the cost/alignment can be reduced by orders of magnitude. In addition, solder provides high quality mechanical, thermal and electrical connections. The extensive work done on solder self-assembly has shown that the technology is at least capable of assembling a MEMS structure to within 0.03 degrees of the desired angular position.

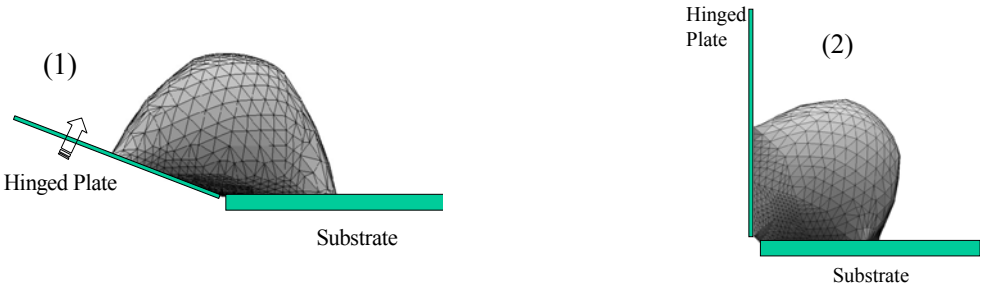

Figure MC-2: Illustration of solder self-assembly of hinged MEMS plate. (1) During reflow. (2) Equilibrium position.

The use of solder self-assembly to create a box or other structure over a device to serve as a lid is fairly straightforward. Many such device configurations are possible, restricted only by the requirement that they are composed of individual hinged plates. One such structure is shown in Figures MC-3 and MC-4. The figures show a six-sided box formed around a comb drive resonator. Figure MC-3 is a top down photograph of an unassembled device with solder in place, and Figure MC-4 is a SEM micro-graph of a partially assembled box such that one can see the device inside. Many variations of such enclosures are possible; another variation is shown in Figure MC-5, a structure that uses thatched beams to form a cavity. The evaluation of the feasibility of the various designs is a fundamental part of this work.

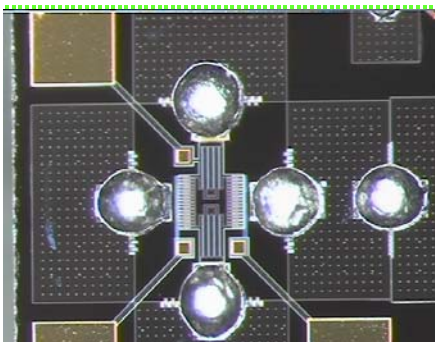

Figure MC-3: A micro resonator fabricated with five polysilicon plates and solder bumps.

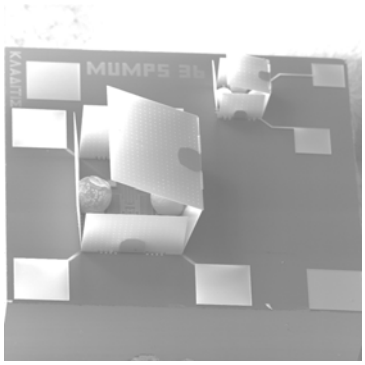

Figure MC-4: Micro-resonator enclosed by the plates after solder reflow. The box is not completely closed to illustrate the concept.

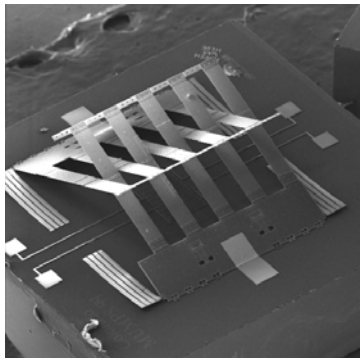

Figure MC-5: A device cover using thatched beams as the structural members.

To evaluate the feasibility and viability of different MEMS structures, several variations were fabricated using the Cronos MUMPs process. This included boxes of various sizes, 3 and 4 sided pyramids, and a number if interlaced structures as shown in Figure MC-5. A large portion of these devices were assembled and covered in sample sealing materials. The results were:

- For high surface tension, wetting, sealant liquids, the device was consistently destroyed. This makes sense given the high amount of force generated by the surface energy warping the structure.
- For low surface tension, wetting liquids, the device would remain intact, but the sealing material would flow through the very fine cracks (2-10 microns) and fill or cover the interior of the cap and the sensing structure.
- Poor wetting liquids would simply slide off the structure and not fully encapsulate the cap.

The conclusion of this preliminary study is that the sealing material is crucial if using self-assembled MEMS structure as the cap. A study of appropriate sealing materials requires further investigation.

1b. Evaluate the Creation of a Micro-cap Using Other Micro-Fabrication Technologies

In addition to creating a cap using self-assembly, other methods of cap creation have been investigated. The basic concept is to batch fabricate individual cap parts using one of a number of possible micro-fabrication technologies. This cap would then be pick and place attached in a manner similar to die attach technology in standard microelectronics manufacturing. The cap would then be encapsulated in the same jet based method as the caps described in the previous section. This method has the benefit of being very flexible in the choice of material and configuration of the cap. The drawback is the additional fabrication steps, and the potential scaling issues with some fabrication methods. The requirements of such a cap are:

- Must stand up to the encapsulation conditions, i.e. temperature, out gassing.
- Must be able to create a chamber ranging from 10 to 1000 microns across, and at least 25-micron cavity height.
- Must emphasize manufacturability and cost effectiveness.
- Should have minimal permeability and be able maintain a hermetic seal, the importance of such depending on the packaging configuration and application.

The processes evaluated in this work are:

Polymer-based fabrication: One option for creating a cap is to use standard photo-reactive polymers and lithography. Using any thick film photo-patternable material, it is fairly straightforward to make a cap structure. We have created cap structures using Ceraset and SU-8 photo resist, with good results. Figure MC-6 shows a typical polymer cap, approximately 400 microns across at its widest point. The internal cavity is approximately 40 microns deep.

Pros: Extremely cost effective, simple, and flexible batch manufacturing process.

Cons: Polymer materials have high gas permeability and outgassing, and typically cannot stand up to high temperatures.

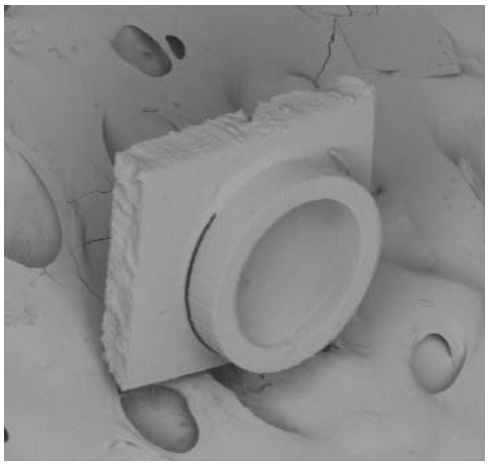

Figure MC-6: SEM micrograph of a Ceraset cap approximately 400 micron across.

Polymer-derived SiCN fabrication: Silicon carbonitride (SiCN) is a novel material belonging to the class of recently developed polymer-derived ceramics. The starting material is a liquid organic precursor, which can be micromachined into polymeric MEMS components, and then pyrolyzed to produce an amorphous bulk ceramic structure. The ceramic material is stable to temperatures exceeding 1500 ^{o}C, and has very high creep resistance, thermal shock resistance and oxidation resistance at these temperatures, making it highly attractive for applications involving ultrahigh temperatures, strong temperature gradients, or chemically corrosive environments. The material can also be altered at the molecular level for tailored mechanical, electrical, magnetic, thermal and optical properties. At the University of Colorado, we have developed a technology to fabricate functional MEMS devices from SiCN for use in ultrahigh temperature and harsh environment applications. We have fabricated a number of different size caps using SiCN (Figure MC-7). These caps have been used in some of the preliminary encapsulation prototypes discussed later.

Pros: Extremely tailorable material, and its polymer-derived nature make it very simple to use. In ceramic form, it is extremely durable and temperature resistant.

Cons: The material itself is still novel, and many physical characteristics are still unknown, and no mass-fabrication infrastructure currently exists.

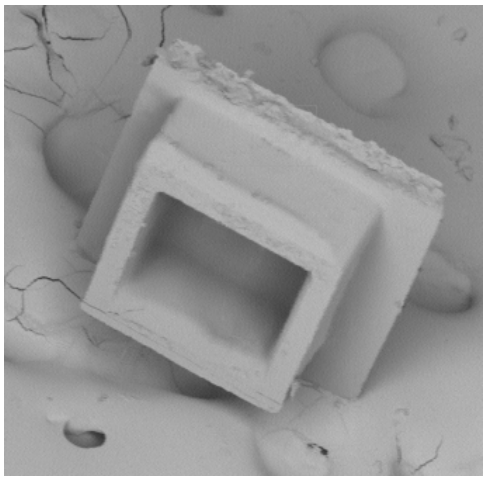

Figure MC-7: SEM micrograph of a SiCN cap, approximately 500 microns across.

Deep Reactive Ion Etching (DRIE): Reactive ion etching is now a common way of making high aspect ratio structures. Moreover, the typical materials include glass, silicon, and metals, which are all highly attractive for this encapsulation effort. The creation of a cap is effectively a two-step etch process. The first etch being the creation of the cavity, the second being for the separation of the parts. For larger parts, it may be possible to dice around the cavities rather than DRIE.

Pros: Batch manufacturing, precision, and extremely good materials. Due to their extremely low permeability and moisture resistance, the glass and silicon would be optimum materials for hermetic packaging.

Cons: High precision, slow process will effect the mass manufacturability of caps.

SOI Fabrication: Another possible technology is silicon on insulator (SOI) micro-machining. Again, the materials inherent in the process are highly attractive for hermetic sealing, and the process allows for very

precise shape definition. We have fabricated a number of cap samples in various sizes ranging from 100 to 1000 micron cavity sizes (Figure MC-8) using the Cronos SOI process. The caps consist of 50 micron sidewalls and have a cavity depth of 12 microns. There is a fundamental drawback of these types of caps in that the crystalline SiO_2 layer has a lower permeability compared to other materials. But this layer is very thin (~2 microns) and thus the effective area and leak rates should remain small.

Pros: Standard process, batch manufacturing, ideal materials, and excellent geometry tolerance control.
Cons: Semiconductor process may not be as mass production cost effective as other encapsulation processes.

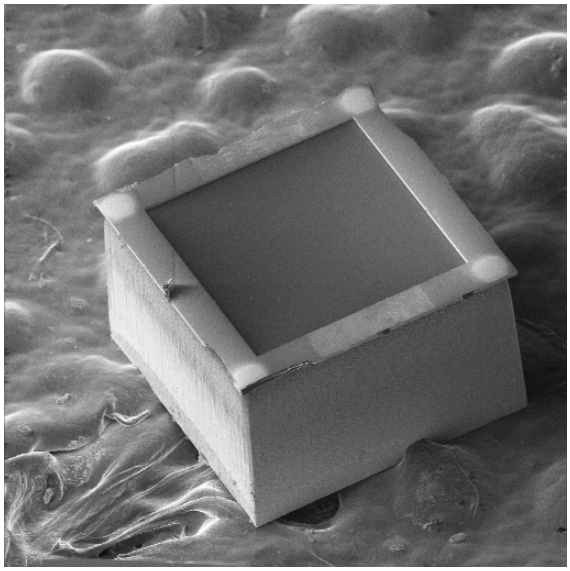

Figure MC-8: SOI fabricated Micro-cap.

Electroplating/LIGA: A standard mechanism for creating high aspect ratio structures is through micro-molding and electroplating. If the processing is done correctly, it can result in very well defined high-density structures in a variety of metals.

Pros: Standard, proven, micro-machining process, variety of metallic materials.
Cons: Processing restrictive, metals not acceptable for all applications, problematic tolerance control.

Glass Particulate Micro Casting: We have investigated a non-traditional micro machining process of casting or embossing glass particulates into the appropriate shapes. It is a very typical, cost effective process by traditional mass manufacturing standards. We have fabricated over 400 sample caps out of Corning Pyrex and Corning glass 7000. These caps have been used in some of the preliminary encapsulation prototypes discussed later. The one innate problem of this type of processing is because the material starts off in a particulate form, and is then compressed into shape, it is very difficult to achieve a non-porous material. Figure MC-9 shows the underside of one such cap, where the porosity of the material can be

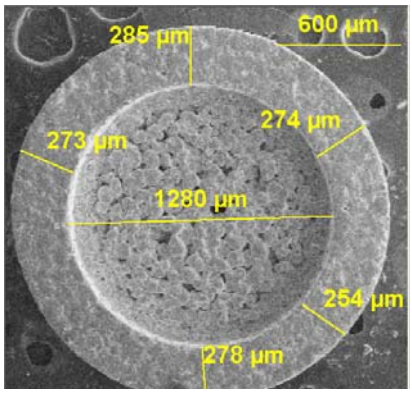

Figure MC-9: Top down view of a porous glass particulate micro-cast cap.

easily seen. Obviously, for material to be an acceptable hermetic sealing material, no amount of porosity is acceptable, and thus for these types of caps to be used in a final product they must be combined with an adequately impermeable sealing material.

Pros: Robust, cost-effective processing, temperature resistant materials.
Cons: Porous, limited to the geometry restrictions of the mold.

1c. Design a MEMS Sensing Device that Will Monitor the Performance of the Micro-Cap

One innate problem with developing this packaging technology is evaluating its quality. The question is, if the micro-package is not hermetic, how do we know? What is the measure of quality, and how do we perform that measurement. Typically, the standard method and measure for hermetic packaging is to use a helium chamber combined with a helium mass spectrometer to test the permeability of the package. Once the permeability to helium is known, the nature of the package leakage (fine, gross, diffusion) can be determined, and the permabilites of other gases and compounds can be determined. There are several problems with using such a system for this application. The foremost is that the extremely small potential size of our cavity will require an extremely sensitive mass spectrometer to detect the very few atoms coming from the package. Second, the specialized mass spectrometers for package evaluation are often not readily available. Finally, the mass detector system is a process/manufacturing characterization tool, and does not lend itself well to prototyping and individual device monitoring. A solution is to include, in the micro-package, a sensing device that can evaluate the hermiticity over time. However, a MEMS mass spectrometer is not a simple/established device to create. When we say we want to test hermiticity, what we want is to know the rate of influx of various atmosphere components such as gases and water. Unless there is a catastrophic package failure, the flux is in the form of molecular diffusion through the solid, which means what we really want to know/measure the material permeability.

A simple way to measure the permeability is to evacuate the cavity to a known level and measure the change in vacuum with respect to time. If done in a consistent environment (helium, nitrogen), the permeability of the package to that gas can be calculated based on the vacuum change, and thus the permeability to other gasses can be thermodynamically calculated. These permeabilities are valid weather the device is at vacuum or not, and they are the basis for hermiticity standards such as MIL-883. Thus a vacuum sensor can be used, and it should be small enough to fit inside the micro-package. The vacuum sensor device we designed is diagramed in Figure MC-10. The concept is based upon the change in electrical resistively in polysilicon at different temperatures. The device is effectively a pair of long thin coils suspended on posts anchored to the substrate. As one of the coils is electrically heated, the heat is conducted through the gas environment to the opposite coil and the substrate. By changing the level of vacuum in the chamber, the heat conducted to the second coil is affected, thus, the change in resistance of the second coil (or of the first coil depending on the sensing circuit design). This concept is the basis of the common macro scale hotwire/thermocouple vacuum gauges, which are typically used to measure vacuum in the range of 100 to 10^{-4} torr. There are other MEMS devices that were considered as a vacuum sensing mechanism, including resonators and pressure sensitive membranes. But, none matched the MEMS hot wire sensors simplicity and flexibility. For example, the resonator would likely need complicated associated capacitance sensing circuitry in order to detect a resonance change in the device.

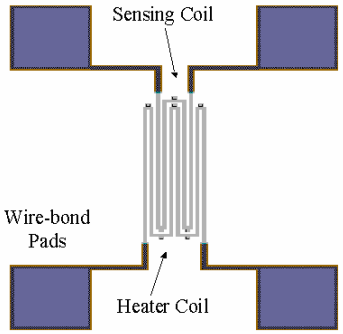

Figure MC-10: Computer (L-Edit) circuit layout for the MEMS hot wire thermal sensor.

1d. Fabricate Proof of Principle Micro-Cap Structures

Micro cap structures have been created using the polymer fabrication, the polymer based SiCN fabrication, SOI fabrication, and glass particulate microcasting. The optimal cap structure is of course dependant on the encapsulation. If a "diffusion and seal" method is used then the glass particulate micro-cast cap is the optimum solution because of it low cost, high manufacturability. But, if permeability is the problem, then SOI or DRIE caps are optimal because of their highly suitable materials and precise definition control.

1e. Fabricate Proof of Principle MEMS Sensing Structures

For this work, several iterations of the vacuum sensor design have been fabricated using the Cronos MUMPs process. They include designs that vary in length, thickness (resistivity), layout configurations, and layer type. The devices have been used in the package verification experiments discussed below.

1f. Experimentally Verify/Calibrate the MEMS Sensing Structures

Once the prototype devices were fabricated, it was necessary to experimentally verify their functionality, and calibrate them for use in the micro-package. Calibration was needed because, despite the availability of models, the exact response and the repeatability of the sensor to vacuum was not precisely known. This testing and calibration was performed in a MMR Technologies vacuum probe system capable of probing MEMS devices (Figure MC-11) in vacuums as low as 1 millitorr. The calibration was done by evacuating the chamber down to a specified level, and ramping the voltage/current through the heating coil, and measuring the response in the resulting resistance change in the sensing coil of the micromachined vacuum sensor. A sample result is shown in Figure MC-12. With the devices properly calibrated, they could then be used to evaluate micro-package quality.

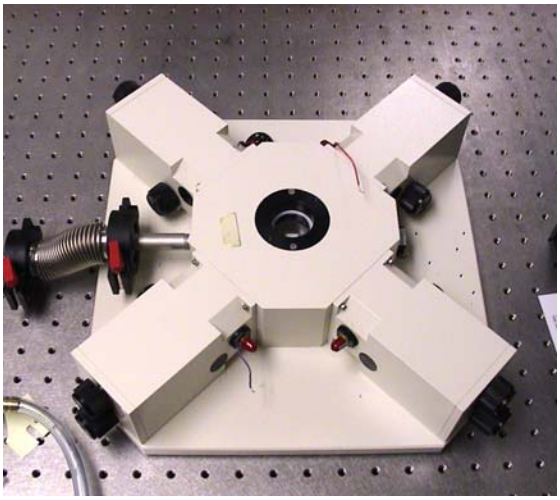

Figure MC-11: Photograph of the MMR Technologies vacuum probe station.

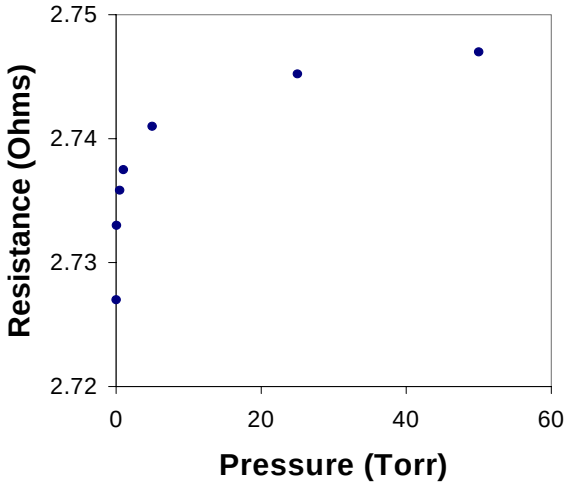

Figure MC-12: Typical calibration data for micromachined hotwire vacuum sensor.

Task 2. Deposition of Glass Droplets in Vacuum

2a. Outline and Evaluate Packaging System and Required Process

Although we initially proposed a process for creating a micro package through the use of speed deposited micro droplets, it was important for us to do a thorough evaluation of the process and gauge its feasibility and applicability. This evaluation was an ongoing process, the involved input from the fabrication results and the proof of principle experiments. For example, initial trial in micro-package assembly led to define potential die attach process and choice of acceptable encapsulation materials. Similarly, the first set of experiments using a vacuum system helped identify intrinsic alignment issues related to applying droplets in a high vacuum. The result of this evaluation was the proposal of several potential encapsulation systems/processes designs (described below).

Process 1: In Vacuum Micro-jet

This is the flagship methodology for this project, and has had the highest level of development. The concept, as described in previous sections, is simple. A cap (MEMS or micro-fabricated) is formed or placed over the desired MEMS structure. Rather than sealing the cap-substrate interface, the cap is instead encapsulated with an appropriate material (glass, metal) using high speed micro-jet technology (Figure MC-13). This approach allows for the cap to be attached and permanently sealed, while allowing for arbitrary surface roughness or electrical feed though lines. The entire process is performed in a vacuum or controlled environment, thus controlling the environment inside the package. The technology is based upon the solder jet technology developed by MicroFab Technologies, Inc. This technology is based on piezoelectric demand-mode ink-jet printing technology and is capable of placing molten solder, polymer or glass droplets, 25-125 μm in diameter, at rates up to 400 per second. The jet-based deposition requires no tooling; therefore, it is very flexible. The glass droplets can be deposited at any location on a chip or

on a wafer. Figure MC-14 shows the high temperature nozzle, the examples of resulting glass and solder bumps, and bump patterns.

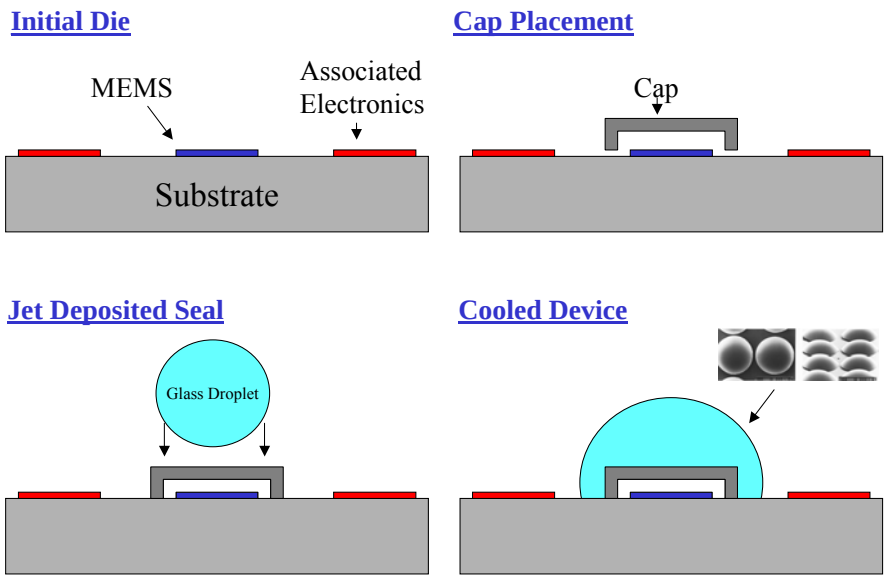

Figure MC-13: Diagram of the "In Vacuum Jet Deposition" packaging process.

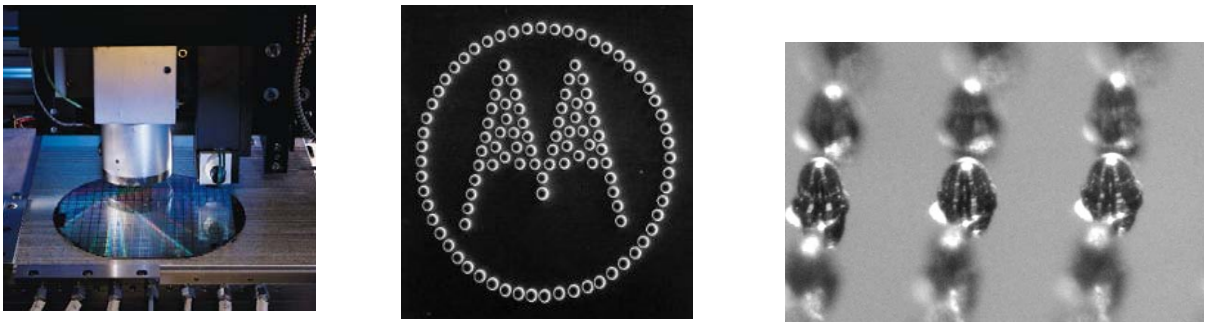

Figure MC-14: (Left) Photograph of the MicroFab jet deposition nozzle working on a six-inch wafer.

(Middle) Sample potential pattern created by the jet system, the spots are 50 microns across. (Right) Close-up of glass caps created by the jet system (~50 microns).

Process 2: Diffusion Evacuation and Furnace Sealing

There are several difficulties with the previous process configuration. The first is the system requires a high melting temperature liquid, which means a complicated heated nozzle system and a potentially complicated thermal management problem of keeping the liquid molten until the seal is made. Another potential problem is the inclusion of the jet system, feed-throughs, and material transfer in a vacuum or controlled environment. A second configuration addresses these problems by separating process into a jet deposition or die attach step and an evacuation/sealing step. Figure MC-15 illustrates the basic process. First the cap (in this case a micro-fabricated cap) is lined with a attach material and placed, at atmosphere and a low temperature, about the MEMS device. The attach material can either be a simple die attach epoxy or a two-phase glass material. Figure MC-16 shows a photograph of the underside of the die

attached porous cap taken through the attached glass substrate. If epoxy is used, a drop of the two-phase glass should be jet deposited on top. The two-phase glass material has low temperature set point (100 ^{o}C) in which it is a solid, but porous material. When heated to 400-600 degrees C, the material transitions into a highly dense, non-porous glass. After the low temperature, atmospheric, deposition, the device is placed in a vacuum or environmental chamber and the atmosphere is allowed to diffuse/flow through the porous material. The chamber is then heated to the appropriate temperature, and the glass seals the micro-package.

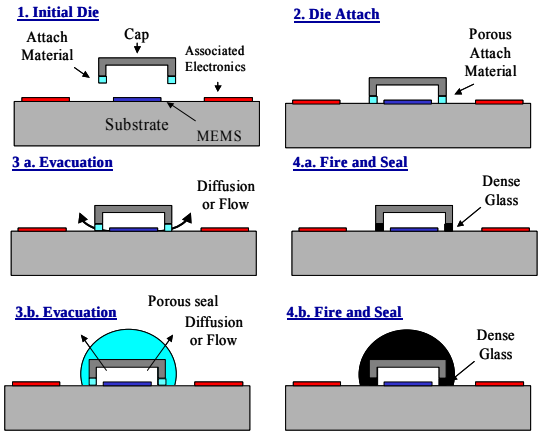

Figure MC-15: Diagram of the "Diffusion Evacuation and Furnace Sealing" process.

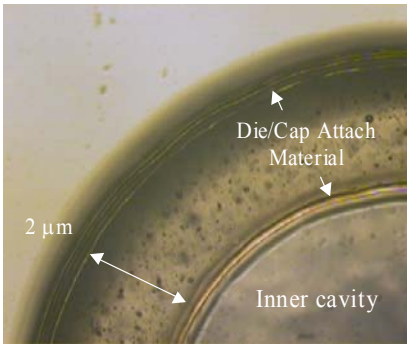

Figure MC-16: Photograph of the porous cap-glass substrate interface, showing the completeness of the attach material seal.

Process 3: Diffusion Evacuation and Pulse Laser Sealing

The previous configuration still has one major drawback; the furnace heating requires that the MEMS structure and associated microelectronics undergo the same heat treatment. This could be detrimental to many MEMS structures and microelectronics in which the metalization and doping are susceptible to degradation at high temperatures. For example, gold on polysilicon will form a number of intermetallics above 250 ^{o}C, and could definitely not survive a 600 degree C heat treatment. Figure MC-17 shows one potential way in which this may be avoided. The process is identical to the previous process except, instead if heating the entire substrate and package, the sealing material is point heated using standard laser welding technology. The result is that the heating can be extremely localized, if designed correctly; it should be possible to raise the sealing material to appropriate temperatures while not damaging the close proximity MEMS. To verify this, we have performed a number of analytical investigations. Figure MC-18 shows one such example. Finite element modeling was extensively used to formulate the heat transfer problem, the model in Figure MC-18 shows one such configuration in which the temperature from the laser pulse can be dissipated such that the cap reaches 600 ^{o}C, but the location of the MEMS stays below 200 ^{o}C.

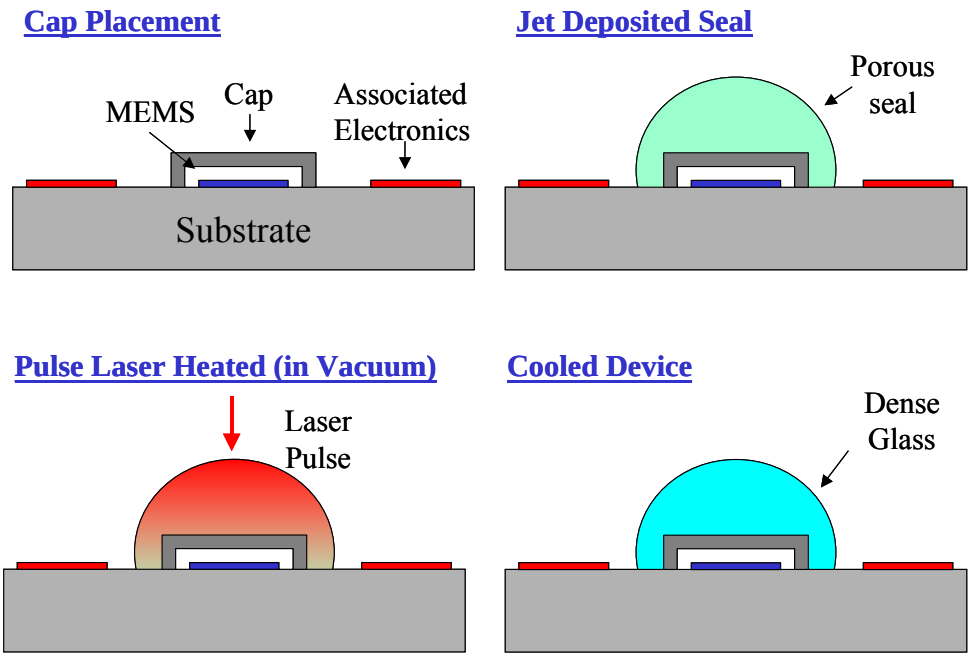

Figure MC-17: Diagram of the "Diffusion Evacuation and Pulse Laser Sealing" process.

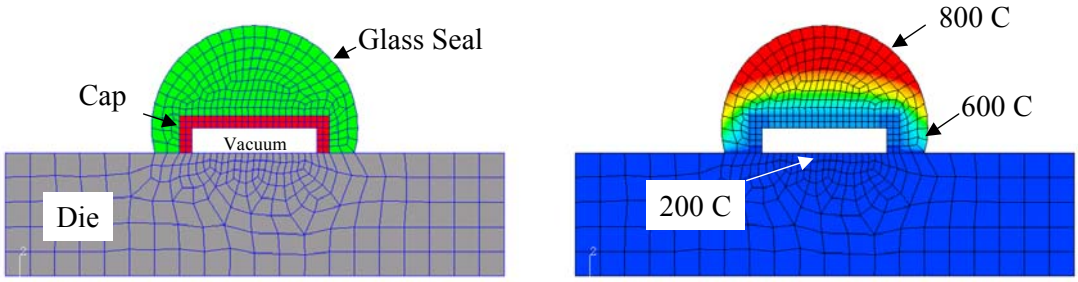

Figure MC-18: Sample finite element model of heat dissipation from laser pulse to cap structure. (Left) Geometry definition. (Right) Model prediction for temperature distribution.

2b. Design, Construct, and Test Preliminary Vacuum Encapsulation System

We have built vacuum encapsulation systems for this work, one each for process 1 and process 2 discussed above.

Vacuum Jet Deposition System

A preliminary system was constructed in order to package proof of principle devices (Figure MC-19 and 20). It was based on process 1 described above. The system consists of a series of steel connectors and feed-throughs arranged around a central chamber. The chamber contains a heated stage and an XYZ motion feed-through. The sealing liquid is flowed into chamber via liquid feed-through and pinch valves to a fixed position nozzle. For simplicity, we did not use the Micro-fab nozzle for the system. This integration requires significant effort and resources and is recommended for future work. The substrate and cap are positioned by adjusting the position of the stage. When the chamber is evacuated the liquid is

flowed in and deposited. The process is viewed through a glass window via a microscope. The entire system was assembled using CF copper seals and a Pirani/Cold Cathode gauge system and was built for vacuums as low as 10^{-9} torr. The system was used for all prototypes and experiments done for this project.

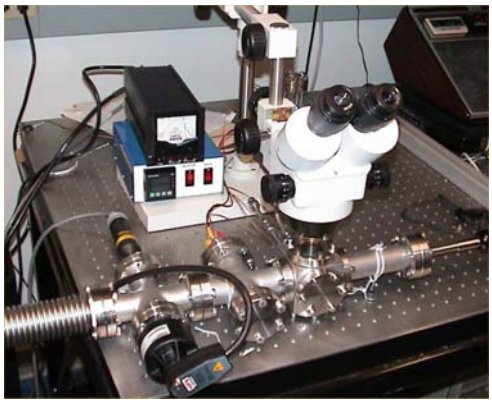

Figure MC-19: Photograph of preliminary vacuum encapsulation system.

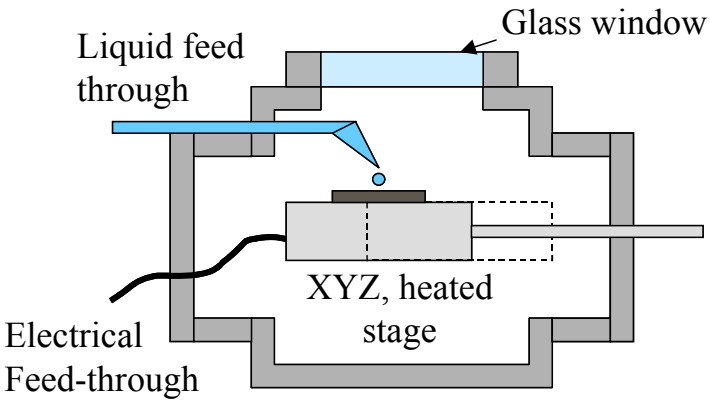

Figure MC-20: Diagram of preliminary vacuum encapsulation system.

Diffusion Evacuation and Furnace Sealing System

Because the temperature characteristics of process 2 were significantly higher than process 1, it was determined that it would be easier to build a new separate system from scratch rather than adapt the existing system. The system (Figure MC-21) consists of a small mass elevated thermal stage, suspended in a glass vacuum jar to maximize localized heating. The chamber is mounted on a stage system with appropriate valve controls and electrical feed-throughs for power, electrical probes, and temperature sensors. A sample in the system can be heated as high as 800 degrees Celsius at vacuum levels as low as 10^{-4} torr. The system is used for the furnace sealing experiments in this work.

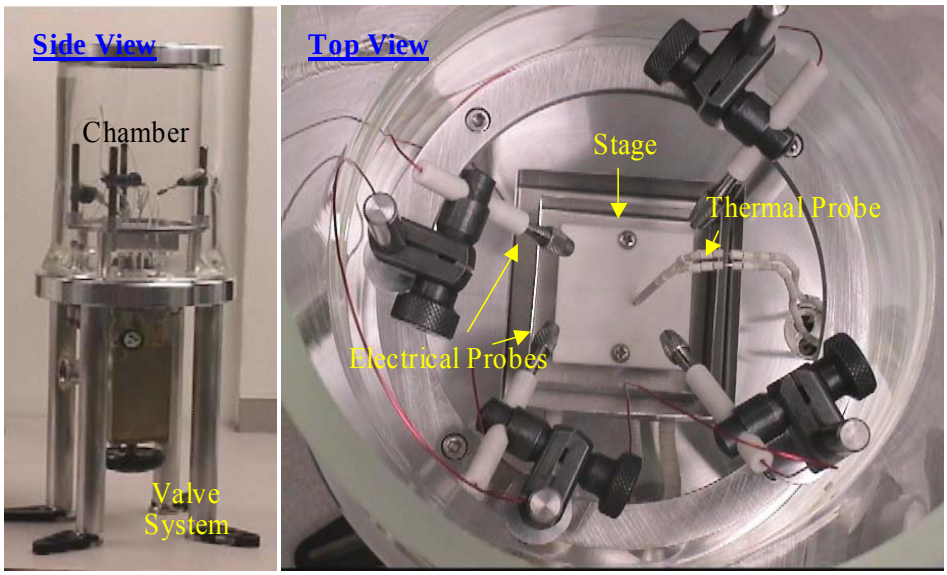

Figure MC-21: Side and top down view of HVAC furnace sealing system

2c. Evaluate Appropriate Sealing Materials for Application Suitability

One of the fundamental aspects of the technology is the performance of the sealing material. The small nature of the micro-package makes it very susceptible to the effects of gas diffusion. Thus the material must be extremely impermeable, but still be usable in this application. An existence search was performed for acceptable materials. The fundamental characteristics we evaluate materials by are:

- Temperature: Most acceptable hermetic materials require high processing temperatures. For example, most low temperature "true" glasses typically have a melting temperature in the range of 400-800 degrees C. The deposition process must be compatible with the MEMS and other microelectronics.
- Outgassing/evaporation: If the material is to remain in a vacuum, and be acceptable as a hermetic material, it may not outgas any component into the package. This eliminated most epoxies and materials composed of solvents and solute. Similarly, the combination of elevated temperature and vacuum can result in the material effectively being evaporated in the package. Thus, this usually means the material need to have a high molecular weight, or vaporization point.
- Gas permeability: In order to maintain a seal, the material must be very impermeable to gaseous diffusion.
- Moisture permeability: Maybe more critical than gas diffusion, the material must be impermeable to moisture and humidity, which eliminates most polymer and organic based sealants.
- Wetting: If the material is to be successfully applied, and maintain a seal, it must wet adequately enough to fill the micron scale crevices around traces and micro-topography. Conversely, the material should not wet excessively such that the substrate is completely covered and the material runs off during application.
- Reliability: The material is of no use if it cracks and fails during cooling, evacuation, or long term use.
- Cost/availability/manufacturability: The sealing material should emphasize manufacturability. It should not be too costly, or overly complicated for implementation.

We identified a number of potential materials, including:

- High Molecular Weight Solvent Free Epoxies (HMSFE): There are a number of high molecular weight solvent free epoxies commercially available (Epotek), that are acceptable for application in a vacuum and do not outgas significantly. The problem with these materials is that, even the best of them, have permeabilities two orders of magnitude worse than glass. The benefit is they are extremely easy to work with, and are cost effective.
- Liquid Crystal Polymers: LCP (Vectran) is a special set of thermoplastics that exhibit a very ordered structure that is extremely impermeable and is moisture resistant, while having a processing temperature in the 200-500 degree C range. LCP typically exhibit gas permeabilites roughly one order of magnitude worse than glass.
- Low Temperature Glasses: A number of low melting temperature (400-600 degrees C) glasses are available which have optimal hermetic characteristics.
- Two Stage/Phase Glass Materials (2SG): We have investigated the use of a two processing step material composed of Pyrex or silicon powder suspended in a resin. The material starts as a thick liquid, that when heated to 100 ^{o}C solidifies into a highly porous resin-powder solid. If the material is further heated to 500-600 degrees C, the material transitions to a highly dense impermeable glass.

- Metals/Solders: Metals and solder are an attractive alternative, giving their impermeable nature and often low melting temperature. They are conductive, which can be a problem in some applications, and wet very poorly to most semiconductors. Additionally, their extremely high surface tension makes conforming to micro-topographies difficult.

We have evaluated each of the above materials. The table below lists the best option determined. The LCP seems to have the optimum characteristics of low processing temperatures and low permeability to gasses and moisture. In addition, the adhesion and flow characteristics make it optimum for the application.

Material Name	Type	Processing temp (C)	K_{Helium} (cm^2/sec)	K_{H20} (g-cm/sec)
Epotek 353-ND	HMSFE	110-150	2.1E-9	~1E-10*
Epotek OG205 (UV)	HMSFE	75-100	3.7E-9*	~1E-10*
Torr Seal	HMSFE	25-100	1.0E-10*	Not Available
Vectran 400	LCP	225-235	1.06E-11	1.18E-12
Vectran 200	LCP	280-290	5.15E-12	6.76E-13
FX11-036	2SG	420	1.25E-12*	Not Available

*Estimates from literature

Table MC 1 -1 Material Options

2d. Demonstrate Preliminary Encapsulated MEMS Sensor in Micro-Package

The major deliverable for this work is a proof of principle packaged MEMS structure. A number of samples were prepared using various combinations of the materials and cap structures discussed above. Figures MC-22, 23, 24, and 25 show an assortment of successes and failures. Figures 22 and 23 show two varying results of encapsulation. In each case a SiCN cap was used and sealed with a high molecular weight epoxy. In Figure MC-22, the epoxy wettability was too high, and the epoxy spread excessively and exposed the top of the cap structure. Although not pretty, the encapsulation was successful, and the MEMS sensor remained intact and functional. Figure MC-23 is a much nicer result, in which the sealant formed a much more uniform spherical droplet on the cap, and had minimal spreading. The improvement was a result of understanding gained through many experiments in which materials, temperature, volume, curing times were varied.

Figure MC-24 is a photograph looking into a formed cavity that had been sheared to reveal the interior result. This particular sample was a SiCN cap on glass wafer. The photograph shows the successful cavity formation, and some leaking of the sealant under the cap edge. The leaking is a result of the high wettabiliy and low surface tension of this particular sealant material used. There is a tradeoff involving these characteristics. If the wetting is poor and the surface tension is high, there is a strong likelihood that the material will not fill and seal the many small surface topographies. Figure MC-25 is an example of desirable wetting, is a close-up view of traces exiting the micro-package sealed conformably by the epoxy sealant. Excellent conformal sealing is an absolute requirement of this technology.

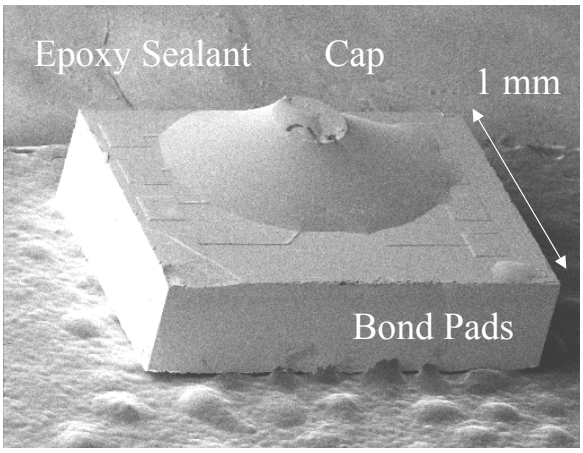

Figure MC-22: SEM of a sealed (epoxy) cap (SiCN) in which the epoxy has wet and left the cap exposed. Device under the cap was still functional.

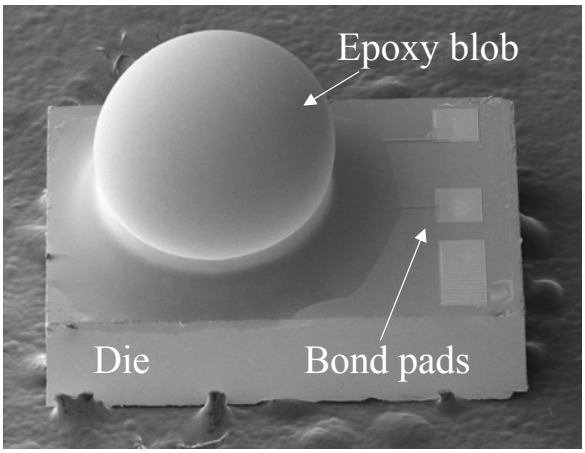

Figure MC-23: SEM of a uniformly sealed (Epoxy) cap (SiCN).

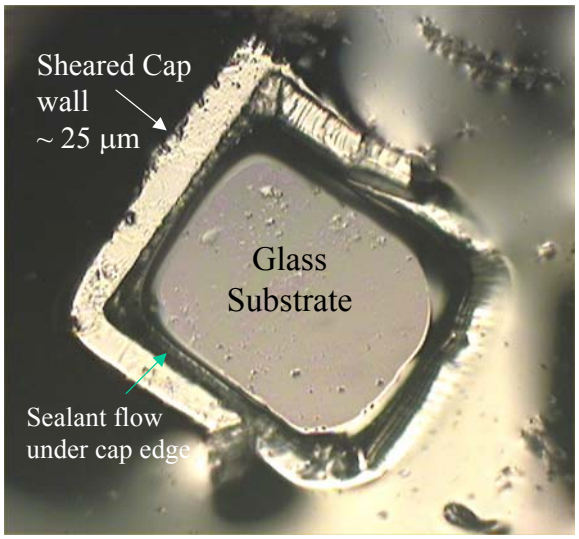

Figure MC-24: Sealed cap structure in which the cap has been sheared off to inspect interior cavity.

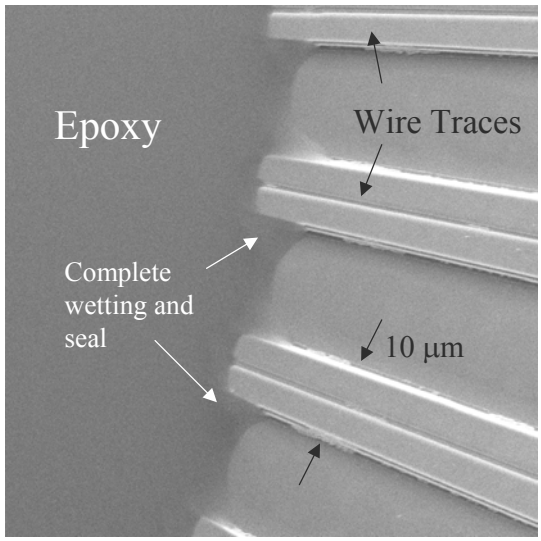

Figure MC-25: Close-up of seal around wire trace feed-throughs at the exit of the micro-package.

After the above experiments were performed, a majority of the work concentrated on identifying the best sealing material. From this study we have concluded that LCP has the best processing characteristics, while not sacrificing hermetic quality. Figure MC-26 shows a RF MEMS device that was encapsulated with LCP. The LCP has excellent adhesion and wetting characteristics. An example hermiticity decay plot is shown in the next section. We believe that LCP has the best potential for use in this application.

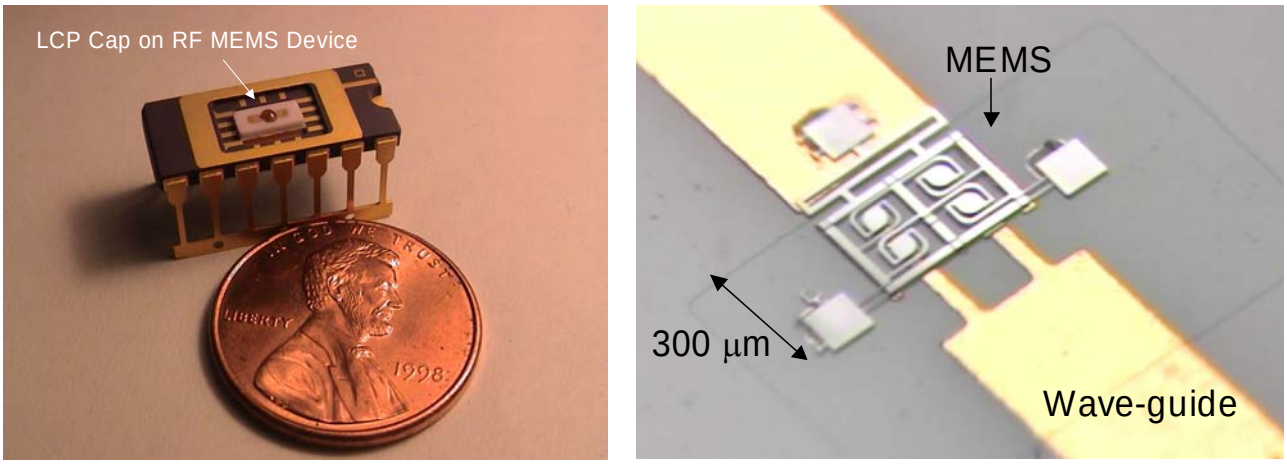

Figure MC-26: LCP Encapsulated RF MEMS. (Left) Packages for testing, (Right) Close-up of MEMS on Alumina substrate.

2e. Experimentally Evaluate the Preliminary Micro-package

With a preliminary set of MEMS sensing devices successfully packaged in a vacuum, and the devices tested and calibrated for effective sensing, we were able to conduct a preliminary set of package evaluation experiments. The result was very promising. The basic test device consisted of a SiCN cap sealed at a number of initial pressures using a low molecular weight epoxy. Figure MC-27 shows a quick test measurement taken immediately after packaging compared to the sensor calibration data. The figure shows that the sensors are indeed functioning properly after sealing. The small variation is likely due to the vacuum control of the packaging system, compared to the highly precise MMR Technologies calibration system. Figure MC-28 shows the measured decay of a similar device initially packaged at 1 milli-torr compared to the theoretical diffusion based prediction. The data matched the prediction very well. From this we can conclude that the package seal is good and that it does not suffer from a fine or gross leak. If there were a fine leak, the expected influx would be orders of magnitude higher. Using the data, the permeability of the epoxy to air can be found to be ~7.4×10^{-10} cm^2/sec. The variation between the prediction and the measurements was expected. The model was based on the ideal assumptions of material uniformity and assumes the permeability of the material to air as the baseline. It is certain that the smaller molecular weight components of air will diffuse more quickly. The vacuum sensor cannot account for this, and thus the leak rate should be slightly higher than the theoretical estimation.

For this device, the cavity effectively reaches five percent of atmospheric pressure within the first 120 days. This is of course not good enough for many applications. The epoxy was used solely for creation of a proof of principle device. The next step would be to improve the package through better materials. By doing this we would expect to be able to improve the hermetic quality of the package significantly. Figure MC-29 shows the predicted effect of using better sealing materials, in this case the LCP and glass. For example, using Glass 7740, the time to reach within 5% of atmosphere should be well over 10 years. The final required hermiticity of course depends on the device application.

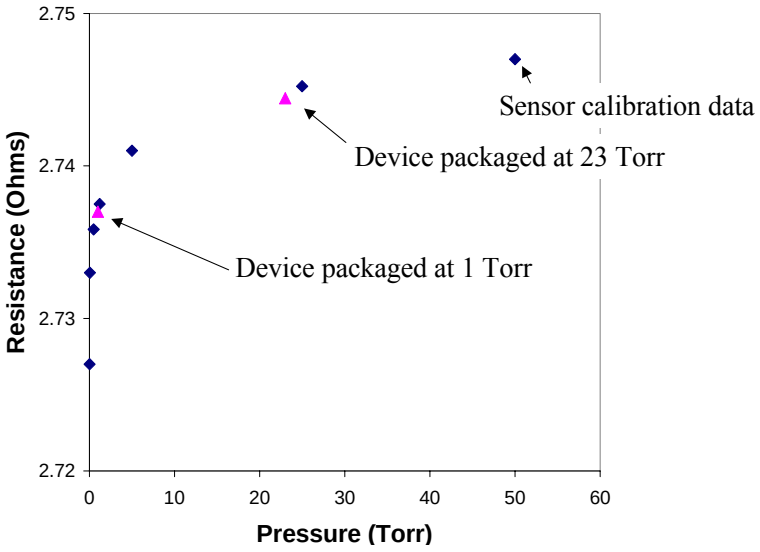

Figure MC-27: Plot of vacuum sensor measurements taken immediately after packaging with SiCN and epoxy and compared to the original calibration data.

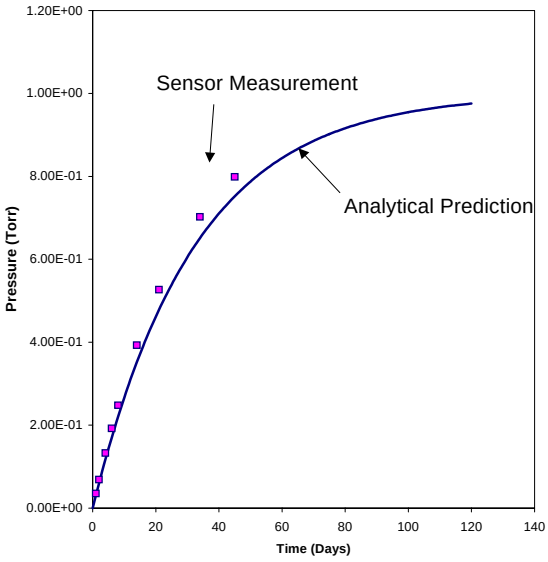

Figure MC-28: Plot of the degradation of the vacuum in the package, measurements and analytical prediction.

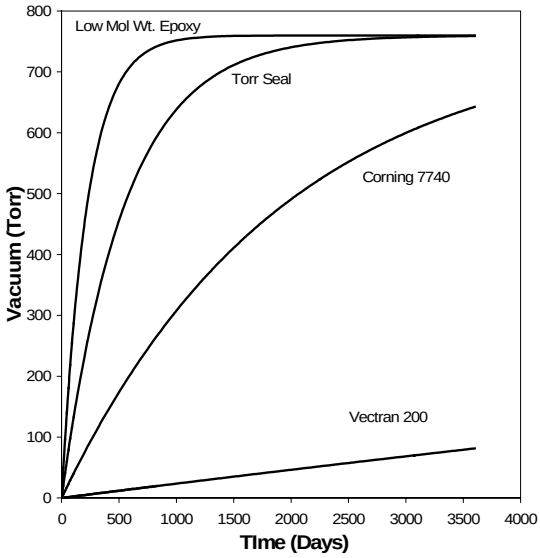

Figure MC-29: Plot of expected vacuum degradation versus time for several encapsulation materials.

6. Administration

6.1 Personnel

Principal Investigator: Dr. Victor M. Bright
Co-Investigators: Dr. Y.C. Lee, Dr. Martin L. Dunn
Postdoctoral Research Assistant: Dr. Kevin Harsh
Professional Research Assistant: Ms. Ann Geesaman

6.2 Publications

F.F. Faheem, K.C. Gupta, and Y.C. Lee, Post-Enable Flip-Chip Assembly for Manufacturable RF-MEMS. Published and presented at the Twelfth International Conference on Solid Stat Sensors, Actuators, and Microsystems. Boston, June 8-12, 2003

6.3 Student Theses

PhD Thesis (in progress). Faheem Faheem, "Encapsulation and Developments of 2-D Variable Capacitor Array for RF-MEMS Applications."